UC San Diego

UC San Diego Electronic Theses and Dissertations

Title

Wave-Current-Tide Interactions in Coastal Environments

Permalink

https://escholarship.org/uc/item/71q3w8g9

Author

Ho, Allison

Publication Date

2024

Peer reviewed|Thesis/dissertation

eScholarship.org Powered by the California Digital Library
University of California

UNIVERSITY OF CALIFORNIA SAN DIEGO

Wave-Current-Tide Interactions in Coastal Environments

A dissertation submitted in partial satisfaction of the
requirements for the degree Doctor of Philosophy

in

Oceanography

by

Allison Joan Ho

Committee in charge:

Sophia Merrifield, Chair
Nicholas Pizzo
Mark Merrifield
Sutanu Sarkar
Eric Terrill

2024

Copyright

Allison Joan Ho, 2024

All rights reserved.

The Dissertation of Allison Joan Ho is approved, and it is acceptable in quality and form for publication on microfilm and electronically.

University of California San Diego

2024

DEDICATION

This is dedicated to my family.

EPIGRAPH

There is a voice inside of you
That whispers all day long,
"I feel this is right for me,
I know that *this* is wrong."
No teacher, preacher, parent, friend
Or wise man can decide
What's right for you - just listen to
The voice that speaks inside.

Shel Silverstein

The world is changing, following its people.

Yup'ik adage

TABLE OF CONTENTS

Dissertation Approval Page iii

Dedication iv

Epigraph v

Table of Contents vi

List of Figures viii

List of Tables xi

Preface xii

Acknowledgements xiii

Vita xvii

Abstract of the Dissertation xviii

Chapter 1 Introduction 1
1.1 Dissertation Outline 7

Chapter 2 Inertial, diurnal, and semidiurnal variability in nearshore wave records 9
2.1 Introduction 9
2.2 Data 11
2.3 Methods 14
2.4 Results 15
2.5 Discussion and Conclusions 25
2.6 Appendix 29

Chapter 3 Mechanisms for periodic wave modulation 32
3.1 Introduction 32
3.2 Governing equations 33
3.3 Stationary wave-current interaction 36
3.4 Wave-tide interaction 37
3.5 Refraction 46
3.6 Discussion and Conclusions 52
3.7 Appendix 53

Chapter 4 Wave-tide interaction for a strongly modulated wave field 55
4.1 Introduction 55
4.2 Data 57
4.3 Simplified Theories for Wave-Tide Interaction 63

4.4 Comparison to Observations 75
4.5 Discussion 79
4.6 Conclusion 80
4.7 Appendix 82

Chapter 5 Concluding Remarks 83

Chapter 6 Appendix 85
6.1 Mechanisms for wind-driven diurnal modulations 85
6.2 Spectral Analysis 87
6.3 Co-located Observations 92

Bibliography 93

LIST OF FIGURES

Figure 1.1. Surface waves at the air-sea interface 3

Figure 1.2. Distribution of peak period T_p from wave measurements located in deep water in the Great Lakes (green), Gulf of Mexico (pink), Atlantic (red), and Pacific (blue), separated by season (summer indicates measurements during June, July and August; winter indicates measurements during December, January, and February) 5

Figure 2.1. (Top) Map of currently operational CDIP (dark yellow) and NDBC stations (light yellow) 13

Figure 2.2. For each buoy, distance from shore vs mooring water depth, colored by region 16

Figure 2.3. Map of semidiurnal (M2) diurnal (S1) and inertial (f_{in}) energy in H_s, reported as the energy above the background of each constituent as a percent of total energy between O(0.5-6cpd) 18

Figure 2.4. Binned monthly averages of spectra of significant wave height (top, gray), currents in wave direction (middle, purple), and wind speed (bottom, green), not normalized for background variance 20

Figure 2.5. Measurements of inertial modulations to H_s 21

Figure 2.6. (Left) normalized spectrum of H_s as a function of cycles per day, plotted at the latitude of the respective buoy along the west coast of North America in water deeper than 20 m 22

Figure 2.7. Measurements of semidiurnal modulations to H_s 23

Figure 2.8. Normalized amplitude of H_s modulations at M2 calculated from the H_s spectra vs amplitude of measured surface current at M2, normalized by average wave phase speed, categorized by regions described in Figure 2.2 24

Figure 2.9. Map of semidiurnal (M2) tidal current ellipses predicted by the barotropic tide model for the West Coast (left) and East Coast Florida Bight region (right) 26

Figure 2.10. Measurements of inertial modulations in H_s (black) from two buoys off the Oregon Coast: NDBC buoy 46100 moored in 582 m water depth (top); CDIP buoy 36 moored in 36 m water depth (bottom) 27

Figure 2.11. Amplitude of $H_{s,sea}$ modulations at S1 vs amplitude of measured wind speeds at S1, categorized by season 29

Figure 2.12. The average semidiurnal (M2, blue) diurnal (S1, green) and inertial (f_{in}, orange) energy at $S(f)$ for each wave frequency, reported for each constituent as the energy above the background as a percent of total energy between O(0.5-6cpd) at each frequency 30

Figure 3.1. Coordinate system for wave-tide interaction 38

Figure 3.2. Cumulative density functions for the simulated H_s, separated by initial significant wave height $H_{s,0}$ 41

Figure 3.3. Predicted change to H_s, normalized by $H_{s,0}$, as a function of water level change and current magnitudes at various depths 42

Figure 3.4. Predicted change to H_s, normalized by $H_{s,0}$, as a function of incident peak period and current magnitude at various depths 43

Figure 3.5. Predicted change to H_s with respect to $A_u/c_{g,0} + A_h/2h_0$ for stationary (downwards triangle) and tidal (upwards triangle) approximation for range of parameters observed in moored buoy array 45

Figure 3.6. Synthetic currents (top) and ray trajectories (bottom) 48

Figure 3.7. Time series of energy E/E_0 (right) at locations that represent a fixed observer denote by triangle and circle (left) 49

Figure 3.8. Bathymetric refraction of ray paths through the Southern California domain, propagating from the left of the domain at an angle $\theta = -20^o$ 50

Figure 3.9. Ray paths (right) through modeled barotropic M2 tidal currents predicted (left) for incident 10 second rays from 270^o clockwise from north 51

Figure 4.1. Location (a,b) and measurements from the Coastal Data Information Program (CDIP) Datawell Waverider directional wave buoy, CDIP132, used to develop and corroborate the model 58

Figure 4.2. Spectral analysis of (a) observed and modeled surface currents, (b) observed and modeled water levels, and (c) observed swell significant wave height, $H_{s,swell}$ 62

Figure 4.3. Estimated directional spectra observed during (a) following currents ($U =$ 0.32m/s) and (b) opposing currents ($U = -0.25$m/s) on 2020-08-18 21:30 and 2020-08-19 03:30 respectively 63

Figure 4.4. Given an incident wave spectra (grey), we show the resulting shift due to a change in current (solid) or a change in water level (dashed) as predicted by the model given by equations (4.31), (4.27), and (4.35) 72

Figure 4.5. Wave spectrogram observed over one day (a) and reproduced wave spectrogram from the numerical model of the omni-directional spectra (b) developed using observations to set the initial condition and forcing terms (currents and depth variations) 77

Figure 4.6. Observations are used as an initial condition to estimate the resulting shift of the directional spectrum under tidal currents and water level variations (d) 78

Figure 6.1. Forced pendulum with varying length (left), solved for varying initial conditions φ_0 (center) 87

Figure 6.2. Inferring modulating amplitude for additive signal (top) and multiplicative signals (bottom) applied to additive signals at f_1 (left) and multiplicative signals f_2 (right) generated from artificial time series with red noise 90

Figure 6.3. For each year, the number of stations with observations of waves (black), wind (green), remotely-sensed HFR currents (purple) and in-situ ACM currents (dark purple) 92

LIST OF TABLES

Table 2.1. Number of buoys with power spectrum with signals at specified constituents (M2, S1, and f_{in}) in significant wave height H_s, and as a percent of total buoys (N=249). Signals are chosen based on existence of a peak greater than the spectral uncertainty for the background power spectrum ($X^{Hs} > \delta X_0^{Hs}$). 17

Table 3.1. Values of parameters in simulation (water depth h_0, current amplitude A_u, water level amplitude A_h, initial significant wave height $H_{s,0}$, and initial peak period $T_{p,0}$) and total number of values for each parameter (N). 40

Table 4.1. First five dominant tidal constituents for Fernandina Beach (30^o42'33.1"N, 81^o17'31.2"W) and corresponding period in hours and amplitude in meters from the global tidal model TPXO 9 and Tide Model Driver 2.5 (Egbert and Erofeeva, 2002; Erofeeva et al., 2020) 61

Table 4.2. Change in swell significant wave height $\Delta H_{s,swell}$, change in swell peak period $\Delta T_{p,swell}$, and change in swell directional spread $\Delta\sigma_{swell}$ at the Fernandina Beach station CDIP132 from 2020-08-01 to 2021-08-01 61

PREFACE

This thesis was accomplished under the guidance of my two advisors, Sophia Merrifield and Nicholas Pizzo. This document was originally submitted with Chair and Co-Chair designations, respectively, but institutional affiliations prevented the formal acknowledge of Dr. Pizzo as Co-Chair. Thus, let this document record that Dr. Pizzo acted as co-advisor for much of the last half of my graduate studies and acted as Co-Chair for both my thesis and defense.

ACKNOWLEDGEMENTS

A PhD is not done in a vacuum, and I owe so much to my advisors, committee members, collaborators, colleagues, peers, friends, and family. First, I would like to thank my research advisors, Sophia Merrifield and Nicholas Pizzo. I would be nowhere without their incredible generosity with their time and resources. Sophia's passion for observational oceanography has inspired me since we met, and her faith in me has allowed me to explore my own interests bolstered with the freedom to make mistakes and the persistence to get up and try again. I am endlessly grateful for Nick's scientific guidance - much of what I know about ocean waves I learned from his expertise. Beyond waves and pendulums, I am continuously motivated by his kindness and positivity, which has often been a light in the noise. I am also grateful to my committee, to Eric Terrill, Mark Merrifield, and Sutanu Sarkar, for their feedback and wisdom, which always comes at the right time and leaves me refreshed with new insight and perspective.

This work would not be possible without support from the Coastal Data Information Program. I graciously acknowledge the effort of this program to develop and maintain the observations that were used in this dissertation and I am grateful for their unfettered support throughout the process; Jim Behrens, Randy Bucciarelli, and Corey Olfe have been incredible colleagues and advocates for my work. I also am grateful for funding from the U.S. Army Corps of Engineers and the meaningful collaborations with USACE scientists, including Ty Hesser, Tripp Collins, Candice Hall, Bob Jensen, and Ali Abdolali. I've also benefited from the insight of other collaborators and colleagues during various other projects and research cruises, including Bia Villas Bôas, Gwen Maréchal, Janet Becker, Bill O'Reilly, Luc Rainville, Fabrice Ardhuin, Steve Elgar, Britt Raubenheimer, Luke Kachelein, Hendrik Tolman, and many more; I'm thankful for being lent an ear time and time again, these conversations have been some of the most important learning moments.

The Coastal Observing Research and Development Center (CORDC) has been my home over the past seven years. I'm grateful to work with talented scientists, staff, and engineers that tackle challenging problems every day with such care and tenacity. I thank all past and

present members of CORDC for their support and efforts in both the field, in the lab, and in the office that make the science not only possible but endlessly interesting. Within the lab, the microclimate created by the graduate students and postdocs, including Ray Young, John Lodise, Mika Siegelman, Ryan McCarthy, Kaley Mudd, Andre Amador, Eric Gallimore, Travis Schramek, and Margaret Sullivan, has made coming to work every day enjoyable and gotten me through some of the hardest moments. I am grateful for their kindness and support, but I think I'm most grateful for all of the fun we had along the way. In particular, I'm thankful for the thirty days at sea with Ray that finally brought us together as friends, I have learned so much from him and will miss the ability to pop over to the next office to work over or rant about a problem. From advising summer interns to attending conferences to his endless encouragement over the last couple months, I couldn't ask for a better co-mentor in John. And lastly, I've spent many countless hours in the same 10x10 square feet and I'm so grateful to have shared that time with the best office mates. Travis's guidance and mentorship has been invaluable and I'm so grateful to have had him looking out for me and my sanity throughout this process. I know Margaret's optimism, humor, and integrity will continue to inspire and buoy me for years to come.

I am grateful to have experienced graduate school surrounded by a delightful group of people, including the 2018 cohort, AOS students, and the Scripps graduate student community as a whole. Whether it be in zoom meetings, in counterspaces, over coffee, or during Friday evenings at Surfside, I will forever be grateful for the camaraderie and companionship from Alaina, Wiley, Taylor, Max, Pascal, Rob, Gabi, Tricia, Athina, Bethan, Alex, Vanessa, Anela, Alyssa, Erica, Ale, Kelli, Kayla, Hunter, Jake, Joe, and many more. I am fortunate to have shared time here with all of you, and can only hope that I am able to find communities of equal kindness and brilliance wherever I go.

Beyond our scientific understanding, I believe our ability to impart meaning from our work into the world is going to be innately entwined with fostering a more empathetic, inclusive, and ethical scientific community. I am grateful to have experienced that sense of community amongst the passionate people who dedicate their time to improving the culture at Scripps,

including members of Women and Minorities in Science, the Equity Diversity and Inclusion Team, Unlearning Racism in the Geosciences, the UCSD Changemaker Fellow Learning Community, various institutional committees, and in the unspoken work of kind friends, unofficial mentors, and unsigned activism. This work should be accredited institutionally and formally, especially as these efforts are often undertaken by those marginalized by these institutions in the first place. At the end of the day, we are people before we are scientists, and our scientific efforts are only as limited as the care, respect, and empathy we show one other.

Lastly, I owe everything to the support of my friends and family. They have been with me through the rain and the shine of graduate school in the form of backpacking trips, pier swims, family reunions, late-night rides, meals, and phone calls. Thank you to Brianne and Anne, for making me look forward to Wednesdays and being my light at the end of the tunnel. Thank you to my friends from college and outside of graduate school for the welcome reminder that the world is bigger than La Jolla. Thank you to my family, both immediate and extended. To Madi and Livi, you are my role models. Beyond any accolade or title, my proudest accomplishment is being your big sister. To my parents, you will never know how much solace I've found at home over the years. I am so grateful for the encouragement and resources you have given us to pursue our interests, but beyond that you have taught me so much about kindness and happiness. Finally, Sam, your impact on me is immeasurable. You are true to yourself in everything you do and inspire me to do the same. I would be nowhere without your empathy and support, and I am so grateful to have met you.

Chapter 2, in part, is currently being prepared for submission for publication of the material, and is co-authored by Sophia Merrifield and Nicholas Pizzo. The dissertation author was the primary investigator and author of this material.

Chapter 3, in part, is currently being prepared for submission for publication of the material, and is co-authored by Sophia Merrifield and Nicholas Pizzo. The dissertation author

was the primary investigator and author of this material.

Chapter 4, in full, is a reprint of the material as it appears in the Journal of Physical Oceanography. The dissertation author was the primary investigator and author of this paper. A Ho, S Merrifield, N Pizzo, Wave-Tide Interaction for a Strongly Modulated Wave Field, Journal of Physical Oceanography. https://doi.org/10.1175/JPO-D-22-0166.1

VITA

2018	Bachelor of Arts (Physics and Astronomy), Pomona College
2020	Master of Science (Oceanography), University of California San Diego
2024	Doctor of Philosophy (Oceanography), University of California San Diego

PUBLICATIONS

Ho, A., S. Merrifield, and N. Pizzo, 2023: Wave–Tide Interaction for a Strongly Modulated Wave Field. J. Phys. Oceanogr., 53, 915–927, https://doi.org/10.1175/JPO-D-22-0166.1.

ABSTRACT OF THE DISSERTATION

Wave-Current-Tide Interactions in Coastal Environments

by

Allison Joan Ho

Doctor of Philosophy in Oceanography

University of California San Diego, 2024

Sophia Merrifield, Chair

Coastal and maritime communities rely on wave models for adaptation and management of coastal hazards, maritime safety, and infrastructure planning. Accurate representation of ocean waves and their subsequent impact on air-sea fluxes is also important for numerical weather and climate prediction models. Ocean currents can have significant impact on accurate prediction of wave conditions as they modify wave direction, frequency, and amplitude. Resolving these effects is complicated in coastal regions, where ocean currents vary spatially and temporally across many scales. Thus, co-located measurements of ocean wave and current conditions are essential for better understanding and predicting surface wave conditions in nearshore environments. This thesis explores the variability of surface waves due to wave-current-tide interactions in coastal

wave climates. Observations from a global network of over 200 moored wave buoys show that 87% of wave height records have significant inertial, diurnal, or semidiurnal variability. Diurnal variability in wave records is observed at high frequencies, related to wind forcing, and varies with latitude and distance from the coastline. Inertial variability has a strong seasonal cycle and is observed predominately in the Pacific Northwest. Finally, we find the strongest semidiurnal modulations in channels, on the East Coast, and in regions known for strong barotropic and baroclinic tides. These regional and seasonal patterns demonstrate how surface wave climate variability is influenced by distinct oceanographic phenomena. Ocean currents impact wave fields through both local effects from currents and water depth changes and non-local refractive effects from transverse gradients in currents and bathymetry. We demonstrate how the different mechanisms for wave-current interaction can lead to similar periodic modulations to ocean wave heights. Several examples of these modulations, influenced by tides and inertial currents, are presented. To characterize the exact influence of wave-tide interaction on the surface wave field measured by these buoys, we consider a case study at Fernandina Beach, FL where wave heights are modulated up to 25% over a tidal cycle. Observations show that wave heights increase when traveling with tidal currents and decrease when opposing them, with the most significant effects occurring in the long-period swell band. We use both analytical and numerical solutions to model these interactions, employing principles of geometrical optics and conservation of wave action. We consider the tide as a one-dimensional progressive shallow-water wave and find that the numerical model accurately reproduces the observed tidal modulation to wave amplitude and phase. Our model shows that the environmental conditions, wave conditions, and the relative speeds between the tide and surface waves determine the magnitude and direction of these modulations.

Chapter 1

Introduction

Interactions between the atmosphere and ocean redistribute mass, momentum, and energy in the climate system. These interactions are fundamental to predicting Earth's weather and climate and are one of the largest sources of uncertainty in predictive models of the climate system (Large et al., 1994; McWilliams, 1996; Deike, 2022). At the sea surface, waves act as the gateway between the atmosphere and the ocean, mediating the exchange of heat, momentum, energy, and mass (Sullivan and McWilliams, 2010; Cavaleri et al., 2012). Surface waves mix the surface layers of water (Melville, 1996), altering upper ocean temperatures (Belcher et al., 2012) and the aerodynamic roughness of the sea surface (Donelan et al., 1993; Taylor and Yelland, 2001), and enhance gas exchange through wave breaking and entrainment (Wallace, 1992; D'Asaro and McNeil, 2007; Deike, 2022). In turn, surface waves are modified kinematically and dynamically by the underling ocean currents and overlying winds (Villas Bôas and Pizzo, 2021). As wind blows on the ocean, it perturbs the ocean surface (Miles, 1957; Phillips, 1957; Pizzo et al., 2021), allowing energy and momentum to be transferred between the fluids. Over long periods of time and long distances, these small perturbation grow to form long period swell waves. These waves then propagate away from their generation, crossing entire ocean basins (Snodgrass et al., 1966), before breaking on our beaches and depositing their momentum and energy, with fundamental implications for coastal processes. Along the way, they interact with other waves, dynamic ocean currents (Kenyon, 1971), internal waves (Gargettt and Hughes,

1972), tides (Longuet-Higgins and Stewart, 1960), and complex bathymetry (Munk and Traylor, 1947). These interactions leave imprints that the waves carry with them, consequently connecting the storms that generate these waves with the rest of the ocean.

Understanding these dynamics is not only important for contextualizing the role of surface waves in the global climate system but also has fundamental operational consequences for accurate forecasts of wave climates and marine weather (Cavaleri et al., 2007), interpretation of remote sensing measurements (Cox and Munk, 1956; Phillips, 1988), marine safety, coastal management and engineering, and recreation (Sadrpour and Reineman, 2023). Accurate waves and wave energy fluxes are necessary for predicting nearshore circulation, wave runup, and sediment transport, and can have compounding effects on the impacts of flooding and inundation (Battjes et al., 1987; Stockdon et al., 2006), coastal erosion, sea level rise, and natural disasters (Harley et al., 2017). And while understanding waves in coastal regions is of particular human and economic interest, coastal regions often are dynamically complex environments that require significant computational resources to resolve these processes with fidelity. That is to say, the large number of degrees of freedom at the coast make observations in these regions, used to constrain these models, particularly valuable.

To date, decades of academic research have led to advancements in our understanding of the dynamics of ocean waves. This has only been possible through the integration of theoretical, experimental, and observational techniques. The theoretical field of surface gravity waves has developed and evolved alongside improvement and collection of wave measurements (Edson et al., 2007). Computational and numerical advancements in wave modeling have led to the development of both spectral and phase-resolved wave models that are able to replicate nearshore and global wave climates (Cavaleri et al., 2012). Early modern wave forecasting began famously with Harold Sverdrup and Walter Munk's wave prediction technique that was used in the 1944 D-Day landings at Normandy to help Allied forces understand the best timing for surf conditions in order to land their troops safely on shore (Sverdrup and Munk, 1947). These predictions used empirical relationships between wave height, period and fetch, the duration and distance over

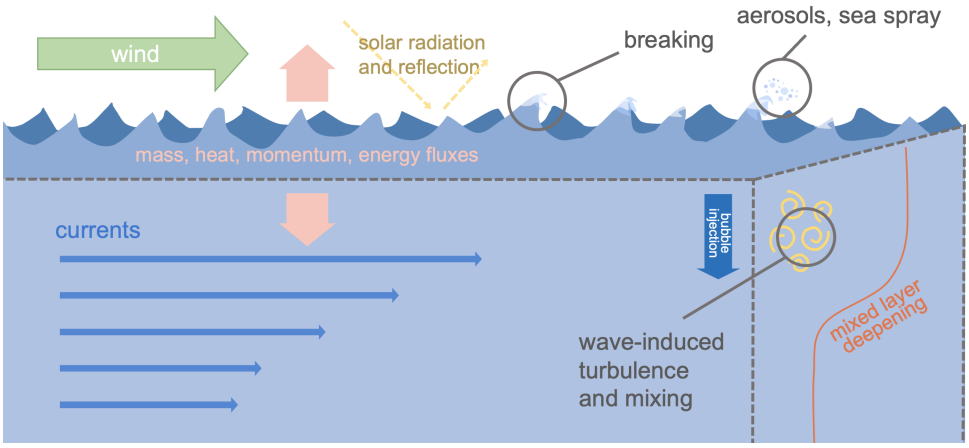

Figure 1.1. Surface waves at the air-sea interface.

which a wind blows. Now, third generation wave models simulate the physics that govern the generation and propagation of surface waves, and modern efforts are working to introduce two- and three-way coupled models between the atmosphere, waves, and ocean. These models are critical for weather forecasts, contextualizing sparse observations and environmental conditions, and forecasting future wave conditions that help coastal communities mitigate storm surge and mariners navigate rough seas.

Through these advances in both modeling and observations, we know that surface wave climates are influenced primarily by synoptic scale wind forcing that leads to the presence of both remotely and locally generated waves. This often dictates seasonal and regional patterns in wave climates. For example, two major generation regions dominate Pacific Basin wave climate. At buoys off the coast of California, northwest swell from Northwest Pacific storms during boreal winter and longer period swell from Southern Ocean storms during boreal summer create a seasonal signal in the coastal wave measurements (Villas Bôas et al., 2017; Colosi et al., 2021) (Figure 1.2). Average global wave height resembles the distribution of wind speed (Young, 1999; Timmermans et al., 2020) and regions with high extra-tropical and tropical cyclone activity (Lodise et al., 2022; Grossmann-Matheson et al., 2024). The amount of space over which waves can grow and propagate also has a significant impact on regional patterns. Pacific Ocean wave climates often experience swells with periods 15 seconds or longer; in contrast, the wave periods

observed in the Great Lakes rarely exceed 6 seconds (Figure 1.2).

At smaller scales, it has been estimated that ocean currents are responsible for up to 75% of the spatial variability in surface wave heights on spatial scales between 10 and 100km (Ardhuin et al., 2017). When waves interact with currents, their amplitudes and phase may be modulated kinematically and dynamically, as dictated by conservation of geometric optics and wave action respectively (Longuet-Higgins and Stewart, 1960; Bretherton and Garrett, 1968), leading to waves steepening or attenuating and providing a two way coupling between the waves and currents (Pizzo and Salmon, 2021). Several recent observational and numerical studies have shown that refraction and advection of long waves due to surface current vorticity is the dominant mechanism for significant wave height gradients in the open ocean (Ardhuin et al., 2017; Quilfen and Chapron, 2019; Bôas et al., 2020). Wind-sea waves with short wavelengths are most impacted by divergent components of the currents (Rascle and Ardhuin, 2013), but it is not known how sensitive waves in between these ranges are to different components of ocean currents. These interactions can lead to strong steepness modulations and in some cases enhanced wave breaking (Romero et al., 2017; Vrećica et al., 2022).

Surface gravity waves in the ocean are modeled through our understanding of their generation, propagation, and dissipation. Linear wave theory describes the propagation of small amplitude gravity waves on a fluid surface where the flow is inviscid, irrotational, and incompressible (Airy, 1845). Conservation of energy balances the kinetic and potential energy that is exchanged for an oscillating water parcel in a wave and thus determines the wave amplitude. Currents Doppler shift waves, meaning they change their frequency, which modifies the phase and group speed. The WKBJ (Wentzel–Kramers–Brillouin Jeffreys) approximation of linear wave theory describes how wave kinematics adjust due to changes in depths and currents that vary slowly relative to scales of the wavelength (Mei, 1992). Wave dynamics can describe the subsequent change in wave height due to the conservation of wave action, which is defined as the ratio of wave energy to the intrinsic frequency (Bretherton et al., 1968). We work in terms of conservation of wave action. In the presence of a current, wave momentum and energy are not

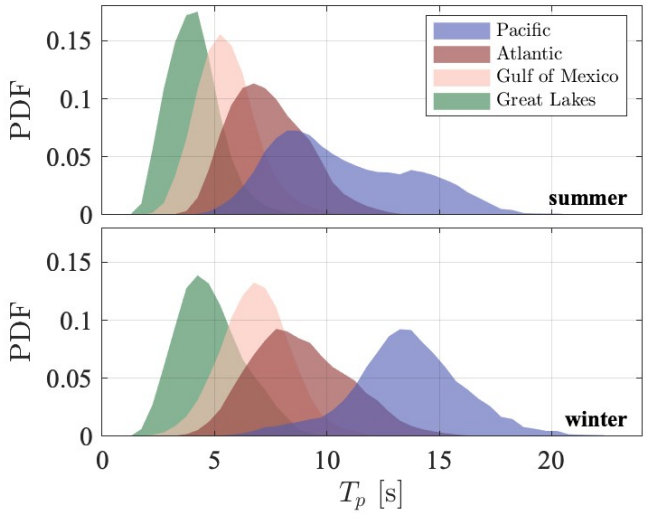

Figure 1.2. Distribution of peak period T_p from wave measurements located in deep water in the Great Lakes (green), Gulf of Mexico (pink), Atlantic (red), and Pacific (blue), separated by season (summer indicates measurements during June, July and August; winter indicates measurements during December, January, and February).

conserved because the waves and currents exchange momentum and energy (Longuet-Higgins and Stewart, 1962). The total momentum of the two systems is conserved. From these principles we can calculate that in the simplest cases of a linear wave propagating into a constant current field, currents following the direction of wave propagation 'redshift' the wave, elongating the wavelength, while opposing currents will reduce its wavelengths. This is summarized as

$$\omega = \sigma + \mathbf{k} \cdot \mathbf{U} \tag{1.1}$$

where the absolute frequency ω is observed by a fixed observer, σ and $\mathbf{k}$ are the intrinsic frequency and wavenumber of the wave, and $\mathbf{U}$ is the current. When wavelength decreases, wave amplitude will increase to conserve wave action. The shift due to a current can also lead to refraction, which alters the direction of propagating waves. The nature of this shifting is modified if the currents are either unsteady or inhomogeneous in time or space, relative to the scales of wave propagation.

Wave-current interaction is further complicated in the nearshore where the waves and

currents may both interact with bathymetry in complex ways. Unsteady tidal currents have been shown to significantly affect nearshore wave climates and motivates the importance of jointly assessing spatial and temporal wave gradients. Significant wave heights have been observed to vary up to 50% over a tidal cycle (Tolman, 1990). In fact, the influence of tides on surface gravity waves, which we hereafter call 'wave-tide interaction', influenced some of the earliest theoretical work on wave-current interaction, notably by Unna (1942) on how the Bristol Channel pilots see the worst seas at the end of the flood tide and Barber (1949) on the observations and theory of waves in tidal streams. Several studies have documented the effects of tides and inertial currents on wave conditions (e.g Gemmrich and Garrett, 2012; Wang and Sheng, 2018). Long before and outside of the modern Western academic study of wave-current interaction, the influence of currents or tides on waves is well-known to many coastal communities or anyone who spends time in the sea. For example, navigators are familiar with how strong currents at channels or inlets can lead to rough seas; the painting "The Junction of the Thames and the Medway" (Turner, National Gallery of Art, Washington DC) from 1807 depicts ships struggling to navigate steep, choppy waves in their passage through waters of the River Thames as they meet to enter the North Sea. Polynesian navigators identified currents by noting how they changed the shape of waves. The famed navigator Basil Tavake of Pileni Atoll of the Santa Cruz Reef Islands commented how "waves of this shape in the continuing absence of appreciable wind could only be caused by a current that was setting against the waves" (Lewis, 1994, p 150-142). The knowledge of the Arctic Indigenous Yu'pik people include a deep understanding of the complex Alaskan coastal environments, one Kongiganak resident John Phillip noting that the ocean swell suddenly get large when they arrive during the end of the incoming tide when the current is strongest (Fienup-Riordan and Carmack, 2011). Surfers have long discussed the "tidal push" where the surf appears to pick up on the incoming tide (Davidson et al., 2008). It is important to acknowledge that while the modern scientific field of wave studies and wave-current and wave-tide interaction is typically dated to have been established in the 20th century, the local and traditional knowledge of these phenomena has existed for millennia through relationships with

the environment embodied in life experiences.

Overall, there is evidence of surface waves interacting with currents at a broad range of spatial and temporal scales. This affects the signals in remote sensing measurements, the predictive capacity of forecasts and wave models, and the impact of surface waves in air-sea interaction and ocean mixing and circulation. Tides and other periodic ocean phenomena (e.g. inertial currents, diurnal winds) naturally account for a considerable amount of the temporal variability in wave climates. Improving our understanding of these phenomena leads to an improved understanding of how Earth's oceans and atmospheres behave and interact with one another.

1.1 Dissertation Outline

This dissertation seeks to understand short time scale variability in coastal wave climates by 1) characterizing the impact of tides, diurnal winds, and inertial currents in historical wave observations 2) identifying potential mechanisms for periodic variability in surface waves and 3) demonstrating a simplified framework for wave-tide interaction with the capability of resolving the amplitude, phase and frequency response of observed tidal modulations. This dissertation is organized as follows.

In Chapter 2, observations from a network of over 200 moored wave buoys are analyzed to characterize the influence of tides on wave spectra and bulk parameters. These observations indicate that diurnal, semi-diurnal, and inertial modulations are common features of nearshore ocean wave climates, contributing up to 15% of the wave variability on time scales shorter than 2 days and modulating wave heights up to a meter over a tidal cycle. The underlying phenomena at these isolated frequencies are apparent in co-located observations of diurnal winds, tides, and inertial currents. The persistence and prevalence of these modulations vary seasonally and regionally, and highlight the coupling between ocean wave climates and distinct oceanographic phenomena.

In Chapter 3, we identify possible mechanisms that allow tidal and inertial currents to impart energy into the wave field. A simple framework for wave-tide interaction is used to identify conditions that lead to modulation of significant wave height through frequency and wavenumber shifting by the local tidal current as well refraction and convergence by non-local tidal or inertial currents.

In Chapter 4, a case study is conducted off the coast of Florida, where strong tidal modulations have been observed in measurements of wave heights and higher order spectral moments, corresponding to a steepening of low-frequency waves on following currents. By representing the system as a long-wave short-wave interaction between the surface waves and the tide, a simple numerical model accurately reproduces the observed modulations.

Chapter 2

Inertial, diurnal, and semidiurnal variability in nearshore wave records

2.1 Introduction

Surface gravity waves act as a gateway between the atmosphere and the ocean, modifying the exchange of heat, momentum, energy, and mass. Variability in ocean wave climates is often driven by local atmospheric and oceanic processes which vary on short time (hours) and space (km) scales. The prediction of these processes and their impact on surface waves is an area of active research in wave modeling, observational campaigns, and in remote sensing. Without ocean currents, wave models may not accurately predict spectral peaks, swell arrival times, spatial gradients, and wave energy for surf and hazard forecasts. Variance in nearshore wave climates is influenced by remotely-generated swell and local forcing from meteorological conditions and complex coastal oceanic currents. Accurate prediction of these coastal wave conditions requires accounting for effects of tides and currents, which occur on daily time scales. Overall, understanding the effect of wave current interactions on observations across multiple spatial and temporal scales is important not only for improving forecasting but can also provide insight for remote sensing, air-sea interaction, ocean mixing, and long term climate trends.

On spatial scales shorter than 100 km, over 75% of the spatial variability in open ocean significant wave heights, H_s, is caused by waves interacting with ocean currents (Ardhuin et al., 2017). In the open ocean, it has been demonstrated both numerically and with remote sensing

observations that the refraction of surface waves through spatially inhomogeneous rotational currents is the dominant source of variations of wave heights (Kenyon, 1971; Quilfen and Chapron, 2019; Bôas et al., 2020; Marechal and Ardhuin, 2021). Previous work has largely focused on effects from quasi steady currents. In coastal waters, however, tides and complex bathymetry lead to unsteady and inhomogenous environments for surface wave propagation. The effect of wave-current interactions due to tides in shallow and intermediate coastal waters has been studied in various regional and theoretical studies (Longuet-Higgins and Stewart, 1960; Tolman, 1990; Masson, 1996; Jones, 2000; Ardhuin et al., 2017; Wang and Sheng, 2018; Peureux et al., 2021; Ho et al., 2023; Halsne et al., 2024). These local regional studies have set the physical framework for understanding the H_s variations resulting from a combination of current-induced convergence, refraction, and Doppler shifting. It is apparent from the diversity of observations in previous work that these mechanisms affect wave heights in varying ways, influenced by the regional bathymetry as well as near- and far-field currents and winds. For example, in certain coastal regions H_s may vary up to 50% over a tidal cycle, or modulate the incident period and direction of waves. Additionally, diurnal winds (Gille et al., 2003) and inertial currents (Gemmrich and Garrett, 2012) can lead to variations in wave height on the order of meters. As these gradients over short time scales can significantly impact flooding and inundation (Battjes et al., 1987; Stockdon et al., 2006), characterizing these periodic variations in nearshore wave climates can help us understand the implications at the shoreline. Generally, this poses an important operational forecasting challenge: the prediction of ocean wave statistics with high temporal fidelity. To better understand how these different processes, mechanisms, and forcing manifest in the surface wave field response, we characterize the spatial and seasonal variability. Broadly, by statistically quantifying the transfer of energy between ocean currents and winds to ocean waves, including an analysis of the full wave spectrum beyond bulk parameters, we can better inform how wave-current interactions can affect swell-dominated processes (e.g. inundation, altimetry sea-state bias) or windsea-dominated processes (e.g. air-sea interactions, Bragg scattering).

In this study we utilize long-term historical wave records to characterize tidal variability in North American and Pacific Island wave climates. We present analysis of 20 years of historical wave records and identify strong semidiurnal, diurnal, and inertial variability in bulk and spectral wave parameters. We demonstrate how these signatures relate to the tidal environments at the buoy location through spectral analysis of measured surface currents. In Section 2.2, we describe the observations from a moored network of wave buoys and corresponding analysis tools; in Section 2.4 we examine the results of the analysis to show evidence of wave-current and wind-wave interactions in the wave records with both tidal and inertial currents and diurnal winds.

2.2 Data

In this chapter, we use a network of moored wave buoys to characterize inertial, diurnal, and semidiurnal variability in wave measurements. To study the interactions of surface waves with currents, tides, and winds, we aggregate four discrete datasets: in-situ wave measurements from moored wave buoys; anemometer marine wind measurements; in-situ surface current measurements from acoustic current meters; and remotely sensed surface current measurements from high frequency radar. In this section, we summarize the co-located observations of winds, waves, and currents at 249 buoys between 2000-2023, which are further itemized in 6.3.

2.2.1 Moored Surface Wave Observations

A wide network of United States moored wave buoys is maintained and operated by the Coastal Data Information Program (CDIP) at Scripps Institution of Oceanography, which uses moored 0.9-m diameter Datawell Waverider directional wave buoys primarily in coastal waters (Behrens et al., 2024), and the National Data Buoy Center (NDBC), which uses 3-m diameter wind-wave buoys primarily at deep ocean sites (Figure 2.1). Additional wave buoys in Canadian coastal waters are operated by Environment and Climate Change Canada (ECCC). These programs transmit wave data from the buoys via satellite in near-real time. We utilize

the quality controlled archived datasets of wave parameters (H_s significant wave height, T_p dominant wave period, and D_p dominant wave direction) and wave spectra ($E(f)$, where f is wave frequency in Hz) from 249 buoys for the time period 2000-2023. The wave parameters and spectra are computed from 200 second records and averaged at 30 to 60 minute intervals. The CDIP station data are accessed online (cdip.ucsd.edu), the NDBC station data are available in Hall and Jensen (2022) and online (ndbc.noaa.gov), and the ECCC station data are accessed from Marine Environment Data Section of the Department of Fisheries and Oceans Canada (2023). Because of high frequency wave damping due to the large buoy hull (Mudd et al., 2024), we do not consider NDBC in our analyses of $E(f)$.

2.2.2 Surface Current Measurements

Co-located long time series of in-situ observations of both waves and currents are sparse. Since 2020, 22 CDIP stations have been deployed with Datawell Waverider 4 (Datawell B.V., 2021) that are equipped with an acoustic current meter (ACM) to provide direct observations of surface currents. In the hull of the these buoys, three acoustic transducers with 2MHz acoustic frequency measure the current velocity between 0.5m and 1.75m from the surface. Stations with at least 6 months of surface current measurements from ACM are used in this study and are highlighted in orange in Figure 2.1.

Where in-situ observations are limited, we leverage other observations of surface currents from shore-based remote sensing stations, such as the high frequency radar (HFR) United States coastal network with coverage in certain regions along the East and West Coast since 2010 (Terrill et al., 2006; Harlan et al., 2010). HFR measurements have been validated with in-situ surface current measurements and provide unique spatial and temporal coverage (Paduan and Washburn, 2013). We co-locate each wave buoy station to the nearest grid point from the 6km interpolated hourly HFR datasets. In total, between ACM and HFR measurements of ocean surface currents, 109 buoys have either in-situ or remote coverage for over 6 months. We consider both vector currents in a E-N coordinate system (u, v), and currents rotated into the direction of

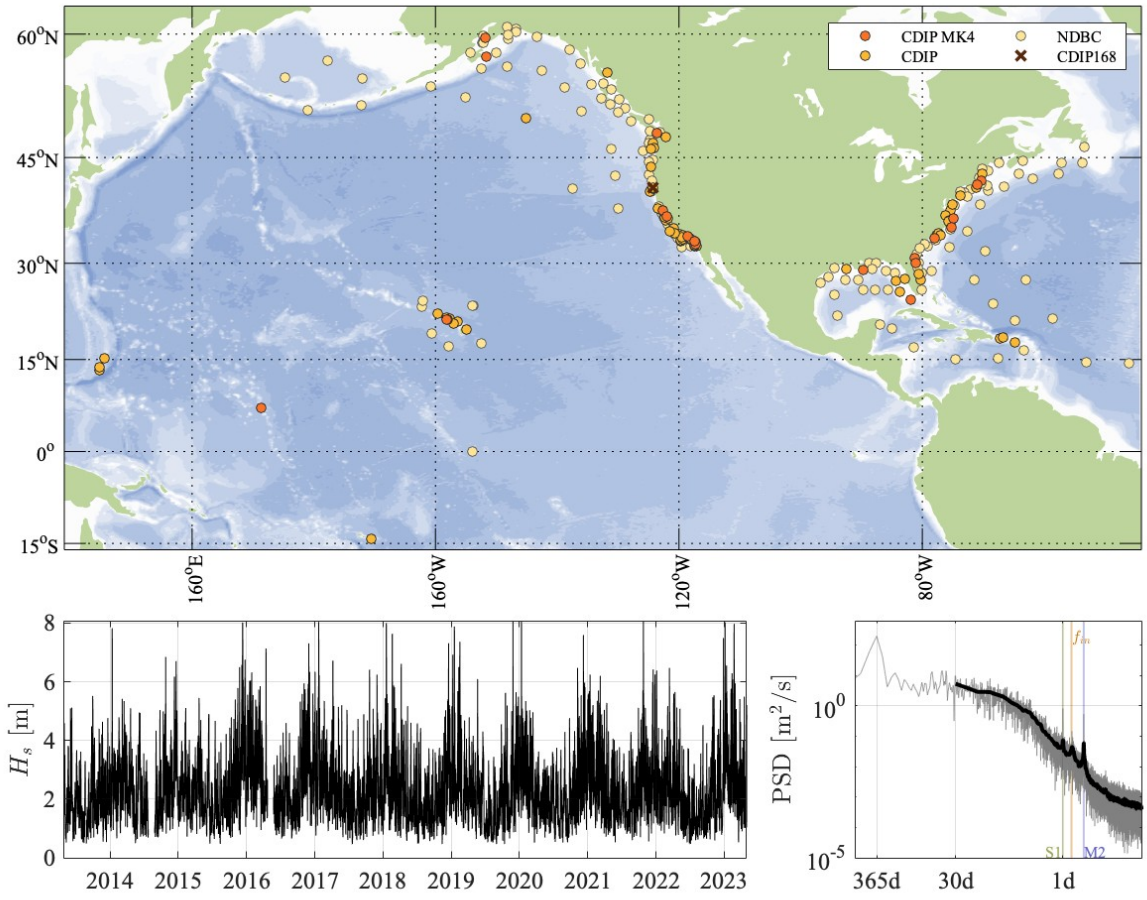

Figure 2.1. (Top) Map of currently operational CDIP (dark yellow) and NDBC stations (light yellow). Buoys with acoustic current meters are highlighted in orange. (Bottom) Example spectral analysis for CDIP station 168 (Humboldt Bay, CA) noted in map. (Left) Time series of significant wave height over past ten years. (Right) Spectrum of significant wave height of a ten year record with segment length of two years (gray) and 90 days (black). The power spectral density highlights modulation at the diurnal, semidiurnal, and inertial bands.

the peak wave direction D_p averaged over 24 hours (U_θ).

2.2.3 Tide Model Predictions

At each buoy location, predicted tidal currents (u, v) and water levels (z) are obtained from the data-assimilated global barotropic tidal model TPXO 9 and Tide Model Driver 2.5 (Egbert and Erofeeva, 2002; Erofeeva et al., 2020). Surface current predictions are used as a

third available source of tidal current information for locations where neither in-situ or HFR surface current measurements are available.

2.2.4 Meteorological Observations

Lastly, we use wind measurements from NDBC meteorological buoys, corrected for anemometer height using Hsu et al. (1994) to 10 meters above the surface. When applicable, we co-located wave buoy stations without meteorological measurements to the nearest NDBC meteorological buoys, constraining the co-locations to distances closer than 50 km, about the decorrelation length scale of nearshore wind fields in reanalysis models and the sampling criterion used in altimeter-buoy comparison (Dobson et al., 1987; Monaldo, 1988).

2.3 Methods

To characterize the high frequency variations related to tides, diurnal winds, and inertial currents, we compute spectra of bulk and specttral wave observations (H_s, T_p, D_p, and $E(f)$) current observations, (U_θ and (u, v)), wind observations (U_{10}), and tidal water levels (z). Spectra are computed by taking the fast Fourier transform of the demeaned and detrended time series over 60-day segments (50% overlap, Hanning window). Both the power spectral density (PSD) and amplitude spectral density (ASD) are computed, where the ASD is the square root of the PSD and is used to infer the modulating amplitude in the original units of the signal. The variance lost due to windowing is corrected by rescaling. An example power spectrum of significant wave height at Humboldt Bay, CA (CDIP 168), averaged over ten years from 2013-2023, is shown in Figure 2.1; the spectrum computed from 750-day segments is also shown. In addition to the peak corresponding with the annual cycle at 365 days, strong peaks are apparent in the diurnal (1 cpd or 24 hours), semidiurnal (1.94 cycles per day or 12.42 hours), and inertial (1.31 cycles per day or 18.29 hours at 40.9^{o}N) bands. For the analysis in this study, spectra are also averaged over the entire record or averaged by year and season (binned into boreal winter from December to February or boreal summer from June to August) to diagnose inter-annual

variability. Cross-spectra between wave, current, and wind measurements are also computed from the 60-day segments to calculate the phase and coherence. Lastly, we exclude NDBC platforms from spectral analysis of $E(f)$ as the damping of high frequency measurements due to the large hull contaminates the measurements (Mudd et al., 2024). The power spectra of a measurement V will be referred to as X^V.

Power spectra of the significant wave height records typically have spectral slopes between -2 and -3, as evident in the example in Figure 2.1. The background spectrum is computed by fitting a power law $X = \sigma^n$ to the spectrum between 0.25 and 3 cycles per day. Significant periodic signals are then identified only if the power spectrum is than the spectral uncertainty; that is, $X^V > \delta X_0^V$. Uncertainty is computed from the number of segments that are averaged to compute each spectra. To compare the relative variability in the wave records at the diurnal, semidiurnal, and inertial frequencies, we compute the integrated variance above the background as a percentage of the total variance on timescales shorter than 0.5 cycles per day. The bandwidth of integration around a center frequency σ_0 is $\{c^{-1}\sigma_0, c\sigma_0\}$, where the bandwidth parameter $c = 1.07$ (e.g. Alford, 2003).

2.4 Results

Wave observations are analyzed for 249 moored buoys with continuous coverage for at least two years of the twenty-four year period from 2000-2023. Geographically, 143 buoys are located in the Pacific, including 24 at Pacific Islands and 22 off Alaska. In general, these buoys experience strong winter storm waves from the North Pacific and long period summer swell propagating from the Southern Ocean, often creating bi-modal sea states. 67 buoys are located in the Atlantic, which experience seasonal local swells from nor'easters, hurricanes, and trade winds. 24 buoys are located in the Gulf of Mexico and 9 are located in the Caribbean. The long term and synoptic scale patterns of the moored buoy network reflect the characteristics of their respective wave basin. Buoys in the Pacific observe the longer periods and higher wave heights

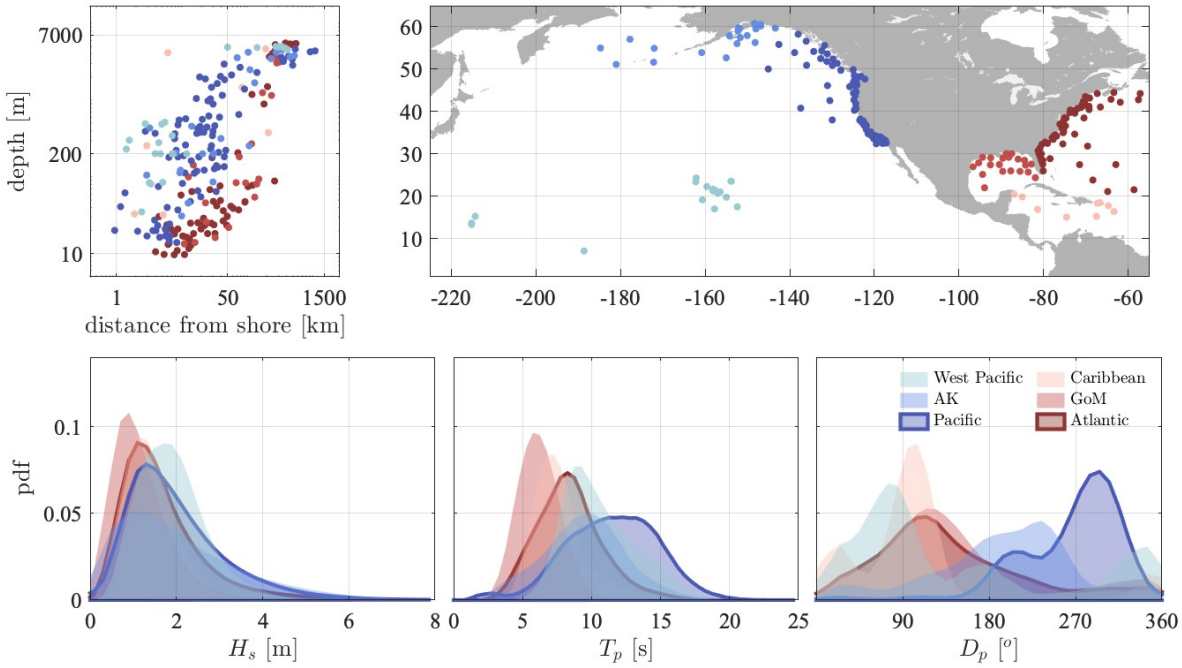

Figure 2.2. For each buoy, distance from shore vs mooring water depth, colored by region. Red colors indicate buoys located in Atlantic, including the Caribbean and Gulf of Mexico, and blue colors indicate buoys located in the Pacific, including Alaska and West Pacific islands (Hawai'i, Guam, Palau, and American Samoa), indicated in map on right. Probability distribution of bulk parameters (H_s, T_p, and D_p) for each region are shown in bottom panels. Pacific wave climates observe larger wave heights and longer periods due to the larger ocean basins. Note the bi-modality of peak periods on the West Coast.

than those in the Atlantic (Figure 2.2).

Buoys also are non-uniformly distributed in mooring depth and distance from shore (Figure 2.2). In total, 43% (N=107) of buoys in the network are moored in 200 meter water depth or less and within 50 km from shore; 26% (N=65) are moored in 200 meter water depth or greater and further than 50 km from shore. The remainder of the buoys are differentiated by regional differences in continental shelf width, i.e. close to shore in deep water (West Coast narrow continental shelf or steep bathymetry around Pacific islands) or far from shore in shallow water (East Coast wide continental shelf), as seen in Figure 2.2.

2.4.1 Regional patterns in periodic wave height records

Dominant periodic signals in wave height records are identified from the power spectra averaged over the duration of each record. We observe modulations to H_s at semidiurnal (M2), diurnal (S1), or inertial (f_{in}) frequencies at the majority of buoy locations. In total, 87% of the buoys have significant energy at at least one of these three constituents, 75% of the buoys have significant energy at M2, 58% have significant energy at S1, and 23% have significant energy at f_{in} (Table 2.1).

Table 2.1. Number of buoys with power spectrum with signals at specified constituents (M2, S1, and f_{in}) in significant wave height H_s, and as a percent of total buoys (N=249). Signals are chosen based on existence of a peak greater than the spectral uncertainty for the background power spectrum ($X^{Hs} > \delta X_0^{Hs}$).

constituent	period [hours]	N (%)
M2	12.42	194 (77%)
S1	24	154 (62%)
f_{in}	$2\Omega \sin\theta$	82 (33%)

To study the relative contributions of the diurnal, semidiurnal, and inertial bands to the wave height records, we compute the relative variance at each buoy, following Section 2.3. The relative variance in the diurnal, semidiurnal, and inertial bands is shown for each buoy across the array (Figure 2.3). Diurnal signals are prevalent in wave records at lower latitudes and closer to shore, and are notably dominant in the Southern California Bight region. semidiurnal modulations exist in most regions covered by the moored array with varying magnitude, aside from the Gulf of Mexico or in the offshore Atlantic. Often the strongest semidiurnal signals are observed in buoys located in channels or enclosed bays (e.g. CDIP 240 in Chesapeake Bay, VA; CDIP 248 in the Strait of Juan de Fuca, WA; CDIP 204 in Cook Inlet, AK) and at the mouths of river or bay inlets (e.g. CDIP 233 in Pearl Harbor, HI; CDIP 142 off the San Francisco Bay, CA). Strong semidiurnal signals also occur off the coast of Florida, the Gulf of Maine, Puerto Rico, Guam, Alaska, and in various locations off the Coast of California. Several of these locations are

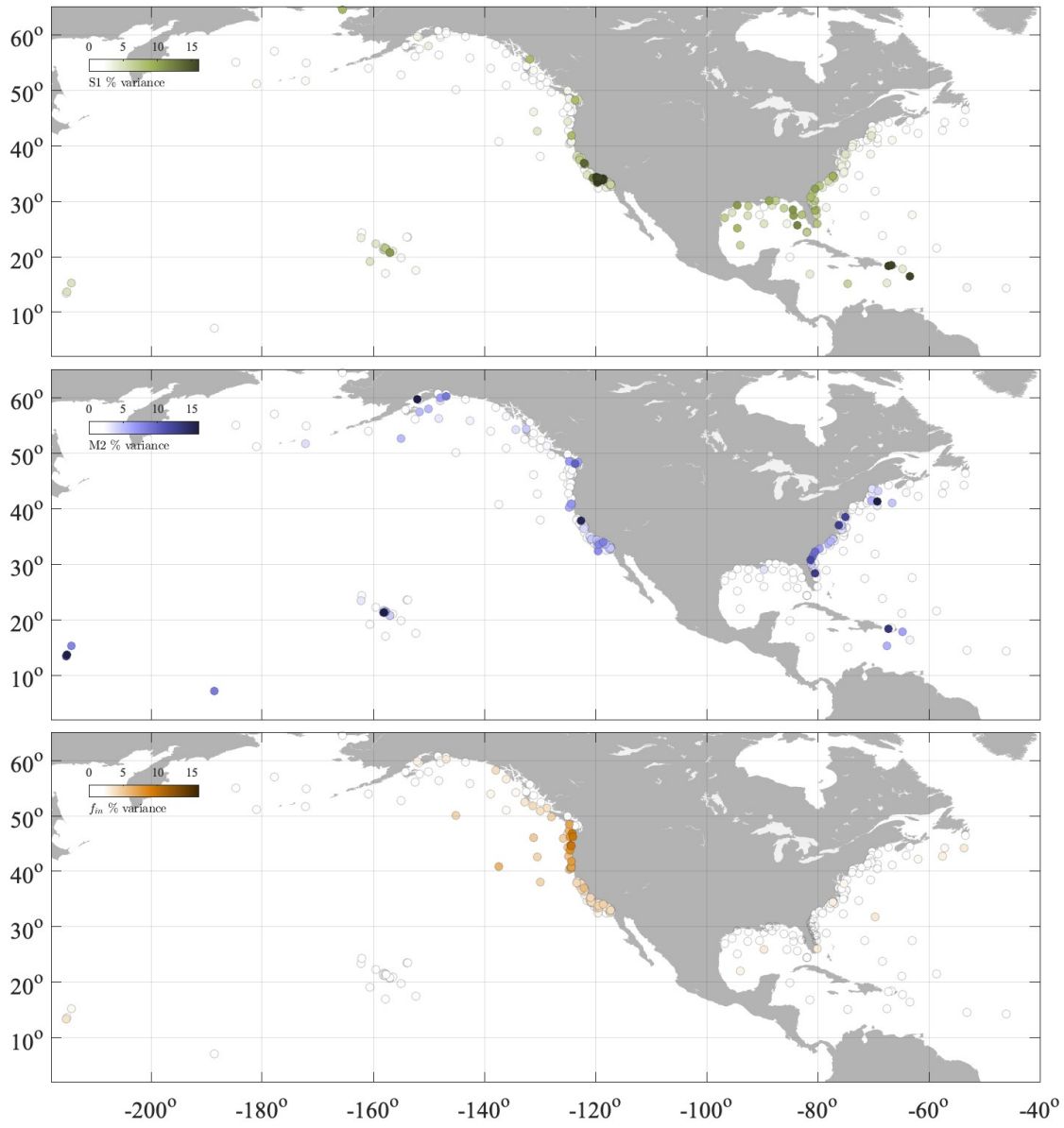

Figure 2.3. Map of semidiurnal (M2) diurnal (S1) and inertial (f_{in}) energy in H_s, reported as the energy above the background of each constituent as a percent of total energy between O(0.5-6cpd). The empty circles indicate buoys with no significant signal ($X^{H_s} < \delta X_0^{H_s}$) in H_s at that constituent. Inertial variance is not computed for buoys where f_{in} is within 0.15 cycle per day of the diurnal or semidiurnal band (these locations denoted with an x). A number of buoys are affected by these periodic signals, some that contribute substantially to the total variance.

well known for extreme tides or enhanced baroclinic tidal energy. Inertial signals are weak in the Atlantic and most dominant in the north east Pacific off the coast of British Columbia and the

Northwest of the United States.

In total, inertial, diurnal, and semidiurnal variability can account for a significant percent of the variance at frequencies less than 0.5 cycles per day within wave records. On average, M2 modulations account for $2-12\%$ of the the total variance, S1 modulations accounts $3-16\%$ and inertial modulations accounts $2-5\%$ of variance less than 0.5 cycles per day in H_s. These results suggest that without including tides or inertial currents in numerical wave models, we may miss up to 20% of the variability in surface wave heights on time scales shorter than two days.

2.4.2 Seasonal patterns in H_s, tidal currents, and winds

To study seasonal patterns in wave height modulations, we average spectra of H_s, currents, and winds by month, (Figure 2.4). Three example buoys with distinct seasonal variability in wave height between 1 and 2 cpd are shown. At time scales longer than 2 days, all buoys observe broad seasonal structure with strongest energy in winter months, in phase with the patterns in the wind observations and consistent with the coupling of winds and waves at the synoptic scale. Between 1-2 cycles per day, distinct patterns in the wave observations pair with the observations of winds and currents. Strong semidiurnal energy is apparent in both the wave and current measurements at CDIP132 located off the east coast of Fernandina Beach, FL. Strong diurnal modulations in both the winds, waves, and currents are observed at CDIP28 located in Santa Monica Bay, CA, with a maxima in summer months. NDBC46029 located west of the Columbia River Mouth, OR has enhanced broadband energy around the inertial frequency (1.44 cpd) with maximal inertial energy in surface currents in early spring and late fall.

The monthly spectra suggest there is a relationship between wave heights and local winds and inertial and tidal currents. At diurnal frequencies, it is challenging to separate the effects of wind forcing and tidal currents. We observe that diurnal variations in wave heights are related to local winds, and that these modulations are prominent in the high-frequency components of the wave spectrum. Further details of diurnal signals are discussed in Section 2.6.1. We focus on

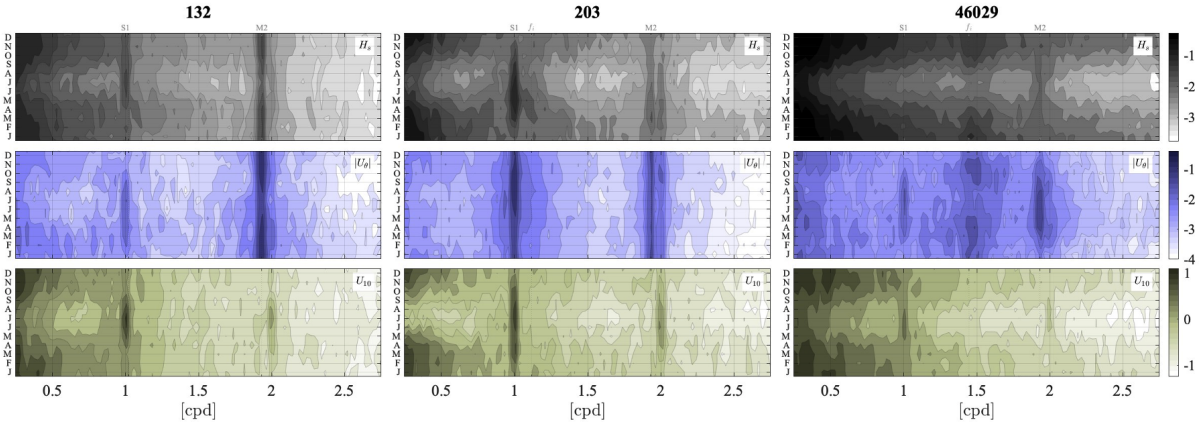

Figure 2.4. Binned monthly averages of spectra of significant wave height (top, gray), currents in wave direction (middle, purple), and wind speed (bottom, green), not normalized for background variance. (Left) CDIP132 (16 m depth) located off the east coast of Fernandina Beach, FL; (middle) CDIP28 (387 m depth) located in Santa Monica Bay, CA; (right) NDBC46029 (131 m depth) located west of the Columbia River Mouth, OR. Seasonal trends in wind and currents map to patterns in wave height between 1-2 cycles per day; winds exhibit mostly diurnal variability amplified in the summer which correlates to the diurnal signals at CDIP132 and CDIP28. Inertial currents enhanced in the winter correlate to the inertial signal in NDBC46029.

wave-current interactions in the inertial and tidal bands, which are poorly resolved in operational wave models, and investigate how modulations in wave heights are related to local currents at the buoys.

2.4.3 Inertial wave height modulations

Inertial motion arises from perturbations in surface wind stress that are balanced by the Coriolis force, generating oscillations observed in current measurements as rotary currents at the inertial frequency. An example of H_s modulations at inertial frequencies (1.5 cycles per day) shows variations of more than 1m off the coast of northern California (Figure 2.5). H_s modulations are observed to be in phase with strong inertial currents exceeding 30-40cm/s, wave heights increase on following currents. During this time period, waves with average peak period at 12 s propagate from the northwest at 300^o. This record represents an example of local inertial currents driving variations in significant wave heights. As there is no wind event

in the wind measurements during this period, we expect that the inertial currents observed at these buoys are from near-inertial waves that propagated from generation at nearby storm. We observe that inertial modulations in H_s exist intermittently throughout the wave record, despite leading to large changes in H_s. This is likely related to the natural intermittency in the generation mechanism of near inertial oscillations.

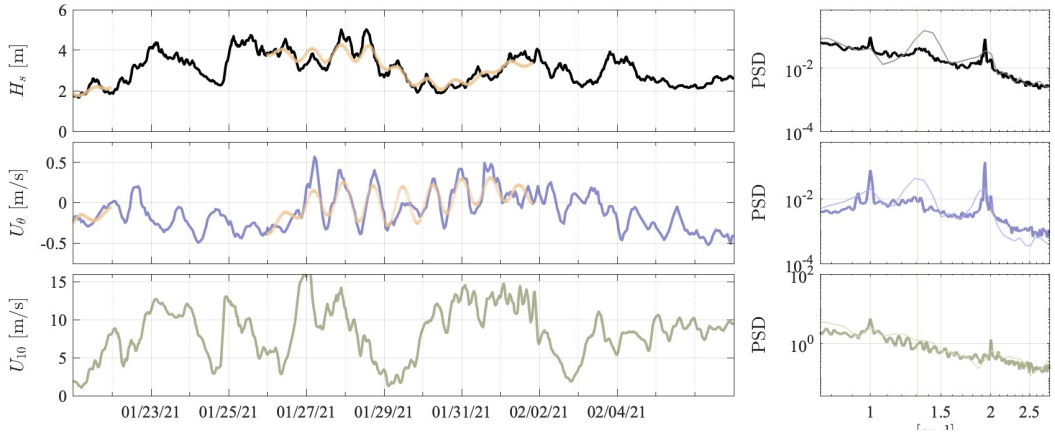

Figure 2.5. Measurements of inertial modulations to H_s. Measurements of significant wave height (top panels), surface currents in dominant wave direction (middle), and wind speed (bottom), are from CDIP buoy 168 and NDBC buoy 46022, located off the coast of Northern California, over the two week period from 2021-01-30 to 2021-02-08. Average spectra of each measured quantity over the entire record are shown in the panels to the right of the two-week time series. H_s and U_θ bandpassed at the inertial frequency is shown in orange.

Inertial signals are also observed in the wave measurements at buoys between 35-60^{o}N along the US West Coast (Figure 2.6), consistent with previous observations of inertial modulations in deep-water wave observations (Gemmrich and Garrett, 2012). Significant inertial modulations are also observed in coastal and shallow-water observations. The maximum contribution from inertial frequencies to variability in significant wave heights occurs between 43^{o}N and 50^{o}N. The increase in inertial energy northwards has been documented in HF radar in Kim et al. (2011), due in part to the increase in strong winds and enhanced near inertial current velocities in the North East Pacific (Alford and Whitmont, 2007; Wang et al., 2023). Inertial signals in H_s are also strongest in the winter on the West Coast, consistent with seasonal trends in storm activity in the North East Pacific and surface current measurements at the buoys. Inertial

signals are also observed at a few buoys in deep water and high latitude on the U.S. East Coast, but are weak compared to the observations on the West Coast.

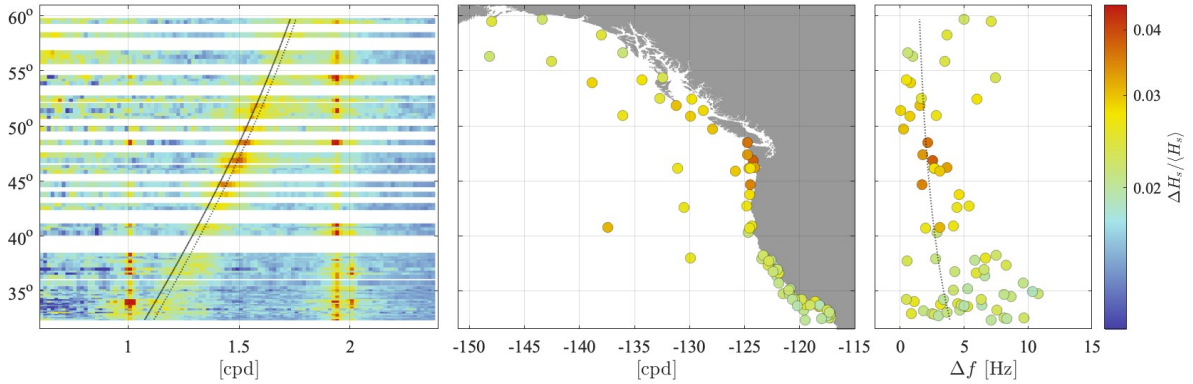

Figure 2.6. (Left) normalized spectrum of H_s as a function of cycles per day, plotted at the latitude of the respective buoy along the west coast of North America in water deeper than 20 m. (Center) Corresponding buoy location. (Right) Frequency shift in percent as function of latitude for each buoy. The solid black line shows the inertial frequency as a function of latitude. The dashed black line shows the near-inertial frequency defined in Eq. 2.1

We find that the inertial peak in significant wave height is shifted to a higher frequency by 2-10%. Following Gemmrich and Garrett (2012), at mid-latitudes this shift is consistent with that expected for near-inertial oscillations shifted due to finite length scales with minimal vorticity, given the following,

$$f_{nio} = \left(f_{in}^2 + c_n^2 k^2\right)^{1/2} + \zeta/2 \tag{2.1}$$

where ζ is the relative vorticity, c_n is the phase speed of the nth vertical mode, and k is the horizontal wavenumber of the inertial wave. This near-inertial frequency is plotted in Figure 2.6 for $c_0 = 2.2$m/s and $k^{-1} = 100$km and ζ is negligible. The corresponding frequency shift expected is plotted in Figure 2.6 and accounts for the shift in frequency at latitudes with the most inertial energy in H_s between 43^oN and 50^oN. The frequency shift decreases with latitude, where buoys in lower latitudes exhibit stronger frequency shifts (up to 10%) of the inertial peak (Figure 2.6). The enhanced frequency shifts south of 40^o could be due to variation in internal tide wavenumber, changes in local vorticity, remotely generated southward propagating near-inertial waves, or interaction with diurnal currents.

2.4.4 Semidiurnal wave height modulations

A representative example of observations off the east coast of Florida show strong M2 tidal currents lead to modulations in H_s and a peak in the H_s spectrum at M2 (Figure 2.7). Wave heights vary up to 0.3 meters or 30% over a tidal cycle, and increase on the following current. During this time period, waves with average peak period at 10 seconds propagate from the east at a direction of 100^o from North. To examine the relationship between the tidal current and modulations to significant wave height, we test the relationship under the assumptions for stationary wave-current interactions:

$$\frac{\Delta H_s}{H_{s,0}} \propto \frac{U}{c_g} \tag{2.2}$$

Under these assumptions, the strength of the modulation to H_s scales with the amplitude of the current. We compute the average semidiurnal current amplitude from the spectrum of U_θ, the average group speed from the average peak period of each buoy, and the average semidiurnal wave height in accordance with the normalization scheme detailed in the Section 6.2.

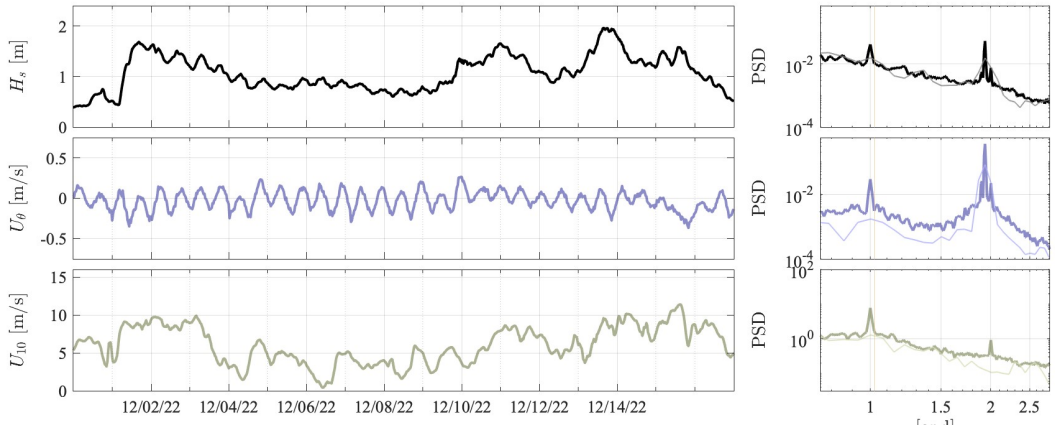

Figure 2.7. Measurements of semidiurnal modulations to H_s. Measurements of significant wave height (top panels), surface currents in dominant wave direction (middle), and wind speed (bottom), are from CDIP buoy 132 and NDBC buoy 41009, located off the east coast of Florida, over a two week period from 2020-09-19 to 2020-10-01. Average spectra of each measured quantity over the entire record are shown in the panels to the right of the two-week time series.

We find that on average, locations with stronger semidiurnal currents coincide with observations of larger tidal modulations to H_s. We find a stronger relationship on the East Coast

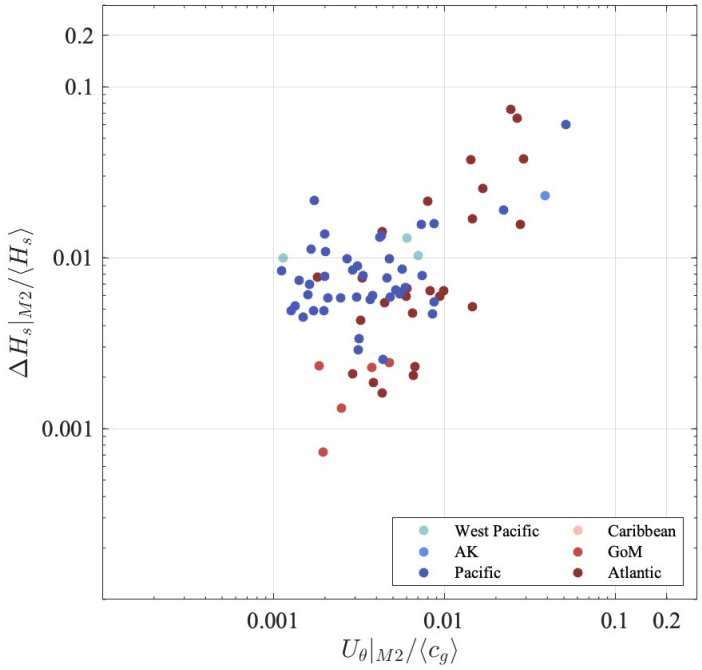

Figure 2.8. Normalized amplitude of H_s modulations at M2 calculated from the H_s spectra vs amplitude of measured surface current at M2, normalized by average wave phase speed, categorized by regions described in Figure 2.2.

relative to the West Coast (Figure 2.8). The normalized M2 wave height, $\Delta H_s|_{M2}/\langle H_s \rangle$, and M2 current variations, $U_\theta|_{M2}/\langle c_g \rangle$, on the East Coast of the United States are highly correlated to the local current amplitude ($r^2 = 0.65$). In contrast, modulations in H_s are weakly correlated on the West Coast ($r^2 = 0.35$). The low correlation on the West Coast may be related to the differences in both tidal and wave climates between East and West Coast, which we discuss in Section 2.5.

2.5 Discussion and Conclusions

We document inertial, diurnal, and semidiurnal modulations in significant wave heights across 249 wave buoys stationed along the U.S. East and West Coasts and at Pacific and Caribbean islands. Our study highlights the necessity of incorporating tidal and inertial currents into numerical wave models to accurately predict wave properties. Stronger diurnal modulations in H_s during the summer are related to the seasonal pattern of measured wind speed, with the most significant relationship observed in the high-frequency portion of the wave spectrum. The co-located measurements of waves and currents suggest that periodic tidal and inertial currents are major drivers of the corresponding periodic signals observed in wave data. In both the inertial and tidal bands, we find wave height variations that are locally and nonlocally forced.

2.5.1 Characteristics of the M2 Tide

Regions with polarized tidal ellipses tend to have local-wave current interaction impacts on the temporal variation of wave height (Figure 2.8). This trend is prevalent on the East Coast, with the modulation in both H_s and T_p readily apparent. In contrast the West Coast wave climate is only weakly modulated by the tidal currents. Figure 2.9 shows the M2 tidal current ellipses predicted by the tidal model and highlights the difference in West Coast and East Coast tidal dynamics resulting from differences in shelf bathymetry Battisti and Clarke (1982). Because of the bathymetry and Kelvin-wave nature of the semidiurnal tide on the West Coast, currents are weak and strongly oriented in the alongshore direction offshore (Miles, 1972). In contrast, the wide continental shelf along the East Coast leads to strong topographically locked currents

that are oriented perpendicular to the shore (Clarke and Battisti, 1981) and amplified across the shelf. The alignment of the tidal current velocities with the incident wave field results in strong interaction.

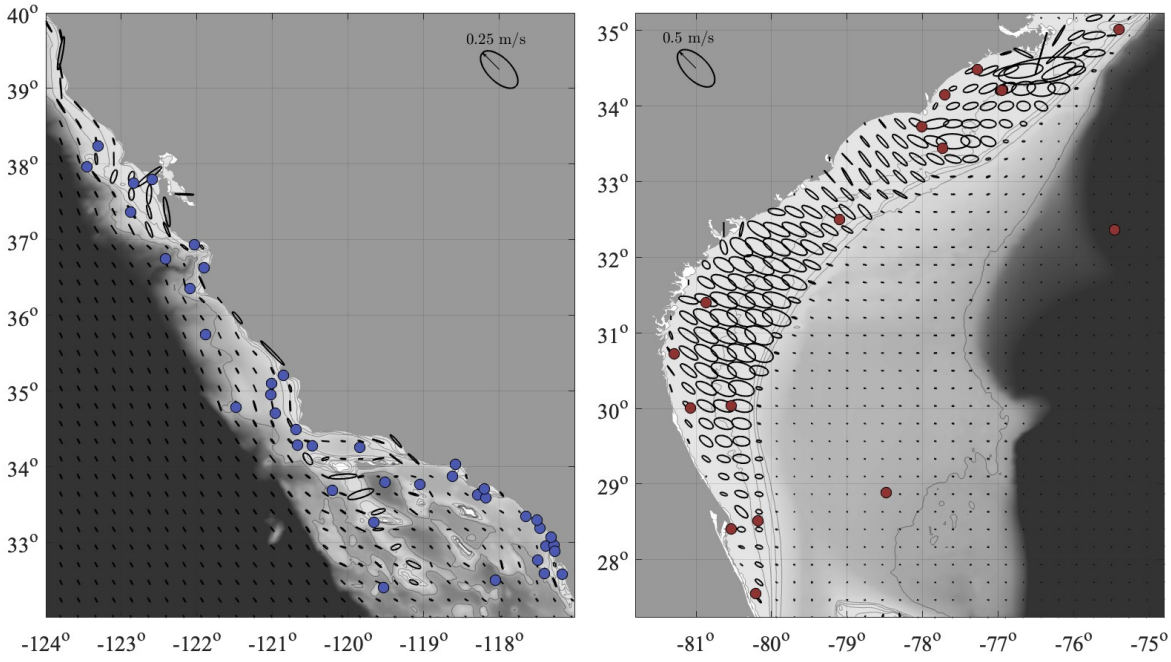

Figure 2.9. Map of semidiurnal (M2) tidal current ellipses predicted by the barotropic tide model for the West Coast (left) and East Coast Florida Bight region (right). Buoy locations within each region are plotted and colored by the regional categorization described in Figure 2.2. Tidal current ellipses scales are shown in the inner corner of each map. Note that the West Coast ellipses are scaled by a factor of 2 greater than the East Coast.

Waves nearby Guam are found to be modulated in the semidiurnal band H_s up to 0.4 meters or 20% over a tidal cycle. In contrast to the eastern seaboard, the predicted barotropic semidiurnal currents are weak ($U_\theta \approx 0.05$ m/s) and in deep water (1600 meters). However, at Pacific islands, baroclinic tides, often with stronger currents, will result in a stronger modulation than what is predicted by a barotropic model (Carter et al., 2008).

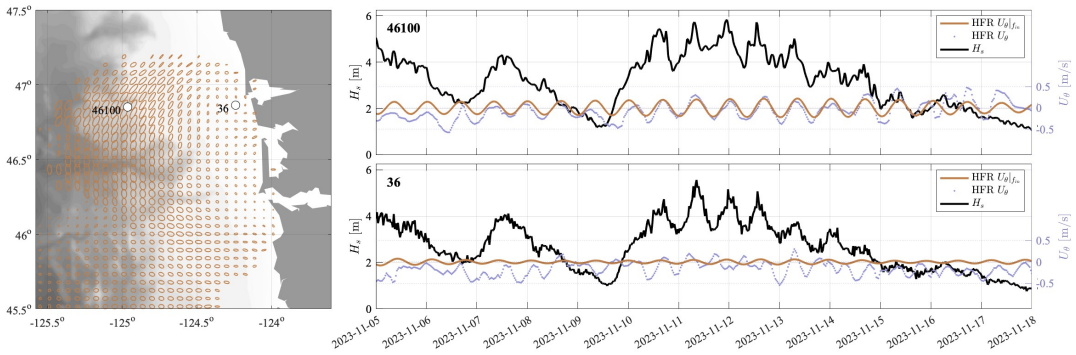

Figure 2.10. Measurements of inertial modulations in H_s (black) from two buoys off the Oregon Coast: NDBC buoy 46100 moored in 582 m water depth (top); CDIP buoy 36 moored in 36 m water depth (bottom). Buoy locations and inertial currents ellipses calculated from HF radar measurements between 2021-11-10 to 2021-11-14 are shown in the map (left). The HF measured surface current U_θ (purple) and the bandpassed inertial current (orange). The nearshore buoy notably observes large inertial modulations to H_s, despite the decay of the inertial current on the continental shelf.

2.5.2 Non-Local Wave-Current Interactions

Not all modulation of the waves, inertial or tidal, have corresponding surface currents in the same band. For example, inertial modulations in two buoys off the coast of Oregon (Figure 2.10) increase by more than 2 meters over an inertial period. At the offshore buoy, inertial currents observed by HF radar are strong (≈ 0.5m/s) and are *in phase* with the modulations to H_s. Onshore, however, the inertial signal is attenuated, evident in both the time series and spectral content. The band-passed inertial currents ellipses, shown in Figure 2.10, reveal a strong decay in close to the coast, likely due to coastal inhibition of the inertial wave and bottom drag (Kim and Kosro, 2013). Modulations to H_s uncoupled to surface currents are also observed at the semidiurnal frequency in certain observations in the Southern California Bight (not shown). These observations indicate that there may be other mechanisms at play that lead to these periodic modulations in wave measurements.

Current-induced convergence and refraction Kenyon (1971); Jones (2000); Wang and Sheng (2018); Bôas et al. (2020) can manifest in non-local effects from transverse current gradients. These effects would not be accounted for with a scaling by the local current magnitude,

leading to the underestimation of H_s modulations. A specific example is the observations off the coast of Oregon: there the inertial currents have an alongshore gradient, which could potentially affect the direction of wave propagation. Additionally, refraction may be particularly important in Southern California where gradients in the internal tide field exist (Kachelein et al., 2023). Additionally, the interaction of tidal currents with the complex bathymetry and islands may introduce tidal vorticity (DiGiacomo and Holt, 2001; Srinivasan et al., 2019; Puthan et al., 2021), potentially influencing the semidiurnal modulation of wave height observed around Guam, Hawaii, Puerto Rico, and the Channel Islands.

The observations emphasize the complexity of the interactions and influence of multiple processes at play in modulating the observed spectrum of H_s. For strong currents, wave-current interaction may be dominated by the effects of local currents and unsteadiness. In this regime strong correlation exists between the measured local current directly to the tidal modulations to H_s. However for weak and variable tidal currents, the effects of convergence and refraction from non-local currents also influence the signal. This discussion remains purely qualitative, as it is not fully understood how and under what regimes non-local and local currents can lead to periodic changes in H_s. Because the non-local convergence effects are highly sensitive to incident wave direction and small current gradients, this makes the resulting H_s signal sensitive and intermittent. Lastly, quantifying the impact of non-local wave-current interactions at a fixed observer requires resolving ocean currents in coastal regions with high spatial and temporal fidelity, which is an active area of research.

This chapter presents evidence that observed modulations of H_s are a result of both local and non-local processes. This requires knowledge of the bathymetry both at the observed site and along the propagation path, the incident wave field, and spatio-temporal measurements of the ocean currents at relatively high resolution and for long periods of time. These observational criteria pose significant challenges.

2.6 Appendix

2.6.1 Diurnal wave height modulations

Wave height modulations at S1 are most coherent with wind measurements, particular for the partitioned spectra for the high frequency seas band, defined as

$$H_{s,seas} = 4\sqrt{\int_{2f_p} E(f)\,\mathrm{d}f} \tag{2.3}$$

The amplitude of the S1 modulation of $H_{s,seas}$ is highly correlated to the amplitude of diurnal winds estimated from spectral analysis for all regions and seasons (Figure 2.11). We find strong seasonality in both the wind and wave measurements at diurnal frequencies, where diurnal wind speed and thus the wave height response increases during the summer. The seasonality is likely related to the enhancement of diurnal sea-breeze amplitude with proximity to coast and during the summer when the land-sea temperature gradient is strongest (Gille et al., 2003), which is also consistent with observations of stronger diurnal winds at buoys closer to the coast.

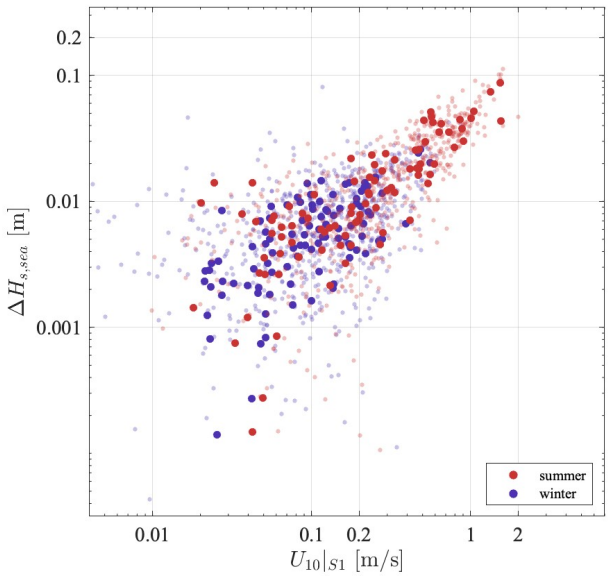

Figure 2.11. Amplitude of $H_{s,sea}$ modulations at S1 vs amplitude of measured wind speeds at S1, categorized by season.

2.6.2 Wave-frequency-dependence in semidiurnal, diurnal, and inertial modulations

The semidiurnal, diurnal, and inertial modulations have different responses in the wave spectra, $E(f)$. The normalized semidiurnal, diurnal, and inertial variance at each frequency f was computed for each buoy to assess the frequency-dependent response in the periodic signals. The percent variance at each constituent is averaged over all buoys and shown in Figure 2.12 for summer and winter. We find distinct frequency responses for the wind-driven (diurnal) and current driven (inertial and semidiurnal) signals. On average, diurnal variations are dominant at high frequencies in summer. The modulations at inertial periods in offshore buoys is the weakest and predominantly isolated to low frequencies. Lastly, modulations to M2 become significant at frequencies as low as 0.1 Hz (swell), unlike S1 which doesn't reach that amplitude until 0.15 Hz in nearshore and 0.2 Hz in offshore. As most wave energy is contained in the lower frequency swell bands, the stronger modulations in M2 then dominate the response in significant wave height, leading to the higher number of buoys with modulations at M2 in H_s than at S1 (Table 2.1). Overall, the M2 signal dominates the modulation at frequencies $f < 0.25$ Hz year round.

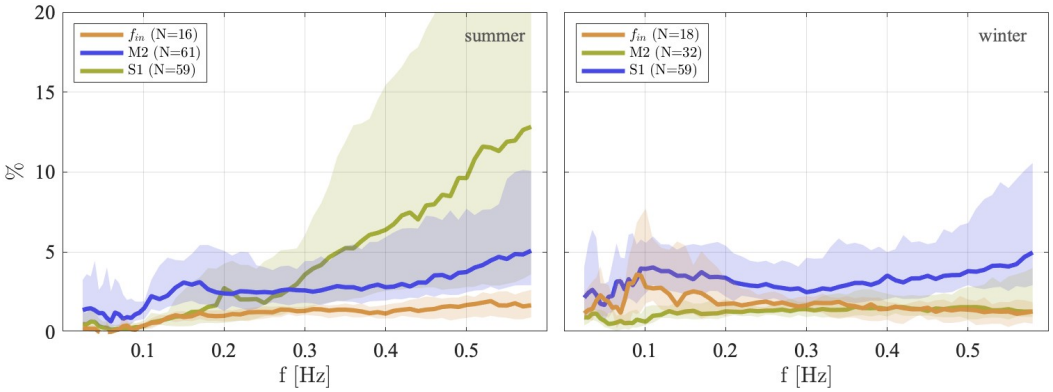

Figure 2.12. The average semidiurnal (M2, blue) diurnal (S1, green) and inertial (f_{in}, orange) energy at $S(f)$ for each wave frequency, reported for each constituent as the energy above the background as a percent of total energy between O(0.5-6cpd) at each frequency. Shaded regions indicate the 25th and 75th percentile. Only CDIP buoys with significant signal ($X^{H_s} < deltaX_0^{H_s}$) in H_s at that constituent are reported, and total number that fall under this criteria is displayed in the legend. Summer averages are on the left, winter averages are on the right.

Chapter 2, in part, is currently being prepared for submission for publication of the material, and is co-authored by Sophia Merrifield and Nicholas Pizzo. The dissertation author was the primary investigator and author of this material.

Chapter 3

Mechanisms for periodic wave modulation

3.1 Introduction

Observations indicate that semi-diurnal and inertial modulations are common features of nearshore ocean wave climates. Though the underlying phenomena are apparent in co-located observations of tides and inertial currents, the exact mechanisms for which the currents impart energy into the wave field is less obvious. Ocean currents act on surface gravity waves through a variety of mechanisms. Most wave-current interaction studies rely on a quasi-stationary approximation which considers the currents and water depth to be stationary at time scales relevant to wave propagation (e.g. Phillips, 1957). Tidal or inertial currents, however, can create both an inhomogenous and unsteady medium for wave propagation, complicating the treatment. The effects of temporally variable tidal currents has been studied extensively beginning with early observations by Unna (1942) and Barber (1949) and later theoretical studies from Longuet-Higgins and Stewart (1960); Tolman (1990); Peureux et al. (2021) and further observational and numerical work from Masson (1996); Jones (2000); Wang and Sheng (2018); Ho et al. (2023). These studies show that tides and currents can modulate waves through a variety of mechanisms. The resulting impact on ocean wave measurements is complex and sensitive to both the ocean current, wave, and environmental conditions. As these phenomena exhibit a wide range of behaviors in the real ocean, this means that the observable modulations in surface waves will be variable both at one buoy location and in cross-comparisons between different locations.

Quantifying how periodic tidal currents, inertial oscillations, water level variations, and diurnal winds impact wave spectra and bulk parameters sets a baseline for understanding the variance related to wave-tide interaction in wave measurements. This then allows us to better understand unique cases that fall outside the classical assumptions (e.g. effects of relative wave speeds between the surface gravity waves and the tides, and non-local refraction).

We highlight several distinct mechanisms for periodic modulations to H_s, and provide simple theoretical discussions of these mechanisms. In Section 3.2 we set up the governing equations. In Section 3.3 we define the results for a stationary approximation of wave current interaction following Phillips (1957). In Section 3.4 we use a simplified model of wave-tide interaction set up in Ho et al. (2023) to represent both the impact of the temporal and spatial gradients in tidal currents and water level variations on wavenumber, frequency, and energy. In Section 3.5, we demonstrate how upstream refraction by transverse current gradients can lead to wave convergence that modulates at the significant wave height at tidal or inertial frequencies via ray tracing (e.g. Masson, 1996; Jones, 2000). Finally, in Section 3.6 we conclude that the mapping between H_s modulations and local and non-local environmental conditions is not bijective. That is, multiple different phenomena may have a similar imprint on significant wave height modulations.

3.2 Governing equations

Ocean currents influence waves through the principles of geometric optics and wave action conservation. Currents can modify the wavenumber, direction, frequency, and energy of the surface waves, which can accumulate to change the bulk parameters and wave spectra. Waves are Doppler shifted by a current as,

$$\omega = \sigma + \mathbf{k} \cdot \mathbf{U} \tag{3.1}$$

where ω is the absolute frequency as observed by a stationary observer, σ is the intrinsic frequency of the waves, $\mathbf{k} = (k, \ell)$ is the wavenumber vector and $\mathbf{U}$ is the current vector. The full

dynamical evolution of the wave field as it responds to winds and ocean currents is governed by a wave action equation, which is conserved in the absence of wind forcing. Wave action at a point in space $\mathbf{x}$ and time t is defined as the ratio between wave energy $E(\mathbf{x},t,\mathbf{k})$ and the intrinsic frequency σ,

$$N(\mathbf{x},t,\mathbf{k}) = \frac{E(\mathbf{x},t,\mathbf{k})}{\sigma(\mathbf{x},t,\mathbf{k})}. \tag{3.2}$$

The wave action conservation equation is,

$$\frac{\partial N}{\partial t} + \nabla \cdot [(\mathbf{U} + \mathbf{c_g})N] = \frac{S_{tot}}{\sigma}. \tag{3.3}$$

where $\mathbf{c_g}$ is the group velocity of the waves and $\mathbf{U} = (U,V)$ is the surface current vector. The term on the right hand side is,

$$S_{tot} = S_{in} + S_{diss} + S_{nl} \tag{3.4}$$

which represents the wind input, S_{in}, dissipation, S_{diss}, and nonlinear wave-wave interactions, S_{nl}. This is where the effects of wind forcing appears. Although there has been significant effort to understand these terms (Janssen, 2003), there is still considerable uncertainty in their behavior. The wind input term is thought to flux momentum and energy into the higher wavenumbers which then cascades to larger scale through nonlinear interactions. Perhaps the most well understood term in the nonlinear interaction term, which in deep water represents four wave interactions, while in shallow water three wave interactions become operable. For our studies, we ignore the impact of these nonlinearities. The dissipation term is typically taken to close the budget, but recent studies have highlighted the potential for this term to have dynamical implications (Romero, 2019). Here, we focus on the wind input term and ignore the dissipation and nonlinear terms.

Given the definitions of the wavenumber magnitude and wave direction,

$$\kappa = \sqrt{k^2 + \ell^2}, \tag{3.5}$$

$$\theta = \tan^{-1}\left(\frac{\ell}{k}\right), \tag{3.6}$$

the left hand side of Equation 3.3 may be rewritten to separate the changes to wave action into components related to advection $\dot{\mathbf{x}}$, wavenumber shifting $\dot{\kappa}$, and refraction $\dot{\theta}$,

$$\frac{\partial N}{\partial t} + \nabla \cdot (\dot{\mathbf{x}} N) + \frac{\partial}{\partial \kappa}(\dot{\kappa} N) + \frac{\partial}{\partial \theta}\left(\dot{\theta} N\right) = \frac{S_{tot}}{\sigma}. \tag{3.7}$$

On the left hand side of Equation 3.7, the equations for the evolution of the wavenumber magnitude $\dot{\kappa}$, wave direction $\dot{\theta}$ are derived from geometric optics which relates change in the wavenumber vector $\mathbf{k}$ to changes in absolute frequency ω to get (Bretherton and Garrett, 1968),

$$\frac{d\mathbf{k}}{dt} = -\frac{\partial \sigma}{\partial h}\frac{\partial h}{\partial \mathbf{x}} - \mathbf{k} \cdot \frac{\partial \mathbf{U}}{\partial \mathbf{x}} \tag{3.8}$$

From this, we derive the equations for the rate of change in θ and κ given the definitions in Equations 3.5 and 3.6. Thus, the system of equations that governs the conservation of wave action is Equation 3.7 and,

$$\dot{\mathbf{x}} = \mathbf{c_g} + \mathbf{U} \tag{3.9}$$

$$\dot{\kappa} = \frac{d\kappa}{dt} = -\frac{\partial \sigma}{\partial h}\frac{\partial h}{\partial s} - \mathbf{k} \cdot \frac{\partial \mathbf{U}}{\partial s} \tag{3.10}$$

$$\dot{\theta} = \frac{d\theta}{dt} = -\frac{1}{k}\left(\frac{\partial \sigma}{\partial h}\frac{\partial h}{\partial m} + \mathbf{k} \cdot \frac{\partial \mathbf{U}}{\partial m}\right) \tag{3.11}$$

$$\dot{\omega} = \frac{d\omega}{dt} = \frac{\partial \sigma}{\partial h}\frac{\partial h}{\partial t} + \mathbf{k} \cdot \frac{\partial \mathbf{U}}{\partial t} \tag{3.12}$$

where $h(x,y,t)$ is the water depth. The coordinates (s,m) are chosen to align s with the wave direction θ and m is perpendicular to s, forming a right handed coordinate system. The total derivative is defined as

$$\frac{d}{dt} = \frac{\partial}{\partial t} + (\mathbf{U} + \mathbf{c_g}) \cdot \frac{\partial}{\partial \mathbf{x}}. \tag{3.13}$$

This set of governing equations (Equation 3.7 and 3.9-3.12) is the basis for modeling ocean waves and backbone for current third-generation numerical wave modeling (WavewatchIII, WAM, SWAN, etc.). Notably, the surface current vector affects Equations 3.10-3.12 differently, thus, there are multiple separate mechanisms for currents to modify wave action through either

the current gradient in the direction of the waves $\frac{\partial \mathbf{U}}{\partial s}$, the current gradient in the transverse direction of the waves $\frac{\partial \mathbf{U}}{\partial m}$, and the temporal gradient of the current $\frac{\partial \mathbf{U}}{\partial t}$. Changes to wave direction only arise from transverse gradients in ocean currents and bathymetry; changes to the wavenumber arise from gradients in the direction of wave propagation; changes to the absolute frequency arise from the temporal gradients. The impact of mechanisms on wave action and subsequently measured wave spectra can differ regionally and temporally depending on the bathymetry, ocean current environments, and wave climate, complicating the interpretation of observations in Chapter 2.

To explore these mechanisms, in this chapter we take several simplifications to these governing equations to understand the underlying mechanisms for different periodic modulation in H_s. As we are specifically interested in solutions for periodic currents, we can prescribe a general form for the currents, comprised of a periodic component $u(\chi)$ multiplicative with some stationary spatial structure $f(x,y)$, where χ describes the phase of the periodic structure of the currents.

$$\begin{aligned} \mathbf{U} &= (U,V) \\ &= (U(x,y,t),V(x,y,t)) \\ &= (u(\chi),v(\chi))f(x,y) \end{aligned} \tag{3.14}$$

For example, as tidal currents propagate with the carrier tidal waves, $\chi = \mathbf{K}\cdot x - \Phi t$. For inertial currents, the periodicity is restrained to the temporal component, $\chi = \Phi t$. We use this framework to discuss the distinct mechanisms for periodic modulation to H_s.

3.3 Stationary wave-current interaction

We solve the system of equations for statistically stationary wave-current interaction in one dimension. In this approximation, the derivatives with respect to time are zero, meaning that the incoming wave field is in a statistically steady state over the time scales under consideration, the coordinates $x = s$ and $y = m = 0$, and $S_{tot} = 0$. Thus, Equations 3.7 and 3.10-3.12 become,

$$\frac{\partial N}{\partial x} = -N\frac{1}{c_g + U}\left(\frac{\partial c_g}{\partial x} + \frac{\partial U}{\partial x}\right) \tag{3.15}$$

$$\frac{\partial k}{\partial x} = \frac{1}{c_g + U}\left(-\frac{\partial \sigma}{\partial h}\frac{\partial h}{\partial x} - k\frac{\partial U}{\partial x}\right) \tag{3.16}$$

$$\frac{\partial \theta}{\partial x} = 0 \tag{3.17}$$

$$\frac{\partial \omega}{\partial x} = 0 \tag{3.18}$$

Solving this asymptotically for small variations to k, U, and N, we obtain the following expressions for change in wave group velocity and energy.

$$\frac{\Delta k}{k_0} = -\frac{U}{c_{g,0}} \tag{3.19}$$

$$\frac{\Delta N}{N_0} = -\frac{U}{c_{g,0}} - \frac{1}{2}\frac{\Delta k}{k_0} = -2\frac{U}{c_{g,0}} \tag{3.20}$$

where the subscript denotes the initial conditions at a point up stream unaffected by the current U, and c_g is the deep water group speed. This approximation acts as a baseline for the effects of currents on waves, wherein modulations to wavenumber and wave action get large when the magnitude of the current U increases, relative to the group speed of the waves.

3.4 Wave-tide interaction

To examine the the effects of tides on surface waves, we utilize a simplified framework for wave-tide interaction established in Ho et al. (2023) and Tolman (1990), which solved the governing equations (Equations 3.7 and 3.10-3.12) under the following assumptions: 1) in one dimension, 2) $S_{tot} = 0$; 3) that the currents and water level vary periodically with a tidal phase $\chi = Kx - \Phi t$ (following Equation 3.14), which allowed the governing equations to reduce a system of ordinary differential equations. This derivation is described in detail in Chapter 4, which we extend here for two dimensions, that is, we allow the direction of wave propagation to be offset from the direction of tidal wave propagation. The tidal current is prescribed as follows,

$$\begin{aligned} \mathbf{U} &= (U, V) \\ &= (U(x, y, t), 0) \\ &= (u(\chi), 0) \end{aligned} \tag{3.21}$$

and similarly,

$$h = h_0 + z(\chi) \tag{3.22}$$

where x is a coordinate oriented along the direction of propagation of the tidal wave, such that $\chi = Kx + \Phi t$ (Figure 3.1). We have taken the y-component of the velocity to be zero to illustrate the basic physics under consideration in a minimal model.

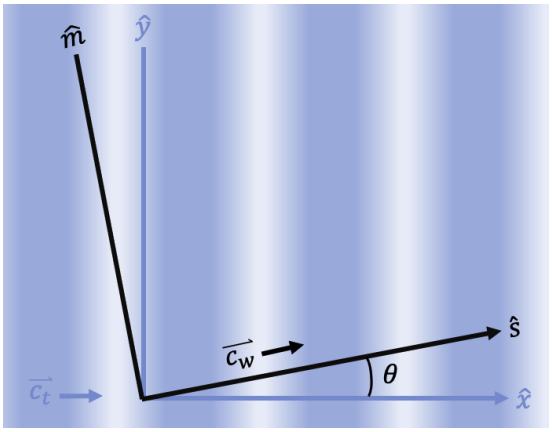

Figure 3.1. Coordinate system for wave-tide interaction. Tidal propagation $\mathbf{c_t}$ direction is fixed to the (x,y) reference frame. Surface waves propagate at speed c_w in the direction θ, aligned with s.

The derivation for the changes in κ (Equation 3.10) with respect to the tidal phase χ is presented in the Appendix 3.7.1. The same derivation is computed for the wave direction (Equation 3.11), absolute frequency (Equation 3.12), and wave action (Equation 3.3) to get the following set of governing equations generalize for an arbitrary direction of wave propagation angle θ,

$$\frac{\partial \kappa}{\partial \chi} = \frac{\cos\theta}{c_t - (U + c_g \cos\theta)} \left(\frac{\partial \sigma}{\partial h} \frac{\partial z}{\partial \chi} + k \cos\theta \frac{\partial u}{\partial \chi} \right) \tag{3.23}$$

$$\frac{\partial \theta}{\partial \chi} = \frac{\sin\theta}{c_t - (U + c_g \cos\theta)} \frac{1}{\kappa} \left(\frac{\partial \sigma}{\partial h} \frac{\partial z}{\partial \chi} + k \cos\theta \frac{\partial u}{\partial \chi} \right) \tag{3.24}$$

$$\frac{\partial \omega}{\partial \chi} = \frac{c_t}{c_t - (U + c_g \cos\theta)} \left(\frac{\partial \sigma}{\partial h} \frac{\partial z}{\partial \chi} + k \cos\theta \frac{\partial u}{\partial \chi} \right) \tag{3.25}$$

$$\frac{\partial N}{\partial \chi} = \frac{N}{c_t - (U + c_g \cos\theta)} \left(\frac{\partial u}{\partial \chi} + \frac{\partial c_g}{\partial \chi} \cos\theta - c_g \sin\theta \frac{\partial \theta}{\partial \chi} \right) \tag{3.26}$$

This models the refraction and wavenumber shifting of the wave spectra due to tidal currents and water level variations. Notably, the changes in wavenumber and wave direction is dependent on the angle between the tide and the surface waves. If waves are aligned with the direction of tidal wave propagation $\cos\theta = 1$ and $\sin\theta = 0$: there are no affects to the wave direction. If waves propagate at an angle oblique to the direction of tidal propagation, e.g. $\theta = 45^o$, both refraction to the wave direction and wavenumber shifting occur. We return to the governing equations in Ho et al. (2023) for the one-dimensional approximation by setting $\theta = 0$ such that the waves propagate in the same direction as the tide, and defining $u(\chi) = A_u \sin\chi$ and $z(\chi) = A_h \sin\chi$.

3.4.1 Simulations

To better understand the range in H_s variations that this predicts, we run an ensemble of simulations exploring the parameter space. For simplicity we use a one-dimensional treatment and ignore the effects of refraction such that $\theta = 0$. We test two different conditions: one with $c_t = 0$, where it is apparent that the governing equations (3.23-3.26) return to the governing equations for stationary currents in Section 3.3, which we call the stationary approximation, and one with $c_t = \sqrt{gh_0}$, to represent the effects of tidal currents with temporal and spatial gradients, which we call the tidal approximation. We are interested in the response in H_s to different water depths h_0, current amplitudes A_u, water level amplitudes A_h, and initial wave spectrum $E(f)$ that is prescribed by a JONSWAP spectrum with different inherent significant wave heights H_s and peak periods T_p. To do so, we employ a 4th-order Runge-Kutta method to solve Equations 3.23-3.26. We examine the change to H_s for these five different parameters under the range of conditions outlined in Table 3.1. In total, we run 210,000 different simulations to compute the modulated wave spectrum $E(f)$ and compute resulting change to the bulk parameters T_p and H_s.

We first test the assumption that the modulation to H_s is proportional $H_{s,0}$, as (3.7) implies. This will allow us to move forward with the assumption of the multiplicative form of H_s

Table 3.1. Values of parameters in simulation (water depth h_0, current amplitude A_u, water level amplitude A_h, initial significant wave height $H_{s,0}$, and initial peak period $T_{p,0}$) and total number of values for each parameter (N).

h_0 [m]	15, 20, 30, 50, 75, 100, 200, 500	N=8
A_u [m/s]	0, $\pm$0.05, $\pm$0.1, $\pm$0.2 ,$\pm$0.3, $\pm$0.4, $\pm$0.5, $\pm$0.6, $\pm$0.8, $\pm$0.9, $\pm$ 1	N=25
A_h [m]	0, $\pm$0.2, $\pm$0.4 , $\pm$0.6, $\pm$0.8, $\pm$1, $\pm$1.2, $\pm$1.4, $\pm$1.6, $\pm$1.8, $\pm$2	N=25
$H_{s,0}$ [m]	0.5:0.5:3	N=6
$T_{p,0}$ [s]	7, 8, 9, 10, 11, 12, 13	N=7

modulations due to the currents, that is,

$$H_s(t) - H_{s,0}(t) = \alpha(t) H_{s,0}(t). \tag{3.27}$$

This is illustrated in Figure 3.2. The cumulative distribution of simulated modulations to H_s, calculated as the difference from the initial $H_{s,0}$, is shown in Figure 3.2a. The distributions are sensitive to the initial $H_{s,0}$, that is, initial wave spectra with greater significant wave heights will lead to larger modulations. When we normalize the modulations to H_s by the initial condition, as shown in Figure 3.2b, the dependence on the initial condition collapses. Hereinafter, we present the results of these simulations in terms of the normalized modulation, $\alpha = \Delta H_s / H_{s,0}$, with the knowledge that the absolute value for change to H_s scales with the initial condition. This has the added advantage that it allows us to reconstruct long time series of H_s with variable $H_{s,0}$ easily without having to re-run the simulation for every value of $H_{s,0}$.

Broadly, tidal modulation of H_s increases with increasing current magnitude, in both the stationary and tidal approximations. We specify this general result to account for changes to local water depth and water levels and incident wave spectra. We find the that the relationship between H_s modulation and current magnitude is modified when varying the parameters identified in Table 3.1. This is evident in Figures 3.3 and 3.4 that show predicted changes to H_s at various depths as a function of current amplitude A_u, water level amplitude A_h, and incident peak period T_p. Namely, in shallow water the tidal modulation of H_s increases when coincident with tidal water level variations. For example, in 15 meter water depth (Figure 3.3) change in water

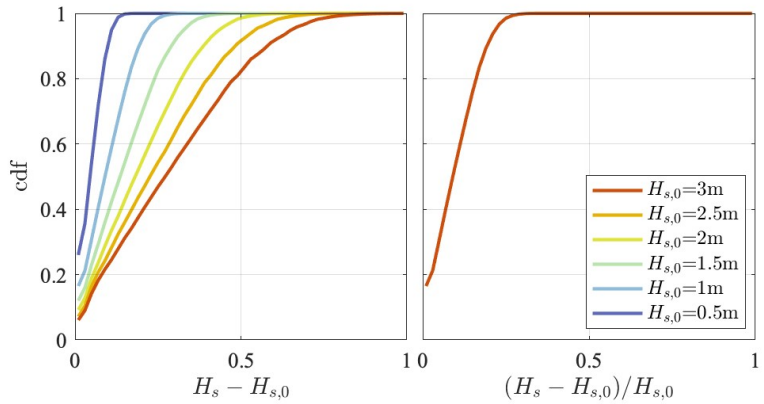

Figure 3.2. Cumulative density functions for the simulated H_s, separated by initial significant wave height $H_{s,0}$. Left shows distributions for change to H_s as $H_s - H_{s,0}$ in units of meters, and right shows distributions normalized by initial condition $H_s - H_{s,0}$, which collapses the curves and shows the insensitivity of this metric to the initial condition.

level of $A_h = 1$ increases the modulations to H_s by 5%. The peak period of the incident wave spectra also changes the response in H_s at all water depths, though this is slightly exacerbated at shallow depths. For incident spectra with peak periods at 8 seconds interacting with an 0.5 m/s current, H_s modulations are 3% greater than for incident spectra with peak periods at 10 seconds. Notably, the relationship between H_s modulations and T_p varies in the tidal approximation. In shallow water, spectra with peak periods T_p longer than 10 seconds observe larger modulations, particularly for fast currents.

Significant differences in the magnitude of H_s modulations can arise between the stationary and tidal approximations. For a wave spectra with a peak period of 10 seconds in 15 m water depth and a 0.5 m/s current magnitude, the tidal approximation predicts a 5% greater modulation to H_s than the stationary approximation. This difference is greater for faster currents and for longer peak periods and becomes less extreme in deeper water.

Sensitivity analysis was performed to assess parameter importance on the relative H_s modulations. We are interested in both the importance of each parameter in predicting H_s modulations as well as the magnitude of H_s modulations over a range of the parameters we

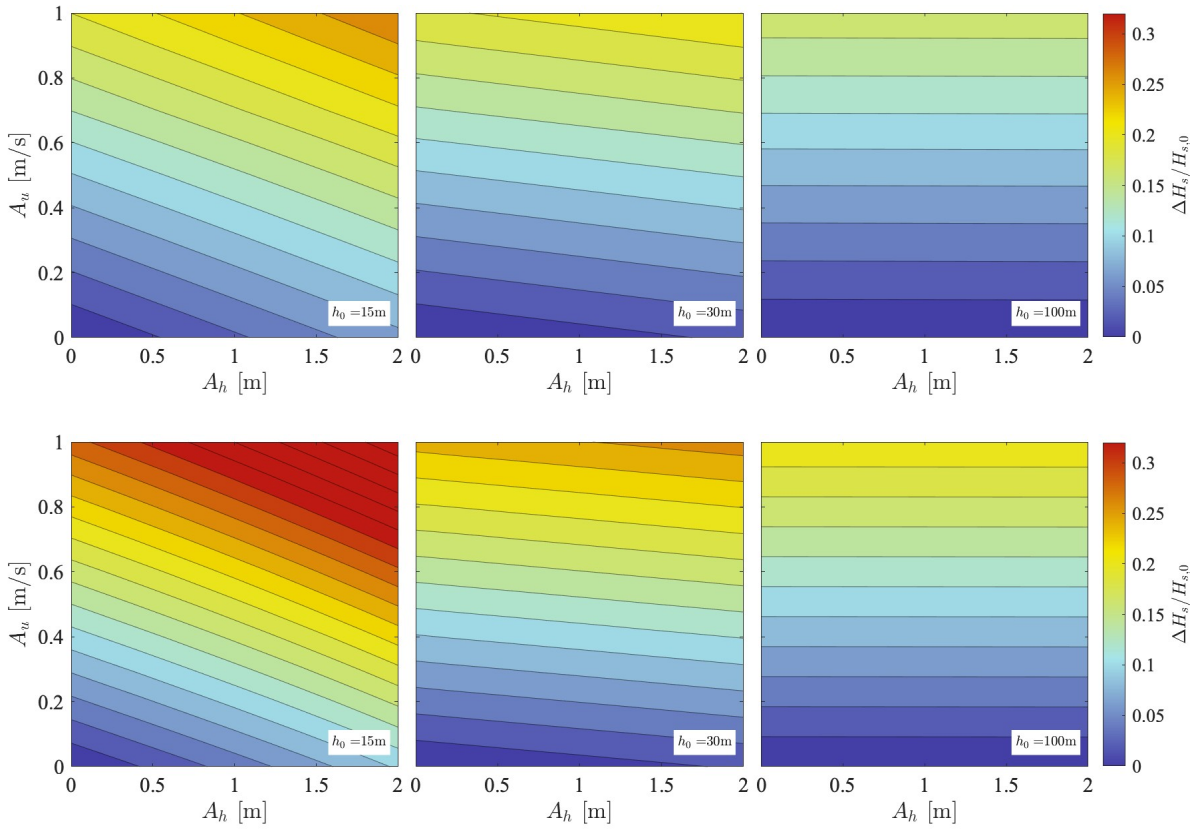

Figure 3.3. Predicted change to H_s, normalized by $H_{s,0}$, as a function of water level change and current magnitudes at various depths. In shallow water depths, the modulation to H_s is enhanced when the change in tidal water level is large, thus, H_s is dependent on both the tidal water level and tidal current. In deep water, the only effect of tides will be through the current. This is shown for the two conditions: stationary wave-current interaction (top) $c_t = 0$, wave-tide interaction (bottom) $c_t = \sqrt{gh_0}$

expect to observe. Both aspects control predictability. We find that the surface current amplitude A_u, is the most important in predicting the resulting H_s modulations, regardless of depth, with correlation coefficients with the H_s modulations above $r^2 > 0.8$ for any water depth. We compare the change in H_s over the expected range of values for each parameter based on the observations in Chapter 3 and find that the variability in peak periods observed at a buoy may lead to variations in H_s modulations of similar order as that expected by surface currents. This motivates the need to understand the influence on background wave conditions (demonstrated here through the sensitivity in our simulations to incident peak period) on H_s modulations, especially when computing statistics over long time windows;

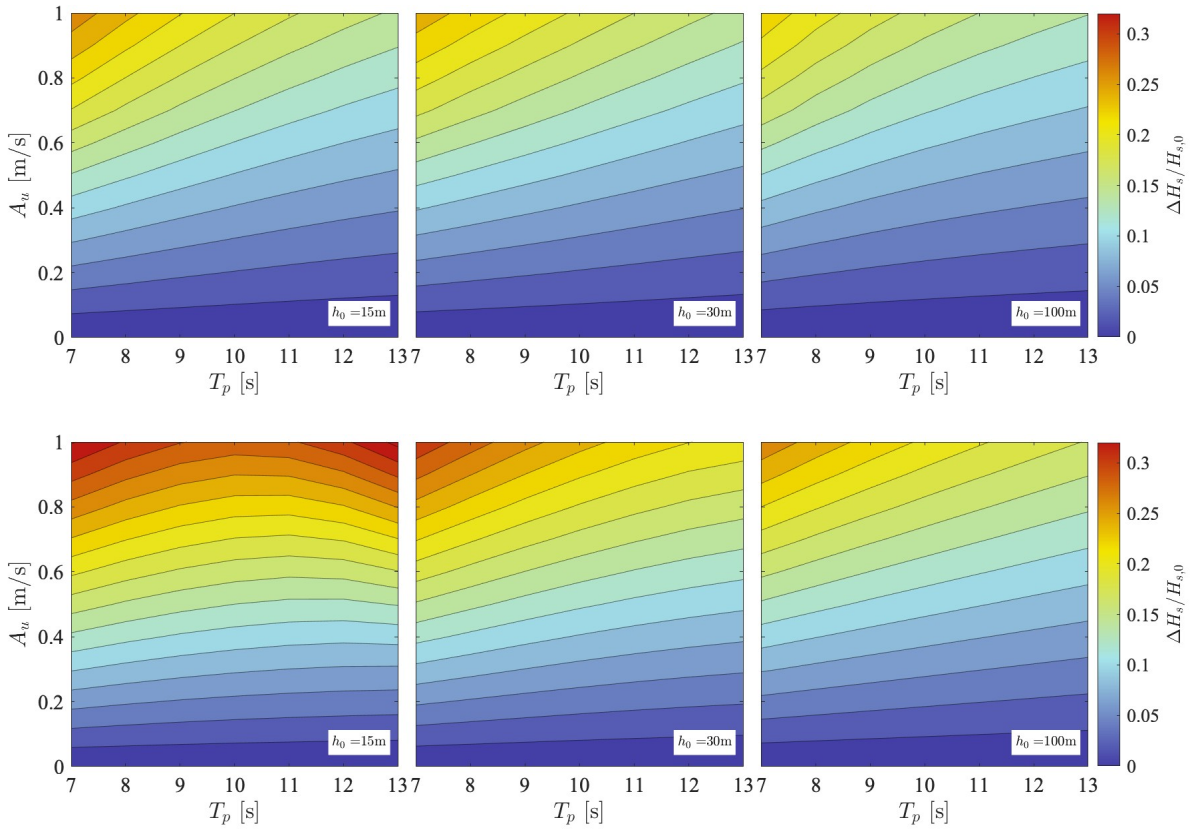

Figure 3.4. Predicted change to H_s, normalized by $H_{s,0}$, as a function of incident peak period and current magnitude at various depths. The change to H_s is sensitive to the initial T_p at all depths, specifically, spectra with shorter peak periods may be more effected by tidal currents. This is slightly enhanced in shallow water.

Given the results of these simulations, we test the importance of several non-dimensional variables in describing the modulations. This will allows us to simplify the wide span of environmental conditions A_u A_h h_0 that exist in the moored buoy network described in Chapter 2. Previously, scaling arguments for modulations to H_s that have been proposed in the literature include stationary approximations (Phillips, 1966) and unsteady and inhomogenous approximations (Tolman, 1990).

We define a unified non-dimensional parameter that represents both the modulations from currents and water depth variations. To do so, we use the stationary form of Equation 3.23 to roughly approximate $\Delta k/k_0$ via asymptotic expansion, and assume that

$$\frac{\Delta H_s}{H_{s,0}} \propto \frac{\Delta E}{E_0} \propto \frac{\Delta k}{k_0} \ll 1 \tag{3.28}$$

which we can roughly approximate via conservation of action to relate to the simulated H_s modulations. The first order asymptotic solutions for small perturbations in k, such that $k = k_0 + \varepsilon k_1$, in response to small perturbations for A_u and A_h is,

$$\frac{k_1}{k_0} = \frac{\Delta k}{k_0} = \frac{1}{c_{g,0}} \left(\frac{1}{k_0} \frac{\partial \sigma_0}{\partial h_0} A_h + A_u \right) \tag{3.29}$$

Note that we have dropped any dependence on χ, as we seek maximum bounds on the amplitude of wave modulation predicted by these expressions, which will occur when the depth variations and current variations are in phase and when $\cos \chi = 1$. We have also scaled the solution for k_1 by k_0. In the limits of small and large kh for to separate this into the shallow and deep water regimes, this becomes,

$$\gamma = \frac{\Delta k}{k} \approx \begin{cases} \frac{A_u}{c_g} + \frac{A_h}{2h} & kh \ll 1 \\ \frac{A_u}{c_g} & kh \gg 1 \end{cases} \tag{3.30}$$

We use this non-dimensional parameter γ to assess the modulations to H_s. This is shown in Figure 6.2 for the subset of estimations that represent each buoy location in the moored array from Chapter 2, based on the buoy's water depth and average measured semi-diurnal current, water level variation, and peak period. The average value of A_u is calculated by averaging a daily envelope of U_θ, the observed currents rotated into the direction of D_p; similarly, average A_h is calculated by averaging a daily envelope of z estimated by the barotropic tide model. The simulated modulations scale well with γ, which demonstrates the utility of γ to predict H_s modulations when driven by local wave-current interaction. For comparison, the observed H_s modulations from the moored buoys are also shown in Figure 6.2. The observation scale reasonably with the non-dimensional term, however, the observations have significant spread, particularly for weak currents. The variability in the observed parameters does contribute to the spread, but not enough to account for the deviations particularly at low γ. Difference may be due to missing physics, which likely include the effects of refraction. This motivates the discussion in the following section.

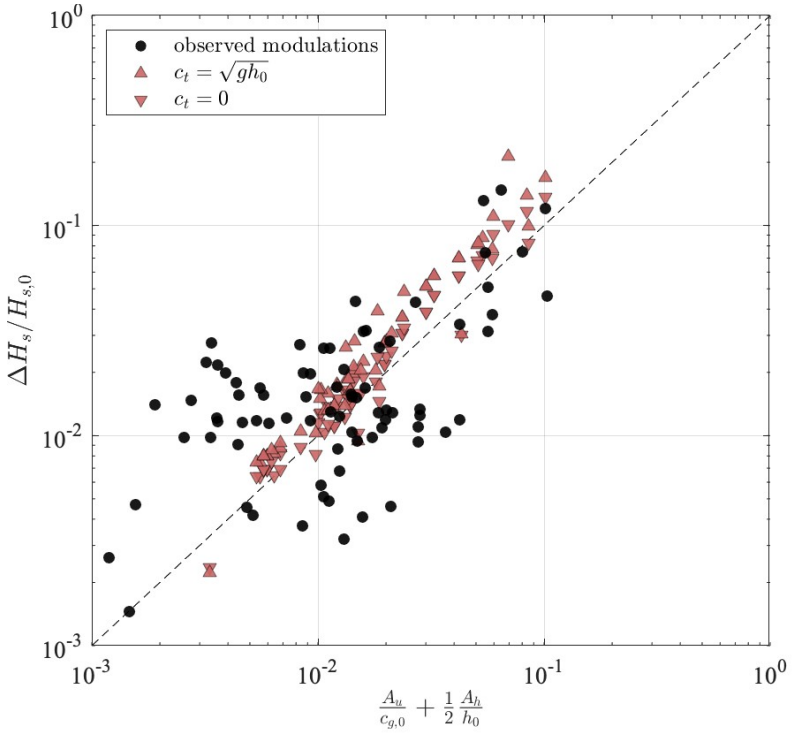

Figure 3.5. Predicted change to H_s with respect to $A_u/c_{g,0} + A_h/2h_0$ for stationary (downwards triangle) and tidal (upwards triangle) approximation for range of parameters observed in moored buoy array. Observations of semidiurnal change in H_s is shown in black.

3.5 Refraction

Ray refraction under varying mediums has has been studied for decades in its application to the interaction between surface waves and currents (Longuet-Higgins and Stewart, 1961; Kenyon, 1971; Peregrine, 1976). We use a ray approximation to model surface wave trajectories and identify cases where refraction leads to ray convergence down-wave of transverse current gradients. These effects are integral and non-local, in the sense that upstream refraction can influence local wave conditions, in contrast to the phenomena discussed above. Changes to wave direction can lead to locations of wave convergence, which, via conservation of wave energy flux, would be measured by a fixed observer as a change to the significant wave height and wave energy at the particular wave direction and frequency that becomes focused. This can lead to periodic modulations if the transverse current gradient varies periodically in time, $\frac{\partial \mathbf{U}}{\partial m} \propto \mathbf{A}\sin(\Phi t)$. To demonstrate how this can lead to periodic modulation in H_s, we solve Equations 3.9, 3.8, 3.12 iteratively using a fourth-order Runge–Kutta numerical scheme. We demonstrate this with two examples. 1) Propagation through synthetic offshore currents in deep water. 2) Propagation through modeled barotropic semi-diurnal tidal currents in the Southern California Bight region.

Conservation of wave action for steady waves implies that the flux of wave action N is non-divergent (Munk and Traylor, 1947; Weinberg and Burridge, 1974; Bretherton and Garrett, 1968; Salmon, 2002). From the divergence theorem, we can assert that the flux between any two rays is constant, such that

$$\int \mathrm{d}s\,[(\mathbf{U}+\mathbf{c_g})N]\cdot\hat{\mathbf{n}} = 0. \tag{3.31}$$

We evaluate this between the initial location of the rays, denoted by the subscript 0, and at an arbitrary point along the ray such that,

$$\frac{E_0}{\sigma_0}|\mathbf{c_{w0}}|\ell_0 = \frac{E}{\sigma}|\mathbf{c_w}|\ell, \tag{3.32}$$

where we introduce $\mathbf{c_w} = \mathbf{c_g} + \mathbf{U}$ as the propagation velocity of the wave in the direction of θ such that $\mathbf{c_w} = (c_w\cos\theta, c_w\sin\theta)$, ℓ is the distance between two rays. Thus, for an initial

condition with zero currents, energy scales with,

$$\frac{E}{E_0} = \frac{\sigma}{\sigma_0}\frac{c_{g,0}}{c_w}\frac{\ell_0}{\ell} \tag{3.33}$$

We assume that within a grid cell of area $\Delta x \Delta y$, ray density coarsely scales inversely with the square of the average length between rays,

$$\rho = \frac{n}{\Delta x \Delta y} = \frac{1}{\langle \ell \rangle^2} \tag{3.34}$$

where n is the number of rays in each grid cell. Thus we can substitute ℓ with the ray count in each grid cell n to get an expression for average energy,

$$\frac{E}{E_0} = \frac{\sigma}{\sigma_0}\frac{c_{g,0}}{c_w}\sqrt{\frac{n}{n_0}} \tag{3.35}$$

where n_0 is the ray count in a grid cell upstream unaffected by the currents. The ray terms σ,c_g, and U_θ are averaged at each grid cell, assuming that they vary slowly, and therefore remain approximately constant over the area $\Delta x \Delta y$.

Equation 3.35 highlights the separate mechanisms that can affect wave energy. If there is no change to the wave direction, and thus the distance between rays remains the same, the energy will scale with changes to the wavenumber and current. This is considered our 'local' effect. The 'non-local' effects arise from ray convergence and divergence, with energy increasing as rays get closer together. This process is considered 'non-local' because it requires global knowledge the relative ray locations to assess the amount of spreading/focusing. In these simulations, we can compare the change to the non-local and local components of Equation 3.35 over a period of time when the currents vary to assess whether or not non-local or local mechanisms dominate.

The first example is an tidally oscillating current field with a 12.42 hour period (Figure 3.6). The currents have a Gaussian spatial distribution centered at x_0, y_0 and length scale σ such that the currents decay entirely at the boundary of the domain. There is no V component to the velocity. The periodic oscillations of the U component of the current have an amplitude of A_u=0.4. The analytical form of the currents is,

$$\begin{aligned} \mathbf{U} &= (U, V) \\ &= (A_u \sin(\Phi t) f(x,y), 0) \end{aligned} \tag{3.36}$$

where Φ is the tidal frequency at 12.42 hours and the envelope $f(x,y)$ is the two-dimensional Gaussian at x_0, y_0.

$$f(x,y) = A\exp\left\{\frac{(x-x_0)^2 + (y-y_0)^2}{\sigma^2}\right\} \tag{3.37}$$

Surface waves propagate from the left side of the domain to the right at an angle of 0^o and initial period of 10 seconds. 200 rays are evenly spaced between y_{min} and y_{max}.

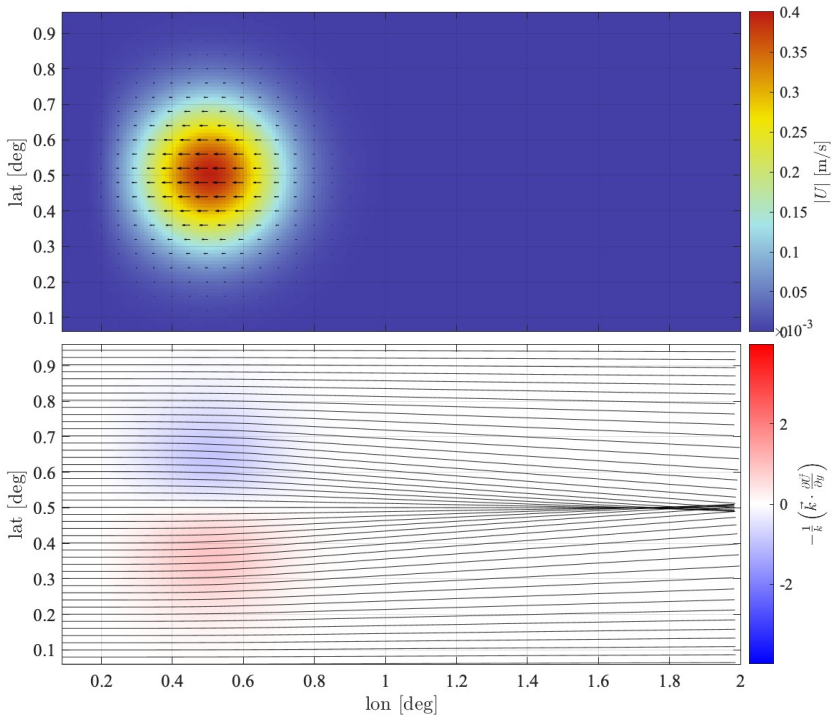

Figure 3.6. Synthetic currents (top) and ray trajectories (bottom). Current vectors are plotted in the top plot, and the transverse current gradients scaled by the wavenumber (Equation 3.11 are shown in color in the bottom plot. Rays propagate from the left of the domain at an angle of $\theta = 0$.

The results of this simulation are shown in Figure 3.7, which shows two snapshots of energy density at two different phases of the synthetic current. On average, each ray takes 8 hours to cross to the edge of the domain. This simulations demonstrate clearly how the effects of up-wave transverse current gradients can cause periodic signals at fixed observers. The two snapshots shown demonstrate instances where a positive tidal currents in the x direction create a postive/negative dipole that spreads rays apart from the center of the domain, leading to the

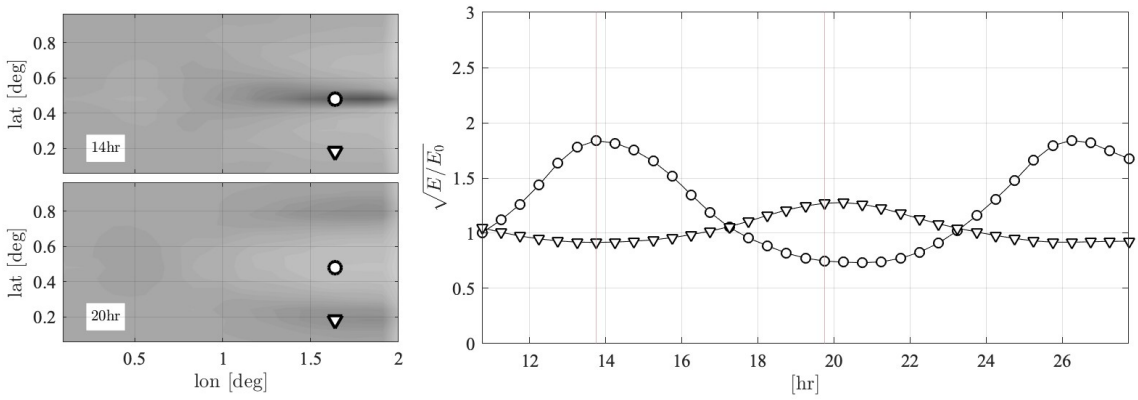

Figure 3.7. Time series of energy E/E_0 (right) at locations that represent a fixed observer denote by triangle and circle (left). Relative energy computed from Equation 3.35 is shown for two snapshots snapshot.

convergent zones near $y = 0.3$ and $y = 0.7$. Six hours later, the current has flipped sign. The negative tidal current now creates a negative/positive dipole, leading to convergence near the center of the domain. This occurs as the current gradients in the transverse direction of ray propagation causes a change in the ray direction following Equation 3.11:

$$\frac{d\theta}{dt} = -\frac{1}{k}\left(\mathbf{k}\cdot\frac{\partial \mathbf{U}}{\partial m}\right) \tag{3.38}$$

The right hand side of this equation is estimated for the synthetic currents and plotted in the bottom panel of Figure 3.6. The transverse gradients creates convergent and divergent features. For example, in Figure 3.6, the ray direction increase below $y = 0.5$ and decreases above $y = 0.5$, leading to the convergence of rays at $y = 0.5$. The time series' of ray density at two fixed observers are plotted in Figure 3.6. At each location there is a significant amount of ray convergence and divergence in a tidal period, which will lead to a change in the measured H_s. This is notable because at those locations the local currents are zero, so the fixed observers measure changes to H_s caused by non-local up-wave transverse current gradients from the current feature at $x_0 = 0.5^o$.

To demonstrate how this mechanism may exist in realistic ocean scenarios, we extend the ray tracing examples to a quasi-realistic example in the Southern California Bight. Wave propagation in the Southern California Bight is well studied (Munk and Traylor, 1947; Crosby

et al., 2016; O'Reilly et al., 1996b). Motivated by the variability in California wave climates at relatively short length scales (a few wavelengths), owed to the complex bathymetry in the region, CDIP uses a backwards spectral refraction model to estimate nearshore wave conditions. This models the refraction of ocean waves at various wavelengths and directions around the bathymetry. However, few studies in this region account for the effect of surface currents. With ray tracing, we demonstrate a case study where waves with 10 second periods propagate eastward from an offshore boundary condition at the west edge of the domain as shown in Figure 3.8. Significant bathymetric refraction and blocking occurs around the Channel Islands before the waves reach the shore.

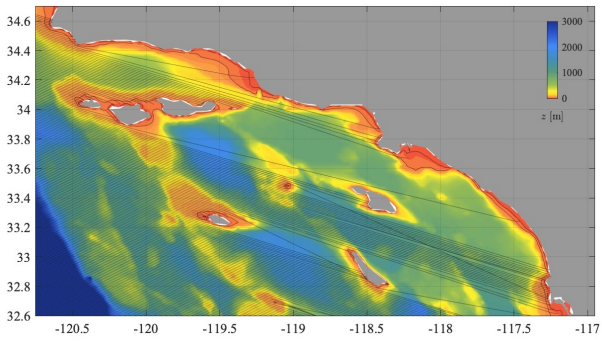

Figure 3.8. Bathymetric refraction of ray paths through the Southern California domain, propagating from the left of the domain at an angle $\theta = -20^o$. The incident period is 10 seconds. Bathymetry is shown in color, with the contour corresponding to $kh = 1,2$ for the 10 second wave shown in black.

To assess the influence of tidal currents, we run this simulation for 60 hours with tidal currents estimated using the predictions of barotropic tidal currents from the data-assimilated global barotropic tidal model TPXO 9 and Tide Model Driver 2.5 (Egbert and Erofeeva, 2002; Erofeeva et al., 2020). It is important to note that California currents are highly variable; tidal dynamics in particular are a mix of phase-locked barotropic tides and a variable internal tide field (Kim et al., 2011; Kachelein et al., 2023). Thus, this example remains only quasi-realistic, and acts as a lower bound on the potential variations to ray trajectories due to tidal currents, especially because the baroclinic tide, unresolved in the model, has much shorter length scales

and thus greater spatial gradients.

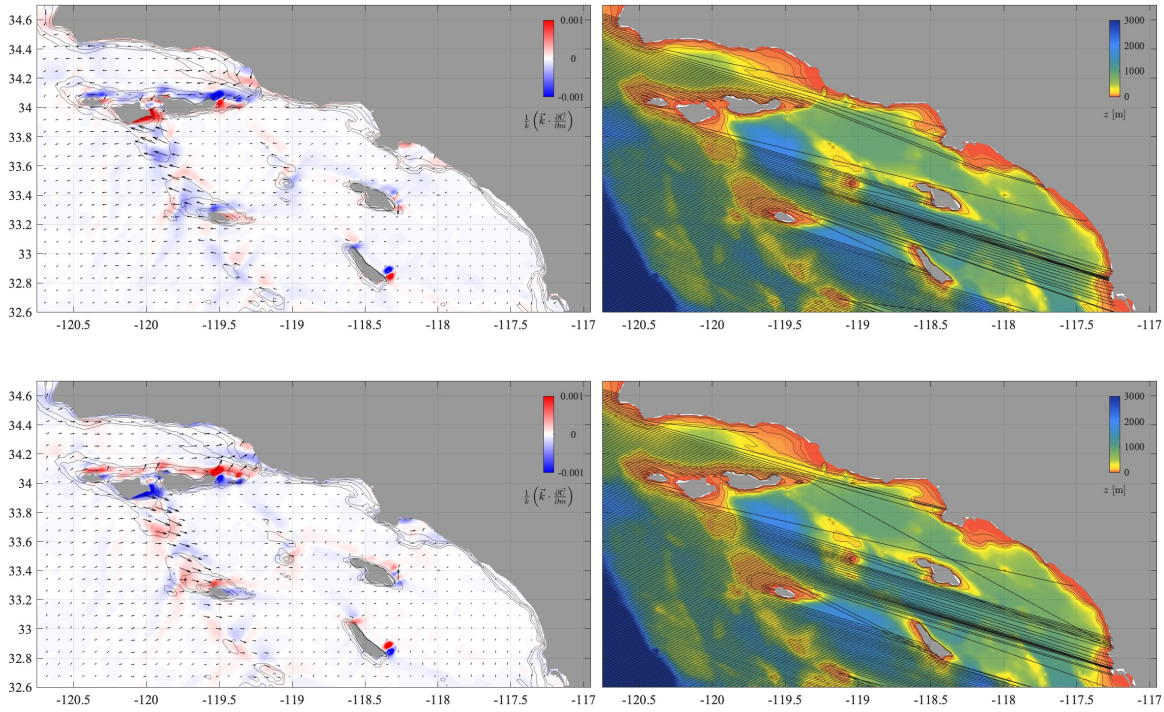

Figure 3.9. Ray paths (right) through modeled barotropic M2 tidal currents predicted (left) for incident 10 second rays from 270^o clockwise from north. Snapshots are separated by 6 hours. The right panels show surface current vectors and the transverse current gradients scaled by the wavenumber (Equation 3.11 in color. Between the two times, waves propagating through the tidal currents over the ridge south of Santa Rosa become refracted in a beam that converges either to the north or south of La Jolla. The ridge creates the dipole pattern (centered at -119.75^oW, 33.6^oN) similar to the synthetic example in Figure 3.6. This pattern repeats every 12.42 hours.

We highlight two snapshots over this simulation that are separated by six hours to represent adverse tidal current conditions. These conditions are visible in Figure 3.9 as well as the estimated change in direction. The ray trajectories for these two snapshots are shown in Figure 3.9. The largest differences occur in the trajectories of the waves that propagate towards San Diego, near -117.24° W, 32.8° N. Between the two times, waves propagating through the tidal currents over the ridge south of Santa Rosa become refracted in a beam that converges either to the north or south of La Jolla. The ridge creates the dipole pattern (centered at $-119.75°W$, $33.6°N$) similar to the synthetic example in Figure 3.6. This pattern repeats every 12.42 hours.

In summary, we look at synthetic and realistic examples of tidal or inertial currents

creating non-local periodic wave modulations. Both examples present circumstances where a fixed observer will measure a periodic change to H_s that is decoupled from any local current modulations. The significance of this change in energy will depend on the gradients of the currents and characteristics of the incident waves.

3.6 Discussion and Conclusions

We have highlighted several mechanisms that give way to periodic modulations in H_s. Both winds and currents can give rise to modulations in H_s. Tides can cause periodic modulations in H_s through tidal currents and changes in water depth that modulate the wavelength and frequency; this effect is intensified in shallow water both in the stationary and tidal approximations and sensitive to the peak period of the incident wave spectra. The key parameters that affect the amplitude of H_s variations, which include the strength of the current, the amplitude of water depth variations, the period of the waves, and the total water depth, can be reduced to a non-dimensional tidal scaling term. When compared to observations, this mechanism explains some of the semi-diurnal modulations, but not all.

Periodic modulations in H_s can also be caused by currents non-local to the observer. Current gradients transverse to the incident wave direction can cause refraction of wave directions, which can turn waves towards and away from each other, leading to regions of energy convergence and divergence far from the current gradient. If these gradients vary periodically, this can lead to periodic modulations in H_s. This is also demonstrated in a quasi-realistic example in the Southern California Bight, where strong current gradients over a ridge south of Santa Rosa create convergence hundreds of kilometers away off the coast of San Diego.

Further work needs to be done comparing these two mechanisms to figure out when which one is more important to understand the mechanisms at play in complex realistic ocean environments. Non-local refractive effects are sensitive to incident wave direction and highly variable spatially, which may lead to increased intermittence in periodic modulations caused

by this mechanism. In contrast, local wave-current interactions will be persistent as long as the current modulates periodically (the strength may change with incident wave direction and period), so may be both easier to observe and quantify statistically.

3.7 Appendix

3.7.1 Derivation of wave-tide interaction on κ in two dimensions

There are two ways refractive effects can appear with the tidal approximation. 1) if the waves are propagating at some angle oblique to the tidal wave propagation, 2) if there is some transverse structure in the tidal wave $f(y)$. For first case, we re-derive the governing equation for Equation 3.10 as a function of a tidal phase χ for the environment defined in Section 3.4. Recall that the currents $\mathbf{U}(x,y,t)$ and bathymetry $h(x,y,t)$ is described as,

$$\begin{aligned}\mathbf{U} &= (U,V)\\ &= (U(x,y,t),0)\\ &= (u(\chi),0)\end{aligned} \tag{3.39}$$

and similarly,

$$h = h_0 + z(\chi) \tag{3.40}$$

Note our rotations for our tide (fixed to (x,y)) vs wave coordinate ((s,m) where s is aligned to θ) frame:

$$\begin{aligned}(s,m) &= (x\cos\theta - y\sin\theta, x\sin\theta + y\cos\theta)\\ (x,y) &= (s\cos\theta + m\sin\theta, -s\sin\theta + m\cos\theta)\end{aligned} \tag{3.41}$$

The change of variables between (x,y,t) and (s,m,t) to χ transforms the derivatives as,

$$\begin{cases} \frac{\partial}{\partial x} = \frac{\partial}{\partial \chi}\frac{\partial \chi}{\partial x} = K\frac{\partial}{\partial \chi} \\ \frac{\partial}{\partial y} = \frac{\partial}{\partial \chi}\frac{\partial \chi}{\partial y} = 0 \\ \frac{\partial}{\partial t} = \frac{\partial}{\partial \chi}\frac{\partial \chi}{\partial t} = -\Phi\frac{\partial}{\partial \chi} \\ \frac{\partial}{\partial s} = \frac{\partial}{\partial \chi}\frac{\partial \chi}{\partial x}\frac{\partial x}{\partial s} + \frac{\partial}{\partial \chi}\frac{\partial \chi}{\partial y}\frac{\partial y}{\partial m} = K\cos\theta\frac{\partial}{\partial \chi} \\ \frac{\partial}{\partial m} = \frac{\partial}{\partial \chi}\frac{\partial \chi}{\partial x}\frac{\partial x}{\partial m} + \frac{\partial}{\partial \chi}\frac{\partial \chi}{\partial y}\frac{\partial y}{\partial m} = K\sin\theta\frac{\partial}{\partial \chi} \end{cases} \tag{3.42}$$

Such that the derivatives of the current and depth terms with respect to the wave coordinates (s,m) become,

$$\begin{cases} \frac{\partial \mathbf{U}}{\partial s} = \frac{\partial U}{\partial \chi}\frac{\partial \chi}{\partial x}\frac{\partial x}{\partial s} + \frac{\partial U}{\partial \chi}\frac{\partial \chi}{\partial y}\frac{\partial y}{\partial s} = K\cos\theta\frac{\partial u}{\partial \chi} \\ \frac{\partial \mathbf{U}}{\partial m} = \frac{\partial U}{\partial \chi}\frac{\partial \chi}{\partial x}\frac{\partial x}{\partial m} + \frac{\partial U}{\partial \chi}\frac{\partial \chi}{\partial y}\frac{\partial y}{\partial m} = K\sin\theta\frac{\partial u}{\partial \chi} \end{cases} \tag{3.43}$$

$$\begin{cases} \frac{\partial h}{\partial s} = \frac{\partial h}{\partial \chi}\frac{\partial \chi}{\partial x}\frac{\partial x}{\partial s} + \frac{\partial h}{\partial \chi}\frac{\partial \chi}{\partial y}\frac{\partial y}{\partial s} = K\cos\theta\frac{\partial z}{\partial \chi} \\ \frac{\partial h}{\partial m} = \frac{\partial h}{\partial \chi}\frac{\partial \chi}{\partial x}\frac{\partial x}{\partial m} + \frac{\partial h}{\partial \chi}\frac{\partial \chi}{\partial y}\frac{\partial y}{\partial m} = K\sin\theta\frac{\partial z}{\partial \chi} \end{cases} \tag{3.44}$$

Thus, Equation 3.10 (below) can be transposed as follows.

$$\frac{\partial \kappa}{\partial t} + (\mathbf{U} + \mathbf{c_g}) \cdot \frac{\partial \kappa}{\partial \mathbf{x}} = -\frac{\partial \sigma}{\partial h}\frac{\partial h}{\partial s} - \mathbf{k} \cdot \frac{\partial \mathbf{U}}{\partial s} \tag{3.45}$$

This is expanded explicitly to highlight how any terms related to V disappear and the group velocity and wavenumber vectors projected into the (x,y) coordinate system is $\mathbf{c_g} = (c_g\cos\theta, c_g\sin\theta)$ and $\mathbf{k} = (k,\ell) = (\kappa\cos\theta, \kappa\sin\theta)$,

$$\frac{\partial \kappa}{\partial t} + (U + c_g\cos\theta)\frac{\partial \kappa}{\partial x} + (c_g\sin\theta)\frac{\partial \kappa}{\partial y} = -\frac{\partial \sigma}{\partial h}\frac{\partial h}{\partial s} - k\cos\theta\frac{\partial U}{\partial s} \tag{3.46}$$

The derivatives with respect to s, t, x, and y are substituted for χ,

$$-\Phi\frac{\partial \kappa}{\partial \chi} + K(U + c_g\cos\theta)\frac{\partial \kappa}{\partial \chi} = -\frac{\partial \sigma}{\partial h}\frac{\partial z}{\partial \chi}K\cos\theta - k\cos\theta\frac{\partial u}{\partial \chi}K\cos\theta \tag{3.47}$$

Rearranging and defining the tidal phase speed as $c_t = \frac{\Phi}{K}$ to get the following equation for changes to κ as a function of the tidal phase χ.

$$\frac{\partial \kappa}{\partial \chi} = \frac{\cos\theta}{c_t - (U + c_g\cos\theta)}\left(\frac{\partial \sigma}{\partial h}\frac{\partial z}{\partial \chi} + k\cos\theta\frac{\partial u}{\partial \chi}\right) \tag{3.48}$$

Chapter 3, in part, is currently being prepared for submission for publication of the material, and is co-authored by Sophia Merrifield and Nicholas Pizzo. The dissertation author was the primary investigator and author of this material.

Chapter 4

Wave-tide interaction for a strongly modulated wave field

4.1 Introduction

Understanding the tidal influence on surface waves is important for maritime safety and navigation, coastal management and adaptation strategies, sediment transport, air-sea fluxes, accurate wave predictions for surf and hazard forecasts, and interpretation of measurements of the ocean surface. Some of the earliest theoretical work on wave-current interaction was motivated by the influence of tides; Bristol Channel pilots saw the roughest seas at the end of the flood tide (Unna, 1942) and the interaction of waves and tidal currents off the coast of Cornwall was considered in an early study by Barber (1949). The tidal influence on coastal wave climates has been reported in numerous studies. For example, in shallow continental shelves, wave height modulations of up to 20-50% have been attributed to tidal currents (Tolman, 1990; Wang and Sheng, 2018; Lewis et al., 2019).

When waves interact with currents, their amplitudes and phase may be modulated, which can lead to strong steepness modulations (Rascle and Ardhuin, 2013) and in some cases enhanced wave breaking (Romero et al., 2017; Vrećica et al., 2022). Although the study of wave-current interaction is well-developed (Longuet-Higgins and Stewart, 1960; Phillips, 1966; Bretherton et al., 1968; Peregrine, 1976; Wolf and Prandle, 1999; Cavaleri et al., 2007), it is only recently that multiple varieties of observations and models are being integrated and compared (Bôas et al.,

2019). There is evidence of surface waves interacting with currents at a broad range of spatial and temporal scales from the submesoscale (Phillips, 1984; Baschek, 2005; Romero et al., 2017, 2020; Vrećica et al., 2022) to large scale circulation (Holthuijsen and Tolman, 1991; Ardhuin et al., 2017; Barnes and Rautenbach, 2020). A recent study has shown wave modulation by currents account for more than 75% of the spatial variability of wave heights at scales of 100km or shorter in wave models; a significant portion of the variability of significant wave height is due to refraction over current gradients (Ardhuin et al., 2017). Additionally, many open question still remain about the two-way coupling between waves and currents (Bühler and Jacobson, 2001; Bühler and McIntyre, 2005; Villas Bôas and Pizzo, 2021). Wave models require high resolution current fields to fully resolve wave height gradients due to currents (Marechal and Ardhuin, 2021). Without currents, models may not accurately predict spectral peaks, swell arrival times, spatial gradients, and energy of waves.

The interaction of waves and currents typically is examined in the framework of conservation of wave action (Longuet-Higgins and Stewart, 1960; Bretherton et al., 1968) and geometrical optics (e.g. Peregrine, 1976). Wave action, or the wave energy divided by its intrinsic frequency, is the conserved quantity in this system as the waves and currents may freely exchange momentum and energy. Geometrical optics constrains kinematic properties of the wave field, such as the Doppler-shift of the wave frequency due to currents and the resulting implications on wave refraction. A canonical textbook example considers a uniform wave field on a steady but spatially non-uniform opposing current, which leads to wave steepening on opposing currents (Phillips, 1966; Mei, 1992).

Tidal environments, however, are neither steady nor homogeneous in space or time. Tides propagate as shallow water waves around ocean basins, generating associated currents and changes in water level that we see at the shore. The relatively higher frequency surface gravity waves propagate in this inhomogenous and unsteady medium, requiring more complex numerical wave models (Tolman, 1991; Booij et al., 1999). The unsteadiness of the tides leads to modulations to the wave field that contradict our intuition based on waves interacting with steady

currents. In particular, several studies have presented observations of wave heights *increasing* on following tidal currents (Gemmrich and Garrett, 2012; Wang and Sheng, 2018), contrasting the behavior seen for steady currents. Observations of the relative phase between the tidal currents and minima and maxima of the wave energy (i.e., the significant wave height) have been hypothesized to be due to refraction, wave dissipation (Davidson et al., 2008), relative wind (Ardhuin et al., 2012), or water depth effects. Here we seek a simple understanding for how changes in currents and water depths due to tides impact wave frequencies and amplitudes of an incoming spectrum of waves.

In this study, we present observations of tidally-driven wave-current interaction. Wave measurements at a moored buoy at Fernandina Beach, FL show strong semi-diurnal variability, modifying significant wave heights and peak periods up to 25% over a tidal cycle. The period of modulation (12.42 hours) suggests influence from currents and water depth variations associated with the semidiurnal tide. In particular, these observations also show that waves increase in steepness on following currents. We demonstrate how the observed modulations can be described in a theoretical framework where we model the tide as a linear shallow water surface gravity wave so the wave-tide interaction may be written as a long wave - short wave interaction (Longuet-Higgins and Stewart, 1962). In Section 2 we describe the observations from the Coastal Data Information Program (CDIP) Fernandina Beach station, in Section 3 we describe the two approaches used to explain the observed phenomena. Next, in Section 4 we compare the models to the observations and finally in Section 5 and 6 we summarize the results and implications.

4.2 Data

The Coastal Data Information Program (CDIP) at the Scripps Institution of Oceanography operates a network of moored Datawell Waverider directional wave buoys to monitor wave conditions in coastal regions of the Atlantic and Pacific Ocean. CDIP's operational buoy network has been used to assist coastal management and hazards mitigation, support maritime operations,

and inform numerous scientific programs (e.g. Hanson et al., 2009; O'Reilly et al., 1996a; Merrifield et al., 2021). Accelerometers measure the vertical and horizontal acceleration of the buoy at 2.56Hz. Statistical wave parameters, wave energy spectra, and the first four directional moments are computed from a 30-minute average of 200 second long overlapping spectra (50% overlap, Hanning window) of the raw displacements. This provides spectral resolution from 0.04-1Hz. The half-hourly wave data is transmitted from the buoys via Iridium satellite and is publicly available at cdip.ucsd.edu. Directional spectra are estimated via the maximum entropy method (MEM) (Kuik et al., 1988).

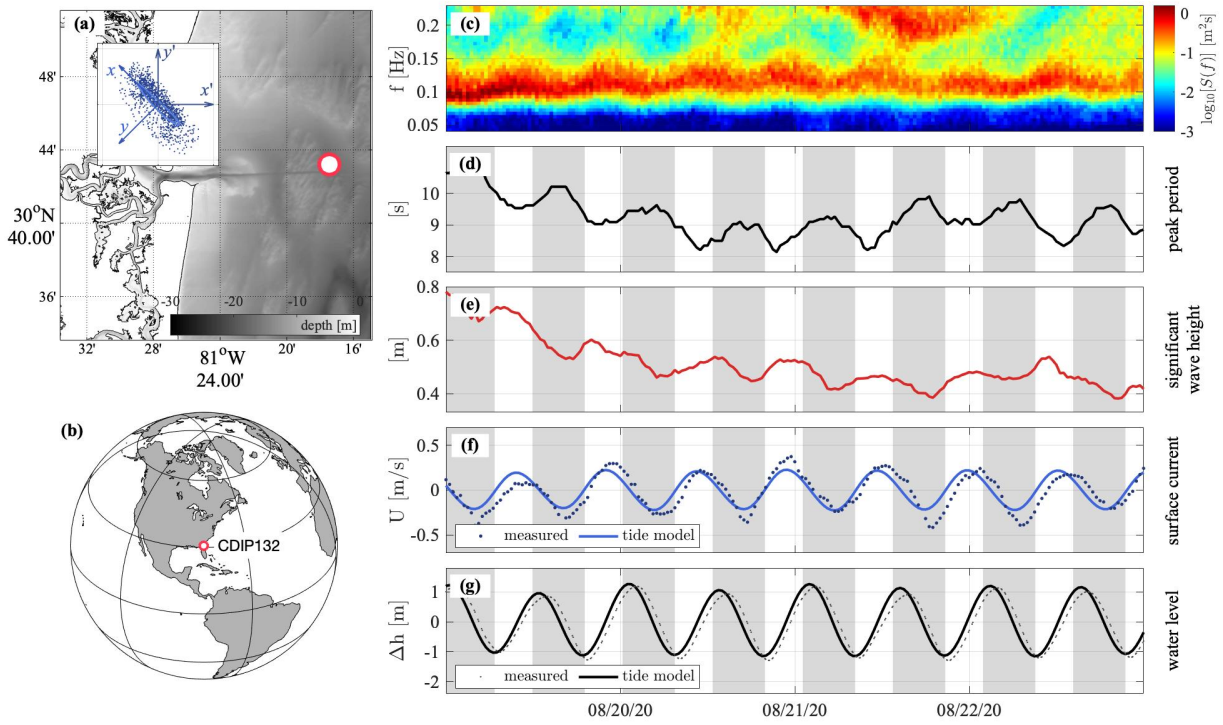

Figure 4.1. Location (a,b) and measurements from the Coastal Data Information Program (CDIP) Datawell Waverider directional wave buoy, CDIP132, used to develop and corroborate the model. A ten day sample of wave measurements including spectra (c), peak period (d), significant wave height (e), surface currents projected onto the peak wave direction (f), and change in water depth from a tidal model and measured at a nearby NOAA tide gauge (g) are shown. The tidal current ellipse is shown inlaid in (a) with the earth coordinates axes (x', y') and current coordinates axes (x, y) labeled. Gray boxes are shaded every 6.2 hours to highlight the change in wave parameters in terms of the phase of the tide.

This study examines wave observations from the CDIP buoy station 132 (CDIP132),

located offshore of Fernandina Beach in 16m water depth, shown in Figure 4.1. In September of 2020, CDIP132 was redeployed with a Datawell Waverider 4 (DWR4) (Datawell B.V., 2021) equipped with an acoustic current meter to provide direct observations of surface currents. In the hull of DWR4, three acoustic transducers with 2MHz acoustic frequency measure the current velocity between 0.5m and 1.75m from the surface. CDIP132 surface currents throughout the first year of deployment (2020-08-01 to 2021-08-01) are on average 0.23 m/s . Surface currents are tidally dominated (see harmonic analysis in Table 4.1 for dominant tidal constituents), in agreement with the climatology observed in a 2006-07 USACE study (McArthur and Parsons, 2009).

The wave climate off the east coast of Florida is dominated by seasonal local swells from nor'easters and hurricanes and trade winds. At CDIP132 from 2020-08-01 to 2021-08-01, the dominant wave direction is from the east (105 degrees) with 8.8 second average peak periods and 0.93 m average significant wave heights, but wave heights have been measured up to 3.3 m during extreme events. Onshore SE diurnal winds that peak in the afternoon with average maximum wind speeds up to 6 m/s are not coherent with wave parameters. Figure 4.1 shows an overview of observations from CDIP132, collected over 4 days in August of 2020. Clear semi-diurnal signals are apparent in the spectral and bulk parameters (Figure 4.1c-4.1e). Spectral analysis of one year of concurrent bulk wave and current and water level data was performed by taking the fast Fourier transform of the demeaned and detrended time series over 60-day overlapping segments. Spectra of surface currents (Figure 4.2f) and water levels (Figure 4.2g) show strong peaks at the principal lunar constituent M2, consistent with the dominant constituents of the observed currents and wave variations, shown in Table 4.1. Frequency spectral analysis on the swell significant wave height $H_{s,swell}$ (Figure 4.2c), defined as the significant wave height $H_s = 4\sqrt{E}$ (where E is the surface elevation variance) in the frequency range of 0.05 Hz to 0.18 Hz, shows that the primary period of oscillation is 12.42 hours, the M2 semidiurnal period, suggesting that the wave variations are due to a tidally driven process. The swell peak period $T_{p,swell}$ and swell directional spread σ_{swell} also have primary dominant peaks at the M2 tidal frequency (not

shown). Tidal variations in significant wave height, peak period, and directional spread have dominant periods at the M2 tidal frequency (Table 4.1). Nearly 90% of the tidal variability in the significant wave height can be attributed to the M2 tide. Because of the well-documented tidal currents, fixed wave direction, and strong observed modulations, this location was well suited for a case study of wave-tide interaction.

Tidal currents and water levels are measured at the nearby NOAA Tides and Currents Station 8720030 in the Fernandina Beach port on the Amelia River, available at tidesandcurrents.noaa.gov. Barotropic tidal currents and water levels are predicted at the buoy location using the data-assimilated global tidal model TPXO 9 and Tide Model Driver 2.5 (Egbert and Erofeeva, 2002; Erofeeva et al., 2020). Dominant constituents given by the tide model for the buoy location and corresponding percent variance of the observed currents and wave variations explained by each constituent are shown in Table 4.1. At CDIP132, the M2 tidal component of the observed surface currents shows strong agreement with the tide model (Figure 4.2a). In the continental shelf region of the mid-Atlantic Bight, the tides and modulations to the waves are dominated by the M2 tidal component, shown in Figure 4.2, which allows us to approximate the tide with a single tidal frequency. Nearly 70% of the variance in the observed surface currents is tidal, and the majority of that is attributed to the M2 constituent (Table 4.1). Additionally, currents flow predominantly in the north-northwest and south-southeast direction, as shown in Figure 4.1a. The current ellipse is oriented along 135^o, or 45^o to the shore, with a semi-major axis of 0.28 m/s and a semi-minor axis of 0.04 m/s. The aspect ratio of the ellipse implies that we may approximate the tide as unidirectional.

Observations of waves, surface currents, and water levels contextualize the modulations in the wave spectra. We observe significant wave height and peak frequency increasing (decreasing) on the following (opposing) current. Modulations occur near the swell peak of the spectra. Variations observed in the bulk parameters range from 10-30% (Table 4.2).

Directional spectra are estimated using MEM from the first four spectral moments recorded by the wave buoy. Figure 4.3 shows an example of directional spectra observed during a

Table 4.1. First five dominant tidal constituents for Fernandina Beach (30^{o}42'33.1"N, 81^{o}17'31.2"W) and corresponding period in hours and amplitude in meters from the global tidal model TPXO 9 and Tide Model Driver 2.5 (Egbert and Erofeeva, 2002; Erofeeva et al., 2020). For each constituent, the percent variance was calculated over two years via a least squares fit for each of the observed variables. This includes observed surface currents u_{obs} and v_{obs}, change in swell significant wave height $\Delta H_{s,swell}$, swell peak period $\Delta T_{p,swell}$, and swell directional spread $\Delta\sigma_{swell}$. A 2-day high-pass filter was applied to each observed variable. The total percent variance is calculated from the fit to all five dominant tidal constituents.

Tidal constituent	**M_2**	**N_2**	**S_2**	**K_1**	**O_1**	**Total**
Period [hr]	*12.42*	*12.66*	*12.00*	*23.93*	*25.82*	–
Amplitude [m]	*0.85*	*0.19*	*0.14*	*0.11*	*0.07*	–
Observed variable	Percent variance (modeled / observed) [%]					
u_{obs} [m/s]	63.07	3.17	2.48	0.78	0.26	69.88
v_{obs} [m/s]	56.09	3.36	2.08	0.89	0.39	62.96
$\Delta H_{s,swell}$ [%]	13.00	0.80	0.32	0.21	0.15	14.50
$\Delta T_{p,swell}$ [%]	6.26	0.44	0.30	0.18	0.18	7.38
$\Delta\sigma_{swell}$ [%]	4.52	0.54	0.39	0.53	0.17	6.17

Table 4.2. Change in swell significant wave height $\Delta H_{s,swell}$, change in swell peak period $\Delta T_{p,swell}$, and change in swell directional spread $\Delta\sigma_{swell}$ at the Fernandina Beach station CDIP132 from 2020-08-01 to 2021-08-01. Shown are the median and the 95th percentile of the percent change in the wave parameters.

	Median	95th percentile
$\Delta H_{s,swell}$	12%	25%
$\Delta T_{p,swell}$	11%	28%
$\Delta\sigma_{swell}$	9%	22%

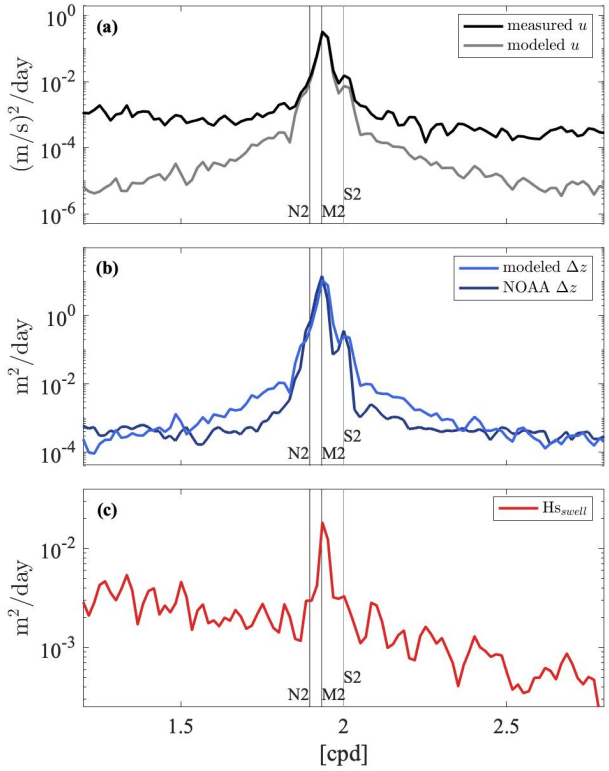

Figure 4.2. Spectral analysis of (a) observed and modeled surface currents, (b) observed and modeled water levels, and (c) observed swell significant wave height, $H_{s,swell}$. Vertical lines highlight dominant tidal constituents defined in Table 4.1. Note the high energy in the semi-diurnal bands, particularly at the M2 frequency.

peak following current and then 6 hours later at the subsequent peak opposing current. Consistent with the variations in the bulk parameters, we observe that the peak of the spectra is at a higher frequency in the following current, and the spectra has higher energy overall. In addition, a slight focusing is observed. This is manifested in a shift of the peak period towards the direction of the following current. We also observe an overall narrowing or focusing of the spectra, corresponding to a shift in the direction spreading of around 7^o.

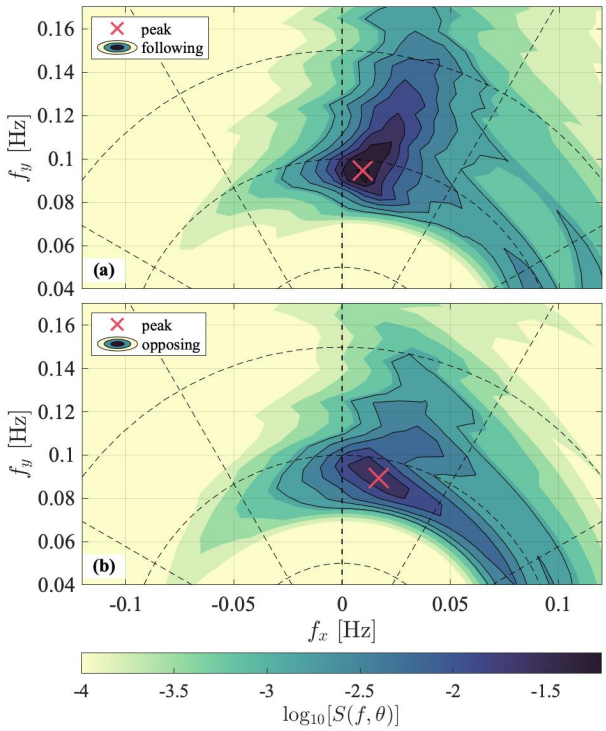

Figure 4.3. Estimated directional spectra observed during (a) following currents ($U = 0.32$m/s) and (b) opposing currents ($U = -0.25$m/s) on 2020-08-18 21:30 and 2020-08-19 03:30 respectively. Spectra are re-oriented so that 0° points in the direction of the current ellipse (along x-axis in Figure 4.1a). In this example, the wave spectra was rotated to be aligned with the current ellipse along 135°. The red X marks the peak of the spectra. The spectrum in following currents is more energetic, narrower, and shifted to higher frequencies than the spectrum in opposing currents.

4.3 Simplified Theories for Wave-Tide Interaction

Solutions for the change in wavenumber and frequency are found for two theories that treat the tide as a propagating shallow water wave. The tidal wave generates the change in mean water depth and currents experienced by the surface gravity waves. The unsteadiness of the tide leads to results that may differ significantly from those formulated based on the condition that the

currents, or changes in water depth, only vary in either space or time. Supplementing traditional wave modeling (e.g. Tolman, 1990), we draw on the field of internal wave and surface wave interaction (e.g. Gargettt and Hughes, 1972; Lenain and Pizzo, 2021) and long-wave short-wave interaction (e.g. Longuet-Higgins and Stewart, 1960), to develop simplified models of wave-tide interaction.

The next two sections describe these methods. The first theory uses solutions to geometrical optics and wave action conservation with modulations driven by tidally varying currents and depth changes. The second theory, which is analytically and numerically simpler, is based on long wave - short wave interactions in a reference frame moving with the tide. Both cases consider irrotational inviscid water waves in finite depth on a spatially and temporally evolving current and depth. The current and depth changes are related to each other, as they are taken to be tidally driven and here we approximate the tide as a monochromatic shallow water wave. Additionally, we assume that the incoming waves have constant action over the duration of consideration. That is, although the tides vary in time, we assume that the wave action is statistically steady. The goal is to model the evolution of the wave spectrum given an initial spectral distribution, tidal current, and tidal amplitude.

4.3.1 Governing equations

Consider unidirectional linear surface gravity waves with vector wavenumber, $\mathbf{k}$, absolute frequency, ω, energy E, and direction θ relative to the x-axis. These parameters are assumed to be slowly varying in space and time relative to the scales of the waves themselves. Following Mei et al. (2005), for a periodic plane wave solution for the surface height $\eta = ae^{i\Theta} + c.c.$ (where $c.c.$ means complex conjugate) with amplitude a and the phase $\Theta(x,y,t) = \mathbf{k}\cdot\mathbf{x} - \omega t$, while the absolute frequency ω and wavenumber $\mathbf{k} = (k,\ell)$ for $\mathbf{x} = (x,y)$ are related to the phase by

$$\omega = -\frac{\partial\Theta}{\partial t}, \qquad \mathbf{k} = \nabla\Theta. \tag{4.1}$$

When combined, these equations yield the conservation of wave crests equation

$$\frac{\partial \mathbf{k}}{\partial t} + \nabla \omega = \mathbf{0}. \tag{4.2}$$

The group velocity of wave energy is defined as

$$\mathbf{c_g} = \frac{\partial \sigma}{\partial \mathbf{k}}. \tag{4.3}$$

For waves on a weak current, the dispersion relation is modified to account for the change in background current velocity $\mathbf{U} = (U,V)$. The propagation velocity of the wave energy is then

$$\mathbf{c_w} = \mathbf{c_g} + \mathbf{U}, \tag{4.4}$$

and the absolute (or total) frequency as observed by a stationary observer is,

$$\omega = \sigma + \mathbf{k} \cdot \mathbf{U}, \tag{4.5}$$

where σ, the relative (or intrinsic) frequency, follows the dispersion relation for surface gravity waves,

$$\sigma = \sqrt{g|\mathbf{k}|\tanh(|\mathbf{k}|h)}, \tag{4.6}$$

where g is the acceleration due to gravity, h is the water depth, and $|\mathbf{k}| = \sqrt{k^2 + \ell^2}$. The relative frequency σ is defined explicitly as a function of $\mathbf{k}(\mathbf{x},t)$ and $h(\mathbf{x},t)$, so we can substitute equation (4.5) into equation (4.2) and expand each derivative to get the full equations for the change in wave parameters following Bretherton et al. (1968),

$$\frac{\partial \mathbf{k}}{\partial t} + (\mathbf{c_g} + \mathbf{U}) \cdot \nabla \mathbf{k} = -\frac{\partial \sigma}{\partial h}\frac{\partial h}{\partial \mathbf{x}} - \mathbf{k} \cdot \frac{\partial \mathbf{U}}{\partial \mathbf{x}}, \tag{4.7}$$

$$\frac{\partial \omega}{\partial t} + (\mathbf{c_g} + \mathbf{U}) \cdot \nabla \omega = \frac{\partial \sigma}{\partial h}\frac{\partial h}{\partial t} + \mathbf{k} \cdot \frac{\partial \mathbf{U}}{\partial t}. \tag{4.8}$$

Wave energy propagation is governed by the conservation of wave action. Wave action is defined as the ratio between wave energy and the intrinsic frequency, $A = {}^{E}/_{\sigma}$. The wave action conservation equation is,

$$\frac{\partial A}{\partial t} + \nabla \cdot [(\mathbf{U} + \mathbf{c_g})A] = S. \tag{4.9}$$

Here S represents the source terms in the wave action balance, typically equal to $S = S_{in} + S_{diss} + S_{nl}$, the sum of the wind input, dissipation, and nonlinear wave-wave interactions, respectively. We set $S = 0$ to examine only the dynamics of wave propagation under currents and depth variations independent of any forcing.

4.3.2 One-dimensional numerical solutions for waves propagating on a tide: Tolman's model

To gain intuition for our system, we start by examining one-dimensional solutions to the equations of geometrical optics and conservation of wave action under the assumption of a one dimensional tide. In one dimension, with x aligned with k, equations (4.7) and (4.8) and (4.9) reduce to

$$\frac{\partial k}{\partial t} + (c_g + U)\frac{\partial k}{\partial x} = -\frac{\partial \sigma}{\partial h}\frac{\partial h}{\partial x} - k\frac{\partial U}{\partial x}, \tag{4.10}$$

$$\frac{\partial \omega}{\partial t} + (c_g + U)\frac{\partial \omega}{\partial x} = \frac{\partial \sigma}{\partial h}\frac{\partial h}{\partial t} + k\frac{\partial U}{\partial t}, \tag{4.11}$$

and

$$\frac{\partial A}{\partial t} + \frac{\partial}{\partial x}[(U + c_g)A] = 0, \tag{4.12}$$

where, c_g and U are the group velocity and current in the $\hat{x}$ direction. The group velocity is given by

$$\begin{aligned} c_g &= \frac{\partial \sigma}{\partial k} \\ &= \frac{\partial}{\partial k}\left\{\sqrt{gk\tanh(kh)}\right\}, \end{aligned} \tag{4.13}$$

and the propagation velocity of the wave energy along the axis x is given by

$$c_w = c_g + U. \tag{4.14}$$

Following the approach of Tolman (1990) and Vincent (1979), we seek periodic solutions for the advection of surface gravity waves by the tidal wave. We consider the tide to be a one dimensional monochromatic progressive shallow water wave of constant frequency, Φ, and wavenumber, K, with corresponding currents, U, and depth variations, h, as a function of the tidal phase, χ, defined as,

$$U(x,t) = A_u \sin(\chi(x,t)), \tag{4.15}$$

$$h(x,t) = \bar{h} + A_h \sin(\chi(x,t) + \varphi), \tag{4.16}$$

and

$$\chi(x,t) = Kx - \Phi t. \tag{4.17}$$

where A_u and A_h are the current and depth amplitude, respectively, and $\bar{h}$ is the mean water depth. The term φ allows for a phase shift between water level variation and currents as observed in many coastal tidal environments with mixed progressive and standing wave tides (Pugh, 1987). The tidal propagation velocity is defined as the phase speed for shallow water waves,

$$\begin{aligned} c_t &= \Phi/K \\ &= \sqrt{g\bar{h}}. \end{aligned} \tag{4.18}$$

The shallow water approximation holds for the tide so long as the tidal wavelength is much greater than the water depth, as is the case at Fernandina Beach in 16 m average water depth. We rewrite the governing equations (4.10)-(4.12) as functions of χ. The coordinates (x,t) must be changed to the tidal phase $\chi = Kx - \Phi t$, where the derivatives become,

$$\begin{cases} \frac{\partial}{\partial x} = \frac{\partial}{\partial \chi}\frac{\partial \chi}{\partial x} = K\frac{\partial}{\partial \chi} \\ \frac{\partial}{\partial t} = \frac{\partial}{\partial \chi}\frac{\partial \chi}{\partial t} = -\Phi\frac{\partial}{\partial \chi} \end{cases} \tag{4.19}$$

We can now rewrite equations (4.10)-(4.12) in terms of χ to arrive at final expressions for the rate of change of wave parameters.

$$\frac{\partial k}{\partial \chi} = \frac{1}{c_t - (c_g + U)}\left(\frac{\partial \sigma}{\partial h}A_h\cos(\chi + \varphi) + kA_u\cos\chi\right), \tag{4.20}$$

$$\frac{\partial \omega}{\partial \chi} = \frac{c_t}{c_t - (c_g + U)}\left(\frac{\partial \sigma}{\partial h}A_h\cos(\chi + \varphi) + kA_u\cos\chi\right), \tag{4.21}$$

and

$$\frac{\partial A}{\partial \chi} = A\frac{1}{c_t - (c_g + U)}\left(\frac{\partial c_g}{\partial \chi} + A_u\cos\chi\right). \tag{4.22}$$

From these equations, we identify the generalized behavior of the modulations in wavenumber, frequency, and wave action. The common term in the denominators, which we will call c_*,

$$c_* = c_t - (c_g + U), \tag{4.23}$$

determines the magnitude and sign of the modulations set by equations (4.20)-(4.22). In particular, when $|c_*|$ is small, the modulations to the surface waves are large. This occurs when the tidal wave and the surface waves have similar speeds, $c_t \approx c_g + U = |c_w|$. For the progressive shallow water tide, modulations in surface wave parameters are most amplified at low frequencies because their propagation velocities c_w approach the tide's shallow water phase (and group) speed $\sqrt{g\bar{h}}$. The c_* term in the denominator of each equation can also change sign if c_t is either larger or smaller than the wave action propagation velocity.

To compare the relative contributions due to depth variations or currents, we can compare the coefficients in front of each phase-dependent term associated with changes in depth or changes in currents in equations (4.20) and (4.21). When the non-dimensional term

$$\gamma = \frac{kA_u}{\frac{\partial\sigma}{\partial h}A_h} \tag{4.24}$$

is greater than (less than) one, currents (depth changes) dominate the modulation in wavenumber. The phase difference due to φ in equations (4.20) and (4.21) can also alter the relative influence of depths and currents as well as the total magnitude of modulations. For example, current and depth variations are out of phase ($\varphi = \pi$), then when $\gamma \approx 1$, the depth modulations and current modulations can effectively cancel out. When $\varphi = 0$ the two contributions to wave modulations will constructively add. However, other values of φ can lead to peaks in wavenumber or wave energy modulation that are not in phase with either the depth variations or the currents. Typical values for c_* and γ will be evaluated at Fernandina Beach in §3d.

In summary, we identify a phase space that governs the variations in wave parameters due to tides. This space includes not just the magnitude of currents and depth variations, A_u and A_h, but also wavenumber k, energy E, mean depth $\bar{h}$, phase φ, and tide phase speed c_t. Full solutions can be found to this system of equations by solving them numerically using an explicit Runge-Kutta method with variable timesteps given initial conditions $k_0 = k(\chi = 0)$,

$\omega_0 = \omega(\chi = 0)$, $A_0 = A(\chi = 0)$ (Shampine and Reichelt, 1997). This approach allows us to derive simplified governing equations for surface wave modulation due to tidally driven currents and depth variations, further quantifying the importance of different forcing parameters, including current magnitude, water depth, and tide phase speed. However this approach is limited by its computational complexity, which, while relatively simple, becomes apparent when generalizing the system to two dimensions. The next section presents an alternative approach that allows us to model two dimensional effects with less computational complexity. We adopt a convenient perspective often applied to understanding the interaction between internal waves and surface waves by working in a reference frame moving with the tide (Longuet-Higgins and Stewart, 1960). This method is described in the next section.

4.3.3 Long wave - short wave solutions for tides and surface gravity waves

In the fixed reference frame of the buoy, absolute frequency is not conserved as currents U and water depth h vary with time. However, following Phillips (1966), we can work in a frame of reference moving with the tidal wave at phase speed, c_t. As U and h only vary with the phase of the tide, the absolute frequency in this reference frame has no explicit dependence on time,

$$\frac{d\omega_t}{dt} = 0. \tag{4.25}$$

The absolute frequency in this frame of reference, ω_t, is modified from equation (4.5) for the fixed frame and is given by,

$$\omega_t = \sigma + \mathbf{k} \cdot (\mathbf{U} - \mathbf{c_t}). \tag{4.26}$$

The conservation of absolute frequency equation (4.25) then implies

$$\sigma_0 + |\mathbf{k}_0|(-c_t)\cos\theta_0 = \sigma + |\mathbf{k}|(U - c_t)\cos\theta. \tag{4.27}$$

Subscript 0 denotes an initial condition where tidal currents are negligible. The angle, θ, is the angle between the waves and the x-axis, which we choose to be aligned with the current. The refraction of the waves is determined by the fact that the wavenumber is the gradient of a scalar

(i.e. the phase), so that its curl is zero. This result, known as Snell's Law, implies that in the absence of transverse currents, we have,

$$|\mathbf{k}_0|\sin\theta_0 = |\mathbf{k}|\sin\theta. \tag{4.28}$$

With some manipulation, Snell's Law tells us that if the magnitude of the wavenumber varies, so too will variations in θ. We can illustrate this from equation (4.28) with a few assumptions: ignoring the variation in the horizontal component we make a small perturbation expansion for variations in k and θ, where $k \approx k_0 + \Delta k$ and $\theta \approx \theta_0 + \Delta\theta$. Then by small angle and first order approximation, equation (4.28) becomes,

$$\frac{\Delta k}{k_0} \approx -\frac{\Delta\theta}{\tan\theta_0}. \tag{4.29}$$

In the one-dimensional approximation, we assume that the waves and currents are aligned and there is no refraction. We are able to find solutions for the modulated wavenumber $|\mathbf{k}|$ to equation (4.27) through the relation

$$\begin{gathered}\sqrt{g|\mathbf{k_0}|\tanh(|\mathbf{k_0}|h_0)} + |\mathbf{k}_0|(-c_t) = \\ \sqrt{g|\mathbf{k}|\tanh(|\mathbf{k}|h)} + |\mathbf{k}|(U - c_t).\end{gathered} \tag{4.30}$$

In two dimensions, we find θ by substituting $|\mathbf{k}| = |\mathbf{k}_0|\sin\theta_0/\sin\theta$ into equation (4.27) and solving the following equation for θ

$$\begin{aligned}&\sigma_0 - |\mathbf{k}_0|c_t\cos\theta_0 = \\ &\sqrt{g|\mathbf{k}_0|\frac{\sin\theta_0}{\sin\theta}\tanh(|\mathbf{k}_0|\frac{\sin\theta_0}{\sin\theta}h)} + |\mathbf{k}_0|\frac{\sin\theta_0}{\sin\theta}(U - c_t)\cos\theta.\end{aligned} \tag{4.31}$$

The wavenumber is then found by solving equation (4.27) for $|\mathbf{k}|$. Solutions for both θ and $|\mathbf{k}|$ are found numerically using the Newton-Raphson method.

The wave action equation for a single wavenumber given in equation (4.9) is extended to include a full spectrum of surface waves with a variable wavenumber $k = k_x$ in the direction of the current x (e.g. Figure 4.1a), and constant in the off-axis y, $\ell = \ell_0 = k_y$ following Hughes (1978) for $Adkd\ell_0$ over a narrow band of k, ℓ space

$$\frac{\partial A}{\partial t} + (c_g + U)\frac{\partial A}{\partial x} = 0. \tag{4.32}$$

In the tide reference frame where wave parameters are time-independent, we find that

$$\begin{aligned} A(k,\ell_0)dkd\ell_0 &= A_0(k_0,\ell_0)dkd\ell_0 \\ &= A_0(k_0,\ell_0)\frac{\partial k}{\partial k_0}dk_0 d\ell_0. \end{aligned} \tag{4.33}$$

The behavior of the Jacobian $\frac{\partial k}{\partial k_0}$ is found following Hughes (1978). We differentiate equation (4.2) with respect to k_0 in the reference frame moving with the tidal wave, using the definition for ω as ω_t in equation (4.26), to find the Jacobian,

$$(c_g + U - c_t)\frac{\partial k}{\partial k_0} = c_{g,0} - c_t. \tag{4.34}$$

In summary, the shifted energy is calculated as

$$E(k,\ell_0)dkd\ell_0 = E_0(k_0,\ell_0)\frac{\sigma}{\sigma_0}\frac{c_{g,0} - c_t}{(c_g + U - c_t)}dk_0 d\ell_0. \tag{4.35}$$

The above expression relates an initial vector-wavenumber spectrum to the final vector-wavenumber spectrum modulated by a tidal wave with phase speed, c_t, and induced current, U. The final step is to relate the vector-wavenumber spectrum $E(k,\ell)$ to the observed absolute frequency spectrum $E(\omega,\theta)$ measured by a moored, stationary wave buoy. This step is detailed in the appendix §7.

In summary, this approach allows us to reduce this problem to a series of simple algebraic equations that are easily solved and replicate the numerical model for solutions to the coupled ODEs in the previous section. See also the related discussion in Gargettt and Hughes (1972) and Lenain and Pizzo (2021). The next section uses the two approaches to model the theoretical response of a wave spectra to tidal currents and depths for the Fernandina Beach environment.

4.3.4 Model predictions

The two simplified models lead to equivalent results and each has advantages in modelling and interpreting wave-tide interaction. To gain intuition about the predictions of the models,

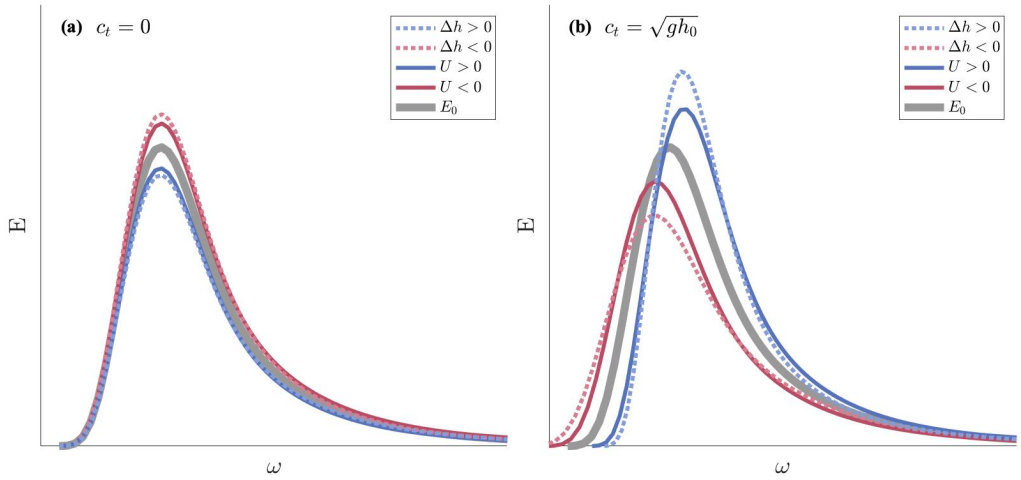

Figure 4.4. Given an incident wave spectra (grey), we show the resulting shift due to a change in current (solid) or a change in water level (dashed) as predicted by the model given by equations (4.31), (4.27), and (4.35). We show the shift corresponding to a following and opposing current (blue / red solid lines respectively) and an increase or decrease in water level (blue / red dashed lines respectively) for the two separate circumstances where the tidal propagation velocity parameter c_t is equal to the shallow water wave phase speed (b) or zero (a). Note the change in sign of the spectral deviations from (a) to (b) in response to the same forcing.

we force them with conditions that replicate the Fernandina Beach environment ($A_u = 0.25$m/s, $A_h = 1$m, $\bar{h} = 16$m). We illustrate in Figure 4.4 the response of a one-dimensional Jonswap wave spectrum under the influence of currents and depth variations induced by tides as found by solutions to equations (4.31), (4.27), and (4.35) in one dimension, i.e. $\theta = 0$. The simulated spectrum has a peak at 10 seconds. We show two cases, one where the phase speed of the tide is zero, $c_t = 0$, (Figure 4.4a) and one where the phase speed of the tide is the shallow water phase speed, $c_t = \sqrt{g\bar{h}}$ (Figure 4.4b). In the first case, we see that a following (opposing) current shifts the spectra to lower (higher) energy. However, when $c_t = \sqrt{g\bar{h}}$, the model predicts variations more similar to those observed at Fernandina Beach: now, a following current will shift the spectra to higher energy and frequency, and vice versa for the opposing case. The relationship with a change in water depth is similar, where an increase in water level shifts the spectra lower when $c_t = 0$ and higher when $c_t = \sqrt{g\bar{h}}$.

Tolman's model highlights the importance of the sign of $c_t - (c_g + A_u)$ in modulating the

maxima and minima of the significant wave height and peak period. The terms in equations (4.23) and (4.24) from the model analysis in §3b allow us to identify the size and sign of variations expected at Fernandina Beach and interpret the modeled spectra in Figure 4.4. As before, we use variables that replicate conditions at Fernandina Beach ($A_u = 0.25$m/s, $A_h = 1$m, $\bar{h} = 16$ m). The group velocity c_g is found by estimating the wavenumber for a 10 second peak period using the dispersion relation in equation (4.6). Finally, we assume the tide acts as a progressive shallow water wave, $c_t = \sqrt{g\bar{h}}$. Under these conditions, $c_* = 3.27$. The positive value of c_* indicates that the wavenumber variations will be in phase with the oscillation of currents or depth, i.e. that as currents increase and become positive, the change in wavenumber will increase. Similarly, as currents decrease and become negative, the change in wavenumber will decrease. In comparison, when $c_t = 0$ for these exact same conditions, c_* is negative and is much larger in magnitude, with $c_* = -9.25$. The change in the sign of c_* is consistent with the difference between the simulated spectra in Figure 4.4, where the response between the two conditions are of opposite sign. The smaller magnitude of c_* when $c_t = \sqrt{gh_0}$ also indicates that the modulation in the surface waves will be large, which is clear in 4.4 as the shift in the wave spectra is nearly three times larger than for the case when $c_t = 0$. From this analysis we also conclude that currents and water depth modulations are approximately balanced at the 10 second peak, with current changes slightly dominating the modulation, as $\gamma \approx 1.17$. In comparison, for slightly lower frequencies at 12 seconds, depth variations dominate the modulation as $\gamma \approx 0.96$, and for slightly higher frequencies at 8 seconds, current variations dominate the modulation as $\gamma = 1.76$.

The model developed using a long-wave short-wave approximation described in §3c allows us to gain intuition behind the individual physical mechanisms at play with minimal computational complexity. The case of internal wave - surface wave interaction, when the phase speed of the internal wave is typically less than that of the surface waves, can be represented by the $c_t \ll 1$ example. With tides, the phase speed $c_t = \sqrt{g\bar{h}}$ is typically larger than that of the surface waves, which is why in wave-tide interactions the response of the surface waves to currents can be opposite.

The key to interpreting the change in sign of the modulations is noting the different speeds of the long wave in question. Most surface waves - including long period swell - propagate slower than the phase speed of the tide, which here we take to be a shallow water wave. In the reference frame moving with the long wave, the slower surface waves now appear to propagate backwards. In this reference frame, what was previously surface waves propagating in the same direction as the current, now the surface waves oppose the direction of the current. The frequency and steepness thus increase. Returning to the fixed frame, this shift is maintained, yet the definition of following / opposing current switches again and we observe surface waves steepening on following currents.

If the tides and waves are not aligned, the apparent tide phase speed is smaller than the shallow water phase velocity, by a factor that is the cosine of the angle between the waves and the tide, and the response of the surface waves can differ and be more complicated. This might explain why the literature contains observations with various phases between the maximum wave amplitudes and the maximum tidally induced currents (e.g. Barber, 1949; Tolman, 1988; Masson, 1996; Davidson et al., 2008; Gemmrich and Garrett, 2012; Guillou, 2017; Wang and Sheng, 2018)

The two-dimensional model that simulates directional frequency spectra implies that not only does the frequency and energy increase on the following current, there is also directional focusing towards the direction of tidal wave propagation, similar to that observed at Fernandina Beach. Conversely, an opposing current increases directional spreading for a given incident wave away from the direction of the long-wave propagation. This can impact both the directional spread and the location of the peak of the directional spectrum in the cases where the peak is off-axis of the current vector.

Simulations of modeled spectra also show the sensitivity to the value of c_t when c_t approaches c_w, as described in §3b. The methods fail when there are no solutions to equation (4.27), which occurs when the short-wave propagation velocity nears the tidal phase speed, i.e. $c_t = c_w = c_g + U$, such that waves cannot travel upstream. Classically, this is known as the

blocking frequency (Phillips, 1966; Gargettt and Hughes, 1972). In the ocean, a combination of breaking and reflection likely occur (Chawla and Kirby, 2002; Ardhuin et al., 2010, 2012), but these effects are not incorporated into this simplified model. In general, c_t becomes an important parameter to describe the sign of the wave modulations with respect to the currents. Even when c_t does not equal c_w, small variations in the value of c_t can alter the magnitude of variation in the surface waves.

4.4 Comparison to Observations

We use the methods developed in §3 to model the tidal variations observed in the wave measurements from the Fernandina Beach CDIP station. Equations (4.27) and (4.31) are solved algebraically to estimate the change in wavenumbers, and then used in equation (4.35) to find the modulated directional spectrum $E(k,\ell)$. The initial condition $E_0(k_0,\ell_0)$ is taken from the observed directional absolute frequency spectrum $E_0(\omega_0,\theta_0)$ when the current magnitude is zero to represent an "unmodulated" spectrum. The observed directional spectra are averaged over 90 minutes to reduce noise. The initial condition is converted to vector wavenumber spectra and the result from the model is converted back to absolute frequency spectra via equation (4.38). Because the Mid-Atlantic Bight and study region is dominated by semi-diurnal tides (Table 4.1), we are able to approximate the tide with a single constituent. We use periodic M2 tidal fits to the observed water depth and surface currents to force the simulation. This model can be run at any time step with any frequency resolution, so we chose to simulate the modulated spectra at same intervals of the observations to facilitate the comparison. However, higher resolutions are easily achieved with minimal added computational costs.

We present a comparison of the modeled wave spectra over one day beginning on 2020-08-20 09:00 in Figures 4.5 and 4.6. Time is expressed as a function of the tidal phase, χ, where 2π covers 12.42 hours. This subsection of the observations was chosen for this example as the incident swell was relatively constant during this time period, isolating the impact of the tidal

variations. We discuss the implications of a varying background wave field later in this section.

The model captures the variations in the wave spectra and the bulk parameters due to the tides. The omni-directional spectrum shown in Figure 4.5 is calculated from the modeled directional spectrum by integrating over all directions. The modeled energetic swell band in Figure 4.5 is shifted upward and amplified at $\pi/2$, and downward later at $3\pi/2$, similar to the observed spectrogram. The one-dimensional spectra at the minima and maxima of the current variations are shown in Figure 4.6a. Both the modeled and observed spectra shift downward in energy and frequency during the opposing current, and shift higher during the following current. The observed peak shifted from 0.119 Hz (0.409 m^2s) to 0.109 Hz (0.271 m^2s), and the modeled peaks shifted from 0.121 Hz (0.404 m^2s) to 0.107 Hz (0.294 m^2s). Potential causes for the over estimation of modulation at lower frequencies, also visible in Figure 4.5, are discussed in §5.

Model deviations from the observed spectra can also occur when non-local or wind-driven energy influences the wave spectra. We chose to model $f < 0.2$Hz in part because this band of the surface wave spectrum is most strongly modulated by the tides and also to avoid the shorter time scale variability in wind forcing as seen around 1π in Figure 4.5. Here the observed high frequency waves ($f > 0.1Hz$) become more energetic due to changing wind conditions that are not accounted for in this wave-tide numerical model that does not include source/sink terms. Likewise, a decrease in significant wave height over 2π in Figure 4.6 is unaccounted for as the presented tidal model does not account for dispersion nor decrease in energy from long-period remote swell. When we do not update the background energy after initiating the model, the model begins to decorrelate from the observations after about 4π (about 1 day), which is the approximate time scale of variations for wind events and modulations in direction and magnitude of the remotely forced swell.

Figure 4.6 shows the change in significant wave height and peak period at Fernandina Beach, and how the model predicts similar variations in bulk parameters when current and depth conditions match observations. The shaded region indicates variations due to errors up to 50% of the total current or depth variation magnitudes. From a following to opposing current, the

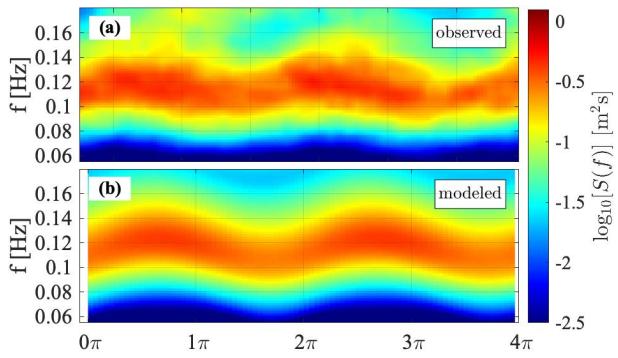

Figure 4.5. Wave spectrogram observed over one day (a) and reproduced wave spectrogram from the numerical model of the omnidirectional spectra (b) developed using observations to set the initial condition and forcing terms (currents and depth variations). The modeled spectrogram mimic the increase and decrease in frequency of the observed swell band. The model tends to overestimate the variation in lower frequencies.

model significant wave height varies from 0.52 to 0.46 m (12% decrease), and the observed significant wave height varies from 0.51 to 0.44 m (13% decrease). This model peak period varies from 8.2 to 9.3 seconds (13% increase) and the observed peak period varies from 8.4 to 9.1 seconds (9% increase). The timing of the minima and maxima of the bulk parameters shown are not coincident with the minima and maxima of the surface currents, indicating the modulations due to water level contribute to the change in bulk parameters, as estimated by γ. We still predict that the following current coincides with an increase in significant wave height and decrease in peak period, as observed in the measurements. There is a lag in the modeled peak period with respect to the observations, which can be associated with the overestimation of low frequencies or unresolved physical processes, discussed in §5. Nevertheless, the bulk scale agreement between the relatively simple model and the observations is encouraging. For this time range, the model predicts a percent change equivalent to that observed and within observed median values for the observations at CDIP132 (Table 4.2).

Directional effects are also modeled and compared to observations of directional spectra,

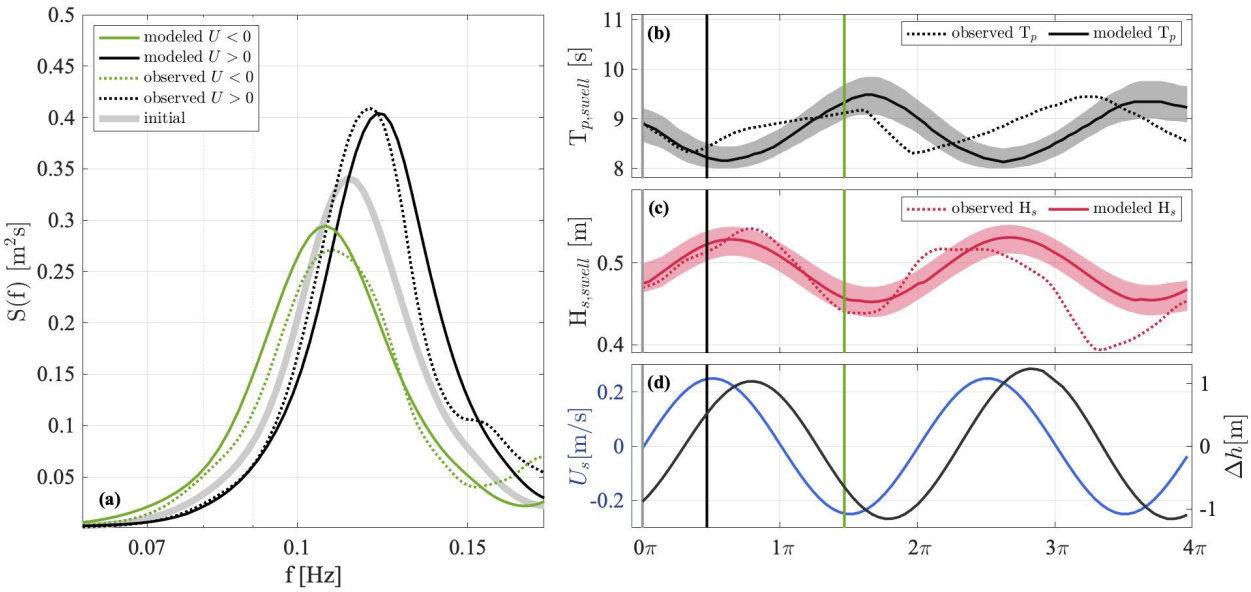

Figure 4.6. Observations are used as an initial condition to estimate the resulting shift of the directional spectrum under tidal currents and water level variations (d). The omni-directional spectrum resulting from following current (black) and opposing current (green) is shown in (a) for both the observations and the model. The initial condition for this run is shown in grey. The bulk parameters (0.05Hz$< f <$ 0.18Hz) for both the model and observations including peak frequency (b) and significant wave height (c). The shaded region corresponds to varying the magnitude of the maximum current speed and depth changes by up to 50%.

which indicate that a slight focusing and a shift in peak direction occur. Observations of shifts in the mean directional spread in the swell band of up to 10 degrees (e.g. Figure 4.3) are modeled in the directional spectrum.

Generally for the environment at Fernandina Beach, with variations in water levels up to 1 meter and tidal currents up to 0.2 m/s, the model predicts variations of significant wave height of up to 25%. This agrees with average values variations in observed significant wave height from Table 4.2, even with the simple assumption of a uniform incident wave spectrum and simple shallow-water tidal wave propagation. Overall, the model confirms that tides will induce changes in the wave field that will manifest in both lower and higher order moments.

4.5 Discussion

Further work to investigate the impact of wave-tide interaction on wave breaking and dissipation using third-generation models could be beneficial to understanding the impact of this phenomena in the broader wave and earth system. This includes addressing issues in this simplified model when the speed of long wave c_t nears the propagation velocity of surface waves c_w and blocking occurs. This is manifested as a critical point in the variables and subsequently the model breaks down. Expanding this work to other locations will help assess any variability in the surface wave modulation by tides related to the wave climatology and various tidal conditions. This work highlights the need for measurements of surface currents and directional wave spectra at other locations with different tidal environments. For example, the model is limited to only using a single tidal phase χ or constituent, which may cause issues when applying this in regions with mixed semidiurnal and diurnal tides. For regions with mixed tides, the reference frame will need to be chosen carefully for the method that relies on working in a reference frame where there are no explicit temporal variations. We have also assumed that the tide is a shallow water progressive wave, and further work should be done to characterize the variability of the phenomena under mixed standing and progressive wave tides, amplified tides, and other coastal wave complexity. This may change the formulation of c_t. Further work can incorporate observations of tidal variation in wave energy at other locations to assess variation with different tidal environments.

This work reiterates the importance of careful interpretation of the reference frame of our observations. It is clear that the reference frame of the observer plays an important role, as noted by work on interpreting wave measurements from propelled platforms like ships and wave gliders and from remote sensing via satellite and HF radar (Longuet-Higgins, 1986; Ardhuin et al., 2009; Collins et al., 2016). In order to integrate and compare multiple varieties of observations and models, especially with the advent of current-measuring satellites such as SWOT, it will be important to carefully consider the measurements.

4.6 Conclusion

In conclusion, this work presents theoretical and numerical models that help understand how tides can modulate surface waves. We present observations of significant tidal modulations in wave records from a moored buoy at Fernandina Beach, FL which shows strong modulations to the surface wave field in frequency, magnitude and direction. Following tidal currents correspond with an increase in wave height of up to 25%, contrary to the canonical textbook example where waves steepen on opposing steady homogeneous currents. We describe the observed modulations through a simplified theoretical framework that models the tide as a progressive shallow water wave, effectively treating the problem as a long wave - short wave interaction. By working in the reference frame moving with the tidal wave, we have simplified the problem from a system of partial differential equations to algebraic equations, which reduces the computational complexity significantly. The model shows that when the phase speed of long wave is faster than propagation velocity of surface waves, steepness can increase on following tidal currents. Key non-dimensional parameters are identified that characterize the size of tidal modulations in wave parameters. Finally, numerical solutions to this model reproduce the observed wave modulations due to tidal currents and changes in water depth at Fernandina Beach.

With the framework developed in this study, we characterize the size and sign of tidal modulations in wave parameters. Surface waves will be amplified by the tide when they propagate in the direction of the tidal currents and when the speed of the surface waves propagation nears the speed of the tidal wave. This will be dependent on both wave frequency, water depth, and current magnitude. When the speed of the tidal wave exceeds the speed of the surface gravity wave propagation, tidal currents following the direction of surface wave propagation can lead to an increase in surface wave height and frequency. At Fernandina Beach where the dominant wave direction is aligned with the tides, this leads to amplification of the peak of the spectrum.

This work has demonstrated the ability to understand significant tidal variations in wave spectra by treating the interaction between surface waves and the tide as a long-wave short-

wave interaction. This treatment allows us to understand how waves respond to tidally induced currents and depth variations, import for maritime safety and navigation, coastal management and adaptation strategies, and accurate nearshore wave forecasts, proposing an explanation for the common surfing phenomena known as the tidal push, where incident wave heights increase during the rising tide. This highlights the importance of careful interpretation of measurements and models for both public and scientific application. Future numerical work will explore the impact of wave breaking, relative wind, and shorter time scale variability in wave fields. This framework will also be used to constrain observed variation in surface waves due to tides and provide statistical estimates for wave variations due to tides at other nearshore environments.

Acknowledgements

The authors thank Eric Terrill, Mark Merrifield, Bia Villas Bôas, Fabrice Ardhuin, and Bill Young for numerous helpful discussions. This work benefited from close collaboration with members of the CDIP team including Jim Behrens and Corey Olfe. Lastly, we thank the two anonymous reviewers for their insightful feedback. This work is funded by the U.S. Army Corps of Engineers through Cooperative Ecosystem Studies Unit (CESU) W912HZ1920020.

Data Availability Statement

Wave data were furnished by the Coastal Data Information Program (CDIP), Integrative Oceanography Division, operated by the Scripps Institution of Oceanography, under the sponsorship of the U.S. Army Corps of Engineers and the California Department of Parks and Recreation. Water level data are from NOAA Tides and Currents. Bathymetry at Fernandina Beach is from NOAA National Centers for Environmental Information (NOAA, 2014). All data used in this paper are publicly available at https://cdip.ucsd.edu/ and https://tidesandcurrents.noaa.gov/ and https://www.ncei.noaa.gov/. Data and analysis are collected in Ho et al. (2022).

4.7 Appendix

4.7.1 Comparison to observations

We express the output in the more traditional absolute frequency spectrum $E(\omega,\theta)$ to relate to the omni-directional frequency spectrum measured by a moored, stationary wave buoy. This is calculated via the Jacobian transformation between frequency and wavenumber as,

$$\begin{aligned} E(\omega,\theta)d\theta d\omega &= E(\kappa,\theta)d\kappa d\theta \\ &= E(\kappa,\ell)\kappa d\kappa d\theta. \end{aligned} \tag{4.36}$$

This is rearranged for the final expression for the directional absolute frequency spectrum.

$$\begin{aligned} E(\omega,\theta) &= \kappa\frac{\partial\kappa}{\partial\omega}E(\kappa,\ell) \\ &= \kappa(c_g+U)^{-1}E(\kappa,\ell). \end{aligned} \tag{4.37}$$

The derivative of absolute frequency with respect to κ was rewritten using the definition in equation (4.5) via,

$$\frac{\partial\omega}{\partial\kappa} = \frac{\partial}{\partial\kappa}(\sigma+\kappa U) = c_g + U \tag{4.38}$$

Finally, the omni-directional spectrum is found by integrating over all directions for a fixed frequency, which requires interpolation.

$$E(\omega) = \int_0^{2\pi} E(\omega,\theta)d\theta \tag{4.39}$$

It is important to note that the Jacobian transformation from wavenumber space to spectra in terms of absolute frequency and direction is not well behaved as there is a singularity at the blocking point (Tolman and Booij, 1998). See also the discussion on the blocking point in §5.

Chapter 4, in full, is a reprint of the material as it appears in the Journal of Physical Oceanography. The dissertation author was the primary investigator and author of this paper. A Ho, S Merrifield, N Pizzo, Wave-Tide Interaction for a Strongly Modulated Wave Field, Journal of Physical Oceanography. https://doi.org/10.1175/JPO-D-22-0166.1

Chapter 5

Concluding Remarks

This dissertation has investigated the impact of tidal currents on short time scale variability in coastal ocean wave climates. A climatolological assessment of tidal signals in historical wave records show that inertial, diurnal, and tidal modulations to wave height are common in coastal ocean wave climates. The signals have distinct seasonal, regional, and frequency patterns that relate to the underlying mechanism for imparting momentum and energy into the wave field from the underlying currents. To understand the amplitude of the tidal signals, a simplified framework for wave-tide interaction is used to estimate particularly strong modulations at Fernandina Beach, FL. There, the unsteady and inhomogenous tidal currents may set up a resonant long wave short wave interaction between the surface waves and tidal wave, leading to amplification of wave energy on following currents. This simplified model is capable of resolving both changes in wave height, peak period, and wave spectra. This framework is then extended to contextualize the observations across the moored array of historical wave records, showing good agreement in particular regions on the East Coast of the United States. On the West Coast, there are several instances in the dataset where wave modulations are observed at tidal or inertial frequencies, but the surface currents have no corresponding signal. Simple numerical studies demonstrate alternative mechanisms for periodic variability in surface waves. In particular, the non-local and integral effects of wave refraction through transverse current gradients that vary at tidal or inertial periods can create periodic modulations in wave energy downstream where no local

current would be measured. This highlights the complexity of mechanisms that impart energy into the wave field. To fully resolve the periodic variability at some of these observations, both temporal and spatial information about ocean currents is required.

Overall, these findings can help in accurately representing nearshore surface wave variability on short time scales and subsequent impacts on coastal inundation and nearshore transport, particularly as current operational wave models neglect tides and surface currents due to the computational requirements. This work provides insight for emerging studies in remote sensing. Recent advancements in technology and new observations, including the launch of the Surface Water and Ocean Topography (SWOT) mission, present exciting new opportunities to observe the ocean surface with unprecedented resolution, but highlights ongoing observational challenges in combining and interpreting measurements from a diverse set of observations that measure ocean processes and surface waves at different temporal and spatial scales (Bôas et al., 2019).

Chapter 6

Appendix

6.1 Mechanisms for wind-driven diurnal modulations

Wind primarily imparts energy at the high frequency tail of the surface wave spectrum, thus, the impact of wind on H_s is mostly additive. In contrast, currents can have pronounced effects at wave frequencies near the peak of the spectrum in cases where unsteady currents resonate the low frequency swell or refract long period waves. In other words, the effect of winds acts additive to total H_s and currents acts multiplicative. To gain intuition for this system, we leverage a parallel system from classical mechanics. Similar to how surface waves conserve wave action (rather then energy or frequency independently), a pendulum conserves the total mechanical energy (rather than only kinetic or potential energy). Modifications to the pendulum system through either changing the total length of the pendulum or forcing the pendulum. These modifications to the pendulum system may change the natural frequency or oscillations of the pendulum, but conserve the total energy, equivalent to the effect of currents or winds on waves under the conservation of wave action. Thus, we can explore the combined wind-driven and current-driven effects by examining the response of periodically forced pendulum with periodically varying length. The pendulum is illustrated in Figure 6.1 and comprised of a mass m connected to a hinge by a string whose length $\ell(t)$ is allowed to slowly vary periodically in time. A time dependent externally imposed periodic force is $F(t)$. The angle φ is the angle between

the mass and the vertical. The governing equation is then,

$$\ddot{\varphi} + \frac{2\dot{\ell}}{\ell}\dot{\varphi} + \frac{g}{\ell}\varphi = F(t) \tag{6.1}$$

Note that when $\ell(t) = \ell_0$ and $F(t) = 0$, the solution for the pendulum is simple harmonic motion with a natural frequency at

$$\omega_0 = \sqrt{\frac{g}{\ell_0}} \tag{6.2}$$

We define $\ell(t)$ and $F(t)$ as,

$$\ell(t) = \ell_0 + A\sin(\nu t) \tag{6.3}$$

$$F(t) = B\sin(\mu t) \tag{6.4}$$

Where the frequencies ν and μ are much smaller than the natural frequency of the pendulum, $\nu \ll \omega_0$ and $\mu \ll \omega_0$. In order to demonstrate the sensitivity of the modulations related to $\ell(t)$ and $F(t)$ to the initial condition, Equation 6.1 is solved numerically for varying initial mass position φ_0,

$$\varphi(0) = \varphi_0 \tag{6.5}$$

$$\dot{\varphi}(0) = 0 \tag{6.6}$$

The results are analyzed by computing the phase averaged horizontal position of the mass $x(t)$. The results are shown in Figure 6.1. The variance at ν changes with the initial condition, where for higher initial angle positions φ_0, the stronger the signal at ν, i.e. the pendulum makes larger amplitude excursions in x at the length frequency ν. In contrast, the signal at μ is invariant to the initial condition. The signal at μ does change when adjusting the amplitude B. Analysis becomes complicated when the length of the pendulum and the external forcing oscillate at the same frequency, $\nu = \mu$. In this case, without exact knowledge of the amplitudes A and B and the solution for Equation 6.1, it is difficult to disentangle the signals in $x(t)$.

These results are representative of the surface wave analogs. Wind-driven signals in H_s, analog to the signal at the forcing frequency in $x(t)$, are invariant to the initial condition, or initial H_s. Current driven signals in H_s are instead sensitive to the initial condition, just as the

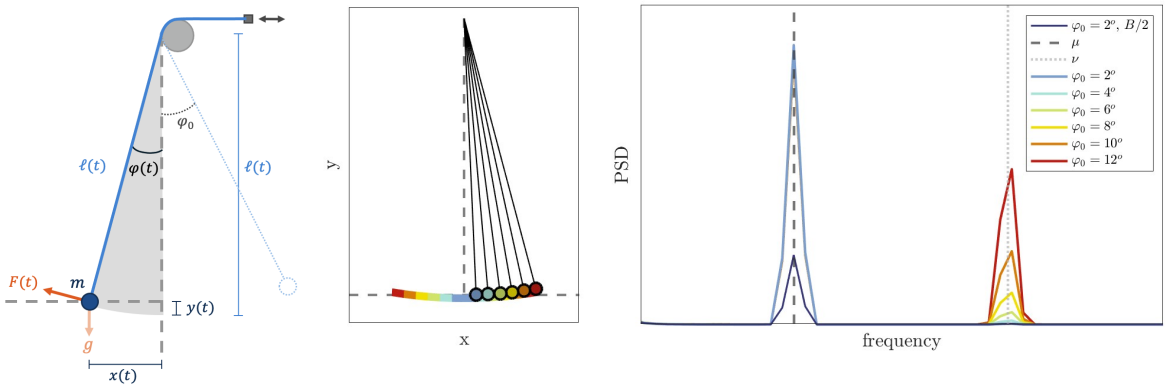

Figure 6.1. Forced pendulum with varying length (left), solved for varying initial conditions φ_0 (center). Power spectra of envelope of horizontal position $x(t)$ for each initial condition. The forcing frequency μ and length frequency ν are annotated in the dashed lines.

signal at ν related to the variable length is dependent on the initial position of the pendulum mass. Thus, though both of these phenomena can lead to distinct periodic signals in H_s $(x(t))$, the relationships to the surrounding wave climate (initial condition φ_0) are different, where the wind is additive, much like the forcing term in the pendulum, and a current is multiplicative to the background or initial condition, much like the variable length.

This then requires careful treatment of the periodic signals in the wave height records, and any inversion for the underlying mechanism will require prior knowledge. This can be roughly done with the diurnal and semi-diurnal signals in the wave height records in the moored array as comparison to wind measurements indicates that it is driven by the diurnal sea breeze. The implications of this on the subsequent Fourier analysis is discussed in the following section.

6.2 Spectral Analysis

Fourier based spectral analysis methods are used commonly to study ocean time series. These methods are best used for linear, periodic, and stationary processes. While stationary in frequency, it is clear that that the strength and persistence of the tidal and inertial signals in wave height records may be non-linear, intermittent, and a-periodic, as has been identified

in various theoretical studies. However, without knowing this with universal certainty for every type of wave-current and wind-wave modulation at every buoy, we use Fourier-based methods to 1) reduce complexity in interpretation introduced by other techniques (e.g. wavelet analysis, HHT, etc.) 2) reserve the ability to cross-compare signals at different frequencies with unknown mechanisms, and 3) to process a large amount of data quickly. Here we address considerations when applying these mechanisms on additive and multiplicative periodic signals. These considerations are important to make when dealing with wind-driven and current-driven effects on wave heights, as discussed in Section 6.1.

6.2.1 Fourier transform of multiplicative and additive signals

We briefly demonstrate how computing Fourier transformations on time series with nonlinear signals requires normalization dependent on a known relationship between the signal and the noise. For additive signals, i.e., where the measured signal x is comprised of a time-varying noise term $x_0(t)$ and a periodic signal at a particular frequency ω_0 with an amplitude A, such that

$$x(t) = x_0(t) + A\sin(\omega_0 t) \tag{6.7}$$

Fourier analysis is relatively straightforward.

$$\begin{aligned} \mathscr{F}\{x(t)\} &= X(\omega) \\ &= X_0(\omega) + \int_{-\infty}^{\infty} A\sin(\omega_0 t)e^{-i\omega t}dt \\ &= X_0(\omega) + \frac{A}{2}\left[\delta(\omega-\omega_0) + \delta(\omega+\omega_0)\right] \end{aligned} \tag{6.8}$$

Noise is removed from the observed spectrum $X(\omega)$ by subtracting the noise spectrum $X_0(\omega)$; the resulting form will have an amplitude at the signal frequency ω_0 that is linearly related to the amplitude of modulation in the time domain A. We can solve this explicitly by integrating over a small bandwidth around ω_0 , $\Delta = \omega_0 \pm \varepsilon$

$$\begin{aligned} \int_\Delta X(\omega)d\omega &= \\ &= \int_\Delta X_0(\omega)d\omega + \frac{A}{2}\int_\Delta \left[\delta(\omega-\omega_0) + \delta(\omega+\omega_0)\right]d\omega \end{aligned} \tag{6.9}$$

The first dirac deltas is integrated over $0 \pm \varepsilon$, so evaluates to 1, and the second is integrated over $2\omega_0 \pm \varepsilon$, so evaluates to 1. Thus, the amplitude A of the modulation is inferred as,

$$A = 2\left(\int_{\Delta} X(\omega)d\omega - \int_{\Delta} X_0(\omega)d\omega\right) \tag{6.10}$$

For the case where noise is multiplicative, spectral analysis requires nuance. We begin with an observed signal that's amplitude scales with the background noise.

$$x(t) = x_0(t)(1 + A\sin(\omega_0 t)) \tag{6.11}$$

This is effectively a cosine modulation to our background spectrum $X(\omega)$, which results in a frequency shift of $X(\omega)$ as multiplication in the time domain on the last term becomes convolution in the frequency domain.

$$X(\omega) = X_0(\omega) + \frac{A}{2}X_0(\omega - \omega_0) + \frac{A}{2}X_0(\omega + \omega_0) \tag{6.12}$$

From this we get an expression for A.

$$A = \frac{2\left(X(\omega_0) - X_0(\omega_0)\right)}{\left(X_0(0) + X_0(2\omega_0)\right)} \tag{6.13}$$

We assume that the value of X_0 at twice the driving frequency will be small compared to $X_0(0)$ the mean of the noise term, which we can call $\overline{x_0}$. Thus, our final expression for the driving amplitude of the periodic signal is,

$$A = \frac{2(X(\omega_0) - X_0(\omega_0))}{\overline{x_0}} \tag{6.14}$$

This expression now allows a linear relationship in the frequency domain between the amplitude of a multiplicative signal in the time domain. We demonstrate this treatment with a synthetic time series in Figure 6.2. We've prescribed a background noise $x_0(t)$ with a red spectral slope and two periodic signals, one centered at f_1 that follows the additive form and one centered at f_2 that follows a multiplicative form.

This difference is important to note because the modulations to H_s from currents has a multiplicative form:

$$H_s(t) = H_{s,0}(t) + \alpha H_{s,0}(t) \tag{6.15}$$

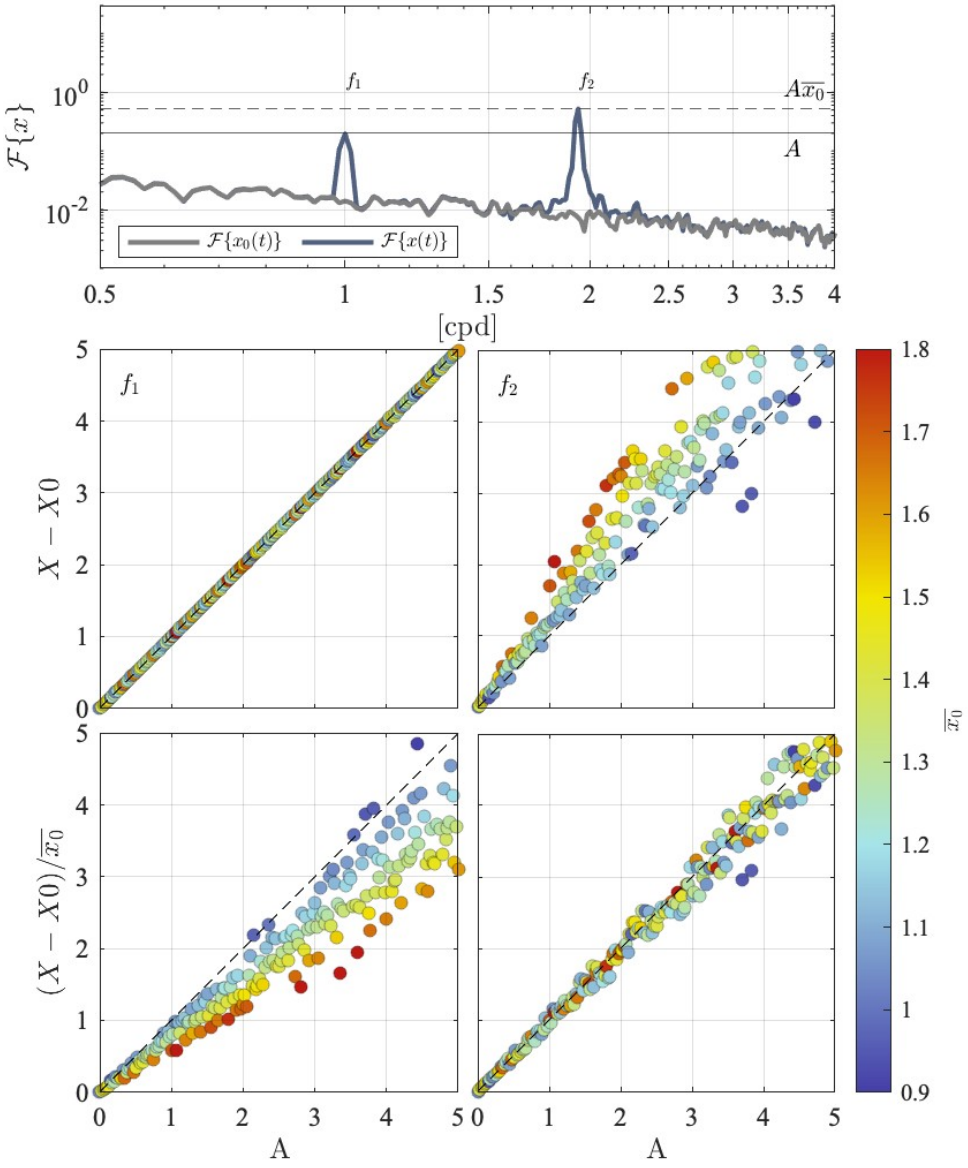

Figure 6.2. Inferring modulating amplitude for additive signal (top) and multiplicative signals (bottom) applied to additive signals at f_1 (left) and multiplicative signals f_2 (right) generated from artificial time series with red noise. Colored by average value of x_0.

In Equation 6.15, α is proportional to U/c_g in deep water but for our cases we define it generally as some periodic function at the tidal frequency who's amplitude A_α depends on the tidal current, wave frequency, water level variations, and local water depth. This modulating amplitude is

calculated from the H_s spectrum X^{H_s} as,

$$A_\alpha = \frac{2\left(X^{H_s}(f_{M2}) - X_0^{H_s}(f_{M2})\right)}{\overline{H_{s,0}}} \tag{6.16}$$

The amplitude of the scaling A_α will take different forms for the mechanisms of wave-current interaction discussed in Chapter 3. Because of the different dynamics at play, we move forward by keeping it defined generally: for additive relationships (e.g. wind-driven at S1)

$$A_{S1} = 2\left(X^{H_s}(f_{S1}) - X_0^{H_s}(f_{S1})\right) \tag{6.17}$$

and for multiplicative relationships (e.g. current-driven at M2)

$$A_{M2} = \frac{2\left(X^{H_s}(f_{M2}) - X_0^{H_s}(f_{M2})\right)}{\overline{H_{s,0}}} \tag{6.18}$$

The difference between additive (e.g. wind) versus multiplicative (e.g. currents) phenomena is evident in the spectral analysis of synthetic data with two signals in Figure 6.2. The linear scaling (Figure 6.2(a-b)) of the computed spectra at f_2 has a clear bias at high mean f_2 values, which is corrected in the multiplicative scaling in Figure 6.2(d). However, the multiplicative scaling introduces a bias in the computed values at f_1 in Figure 6.2(c): for the same A magnitude, observations with low mean f_2 have disproportionately high estimates. This will be important when dealing with signals at the semi-diurnal (M2) and diurnal frequencies (S1), as the contribution from diurnal winds at S1 has a different functional relationship to H_s than the current.

6.3 Co-located Observations

This dissertation combines observations of winds, waves, and currents from several discrete publicly available data sources identified in Chapter 2.2 over the 23 year period between 2000-2023. Here we summarize the observational coverage of each of these sources. The coverage is visualized in Figure 6.3.

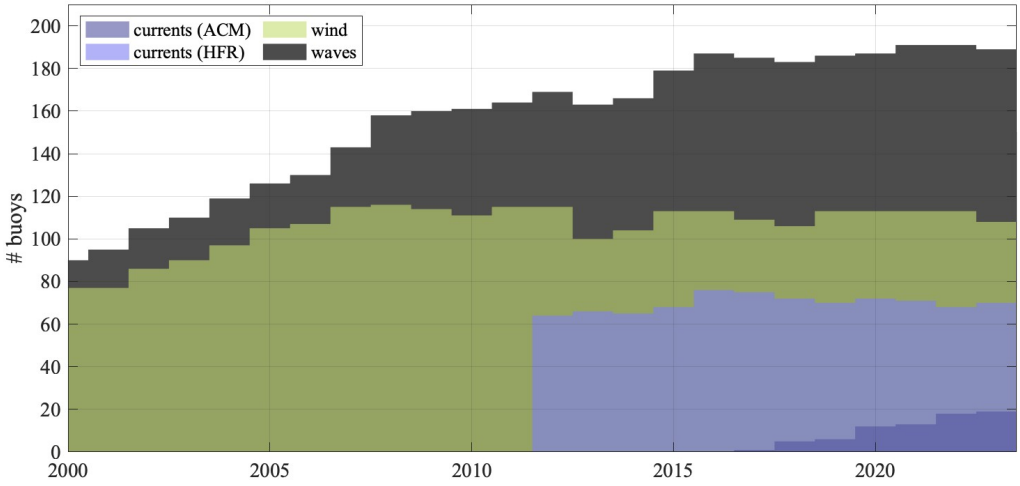

Figure 6.3. For each year, the number of stations with observations of waves (black), wind (green), remotely-sensed HFR currents (purple) and in-situ ACM currents (dark purple). Co-located HFR observations begins in 2012 when the network begins disseminating data in NetCDF file format, although HFR observations date back to 2008.

Out of the 249 buoys analyzed in this study, 109 have co-located surface current measurements. The buoys with co-located surface current measurements are all located within 50 km from shore due to the limitations of shore-based HF radar and recent deployments of platforms with in-situ current sensors. This dataset and analysis in this dissertation highlights the need for more observations of ocean surface currents and ocean waves in both open ocean and coastal wave climates, which is being answered by present and future satellite missions and ongoing coastal monitoring efforts.

Bibliography

Airy, G. B., 1845: *Tides and waves*. B. Fellowes.

Alford, M. H., 2003: Redistribution of energy available for ocean mixing by long-range propagation of internal waves. *Nature*, **423 (6936)**, 159–162.

Alford, M. H., and M. Whitmont, 2007: Seasonal and spatial variability of near-inertial kinetic energy from historical moored velocity records. *Journal of Physical Oceanography*, **37 (8)**, 2022 – 2037, doi: https://doi.org/10.1175/JPO3106.1.

Ardhuin, F., S. T. Gille, M. Dimitris, C. B. Rocha, N. Rascle, B. Chapron, J. Gula, and J. Molemaker, 2017: Small-scale open ocean currents have large effects on wind wave heights. *Journal of Geophysical Research: Oceans*, **122**, 1–22, doi: 10.1002/2016JC012413.

Ardhuin, F., L. Marié, N. Rascle, P. Forget, and A. Roland, 2009: Observation and estimation of lagrangian, stokes, and eulerian currents induced by wind and waves at the sea surface. *Journal of Physical Oceanography*, **39 (11)**, 2820–2838, doi: 10.1175/2009JPO4169.1.

Ardhuin, F., and Coauthors, 2010: Semiempirical dissipation source functions for ocean waves. Part I: Definition, calibration, and validation. *Journal of Physical Oceanography*, **40 (9)**, 1917–1941, doi: 10.1175/2010JPO4324.1.

Ardhuin, F., and Coauthors, 2012: Numerical wave modeling in conditions with strong currents: Dissipation, refraction, and relative wind. *Journal of Physical Oceanography*, **42 (12)**, 2101–2120, doi: 10.1175/JPO-D-11-0220.1.

Barber, N. F., 1949: The behaviour of waves on tidal streams. *Proceedings of the Royal Society of London. Series A. Mathematical and Physical Sciences*, **198 (1052)**, 81–93, doi: 10.1098/rspa.1949.0088.

Barnes, M. A., and C. Rautenbach, 2020: Toward Operational Wave-Current Interactions Over the Agulhas Current System. *Journal of Geophysical Research: Oceans*, **125 (7)**, 1–21, doi: 10.1029/2020JC016321.

Baschek, B., 2005: Wave-current interaction in tidal fronts. *Aha Hulikoa Hawaiian Winter*

Workshop 2005, 131–138, URL http://www.soest.hawaii.edu/PubServices/2005pdfs/Baschek.pdf.

Battisti, D. S., and A. J. Clarke, 1982: A simple method for estimating barotropic tidal currents on continental margins with specific application to the m 2 tide off the atlantic and pacific coasts of the united states. *Journal of Physical Oceanography*, **12 (1)**, 8–16.

Battjes, J. A., T. J. Zitman, and L. H. Holthuusen, 1987: A Reanalysis of the Spectra Observed in JONSWAP. 1288–1295 pp., doi: 10.1175/1520-0485(1987)017⟨1288:AROTSO⟩2.0.CO;2.

Behrens, J., and Coauthors, 2024: Coastal data information program: advances in measuring and modeling wave activity, climate, and extremes. *Coastal Engineering Journal*, 1–14.

Belcher, S. E., and Coauthors, 2012: A global perspective on langmuir turbulence in the ocean surface boundary layer. *Geophysical Research Letters*, **39 (18)**.

Bôas, A. B., and Coauthors, 2019: Integrated observations of global surface winds, currents, and waves: Requirements and challenges for the next decade. *Frontiers in Marine Science*, **6**, 1–34, doi: 10.3389/fmars.2019.00425.

Booij, N., R. C. Ris, and L. H. Holthuijsen, 1999: A third-generation wave model for coastal regions: 1. model description and validation. *Journal of Geophysical Research: Oceans*, **104 (C4)**, 7649–7666, doi: https://doi.org/10.1029/98JC02622, https://agupubs.onlinelibrary.wiley.com/doi/pdf/10.1029/98JC02622.

Bretherton, F. P., and C. J. R. Garrett, 1968: Wavetrains in inhomogeneous moving media. *Proceedings of the Royal Society of London. Series A. Mathematical and Physical Sciences*, **302 (1471)**, 529–554, doi: 10.1098/rspa.1968.0034.

Bretherton, F. P., C. J. R. Garrett, and M. J. Lighthill, 1968: Wavetrains in inhomogeneous moving media. *Proceedings of the Royal Society of London. Series A. Mathematical and Physical Sciences*, **302 (1471)**, 529–554, doi: 10.1098/rspa.1968.0034.

Bühler, O., and T. E. Jacobson, 2001: Wave-driven currents and vortex dynamics on barred beaches. *Journal of Fluid Mechanics*, **449**, 313–339.

Bühler, O., and M. E. McIntyre, 2005: Wave capture and wave–vortex duality. *Journal of Fluid Mechanics*, **534**, 67–95.

Bôas, A. B. V., B. D. Cornuelle, M. R. Mazloff, S. T. Gille, and F. Ardhuin, 2020: Wave–current interactions at meso- and submesoscales: Insights from idealized numerical simulations. *Journal of Physical Oceanography*, **50 (12)**, 3483 – 3500, doi: https://doi.org/10.1175/JPO-D-20-0151.1.

Carter, G. S., and Coauthors, 2008: Energetics of m2 barotropic-to-baroclinic tidal conversion at the hawaiian islands. *Journal of Physical Oceanography*, **38 (10)**, 2205–2223.

Cavaleri, L., B. Fox-Kemper, and M. Hemer, 2012: Wind waves in the coupled climate system. *Bulletin of the American Meteorological Society*, **93 (11)**, 1651–1661, doi: 10.1175/BAMS-D-11-00170.1.

Cavaleri, L., and Coauthors, 2007: Wave modelling – the state of the art. *Progress in Oceanography*, **75 (4)**, 603–674, doi: https://doi.org/10.1016/j.pocean.2007.05.005.

Chawla, A., and J. T. Kirby, 2002: Monochromatic and random wave breaking at blocking points. *Journal of Geophysical Research: Oceans*, **107 (7)**, 1–19, doi: 10.1029/2001jc001042.

Clarke, A. J., and D. S. Battisti, 1981: The effect of continental shelves on tides. *Deep Sea Research Part A. Oceanographic Research Papers*, **28 (7)**, 665–682, doi: https://doi.org/10.1016/0198-0149(81)90128-X.

Collins, C. O., and Coauthors, 2016: Doppler Correction of Wave Frequency Spectra Measured by Underway Vessels. *Journal of Atmospheric and Oceanic Technology*, **34 (2)**, 429–436, doi: 10.1175/jtech-d-16-0138.1.

Colosi, L. V., A. B. Villas Bôas, and S. T. Gille, 2021: The seasonal cycle of significant wave height in the ocean: Local versus remote forcing. *Journal of Geophysical Research: Oceans*, **126 (8)**, e2021JC017 198, doi: https://doi.org/10.1029/2021JC017198, e2021JC017198 2021JC017198.

Cox, C., and W. Munk, 1956: Slopes of the sea surface deduced from photographs of sun glitter. *Bulletin of the scripps institution of oceanography of the University of California*, **6 (9)**, 401–488, 0608246v3.

Crosby, S. C., W. C. O'Reilly, and R. T. Guza, 2016: Modeling long-period swell in Southern California: Practical boundary conditions from buoy observations and global wave model predictions. *Journal of Atmospheric and Oceanic Technology*, **33 (8)**, 1673–1690, doi: 10.1175/JTECH-D-16-0038.1.

D'Asaro, E., and C. McNeil, 2007: Air-sea gas exchange at extreme wind speeds measured by autonomous oceanographic floats. *Journal of Marine Systems*, **66 (1-4)**, 92–109, doi: 10.1016/j.jmarsys.2006.06.007.

Datawell B.V., 2021: *Datawell Waverider Manual DWR4*. Haarlem, Netherlands, Datawell B.V., URL https://www.datawell.nl/Portals/0/Documents/Manuals/datawell_manual_dwr4_2021-12-01.pdf.

Davidson, M. A., T. J. O'Hare, and K. J. George, 2008: Tidal modulation of incident wave

heights: Fact or fiction? *Journal of Coastal Research*, **24 (2B)**, 151–159, URL http://www.jstor.org/stable/30138753.

Deike, L., 2022: Mass transfer at the ocean–atmosphere interface: the role of wave breaking, droplets, and bubbles. *Annual Review of Fluid Mechanics*, **54**, 191–224.

Department of Fisheries and Oceans Canada, 2023: Marine environmental data section archive. Accessed: 2023/09/08, https://meds-sdmm.dfo-mpo.gc.ca.

DiGiacomo, P. M., and B. Holt, 2001: Satellite observations of small coastal ocean eddies in the southern california bight. *Journal of Geophysical Research: Oceans*, **106 (C10)**, 22 521–22 543.

Dobson, E., F. Monaldo, J. Goldhirsh, and J. Wilkerson, 1987: Validation of geosat altimeter-derived wind speeds and significant wave heights using buoy data. *Journal of Geophysical Research: Oceans*, **92 (C10)**, 10 719–10 731, doi: https://doi.org/10.1029/JC092iC10p10719.

Donelan, M. A., F. W. Dobson, S. D. Smith, and R. J. Anderson, 1993: On the dependence of sea surface roughness on wave development. *Journal of physical Oceanography*, **23 (9)**, 2143–2149.

Edson, J., and Coauthors, 2007: The coupled boundary layers and air-sea transfer experiment in low winds. *Bulletin of the American Meteorological Society*, **88 (3)**, 341–356, doi: 10.1175/BAMS-88-3-341.

Egbert, G., and S. Erofeeva, 2002: Efficient inverse modeling of barotropic ocean tides. *J. Atmos. Ocean. Tech.*, **19**, 183–204, doi: 10.1175/1520-0426(2002)019⟨0183:EIMOBO⟩2.0.CO;2.

Erofeeva, S., L. Padman, and S. L. Howard, 2020: Tide ModelDriver (TMD) version 2.5, Toolbox for Matlab, GitHub. URL https://github.com/EarthAndSpaceResearch/TMD_Matlab_Toolbox_v2.5.

Fienup-Riordan, A., and E. Carmack, 2011: "The ocean is always changing": Nearshore and farshore perspectives on Arctic coastal seas. *Oceanography*, **24 (3)**, 266–279.

Gargettt, A. E., and B. A. Hughes, 1972: On the interaction of surface and internal waves. *Journal of Fluid Mechanics*, **52 (1)**, 179–191, doi: 10.1017/S0022112072003027.

Gemmrich, J., and C. Garrett, 2012: The signature of inertial and tidal currents in offshore wave records. *Journal of Physical Oceanography*, **42 (6)**, 1051–1056, doi: 10.1175/JPO-D-12-043.1.

Gille, S. T., S. G. Llewellyn Smith, and S. M. Lee, 2003: Measuring the sea breeze from quikscat scatterometry. *Geophysical Research Letters*, **30 (3)**, doi: https://doi.org/10.1029/

2002GL016230.

Grossmann-Matheson, G., I. R. Young, A. Meucci, and J.-H. Alves, 2024: Global tropical cyclone extreme wave height climatology. *Scientific Reports*, **14 (1)**, 4167.

Guillou, N., 2017: Modelling effects of tidal currents on waves at a tidal stream energy site. *Renewable Energy*, **114**, 180–190, doi: https://doi.org/10.1016/j.renene.2016.12.031.

Hall, C., and R. Jensen, 2022: Usace coastal and hydraulics laboratory quality controlled, consistent measurement archive. *Nature Scientific Data*, **9 (248)**, doi: https://doi.org/10.1038/s41597-022-01344-z.

Halsne, T., A. Benetazzo, F. Barbariol, K. H. Christensen, A. Carrasco, and Ø. Breivik, 2024: Wave modulation in a strong tidal current and its impact on extreme waves. *Journal of Physical Oceanography*, **54 (1)**, 131–151.

Hanson, J. L., B. A. Tracy, H. L. Tolman, and R. D. Scott, 2009: Pacific hindcast performance of three numerical wave models. *Journal of Atmospheric and Oceanic Technology*, **26 (8)**, 1614–1633, doi: 10.1175/2009JTECHO650.1.

Harlan, J., E. Terrill, L. Hazard, C. Keen, D. Barrick, C. Whelan, S. Howden, and J. Kohut, 2010: The integrated ocean observing system high-frequency radar network: Status and local, regional, and national applications. *Marine Technology Society Journal*, **44**, 122–132, doi: 10.4031/MTSJ.44.6.6.

Harley, M. D., and Coauthors, 2017: Extreme coastal erosion enhanced by anomalous extratropical storm wave direction. *Scientific reports*, **7 (1)**, 6033.

Ho, A., S. T. Merrifield, and N. Pizzo, 2022: Data from: Wave-tide interaction for a strongly modulated wave field. UC San Diego Library Digital Collections, doi: https://doi.org/10.6075/J0WD40R1.

Ho, A., S. T. Merrifield, and N. Pizzo, 2023: Wave-tide interaction for a strongly modulated wave field. **53 (3)**, 915–927, doi: https://doi.org/10.1175/JPO-D-22-0166.1.

Holthuijsen, L. H., and H. L. Tolman, 1991: Effects of the gulf stream on ocean waves. *Journal of Geophysical Research: Oceans*, **96 (C7)**, 12 755–12 771, doi: https://doi.org/10.1029/91JC00901.

Hsu, S. A., E. A. Meindl, and D. B. Gilhousen, 1994: Determining the power-law wind-profile exponent under near-neutral stability conditions at sea. *Journal of Applied Meteorology*, **33**, doi: 10.1175/1520-0450(1994)033⟨0757:DTPLWP⟩2.0.CO;2.

Hughes, B. A., 1978: The effect of internal waves on surface wind waves 2. theoretical analysis.

Journal of Geophysical Research: Oceans, **83 (C1)**, 455–465, doi: https://doi.org/10.1029/JC083iC01p00455.

Janssen, P. A., 2003: Nonlinear four-wave interactions and freak waves. *Journal of Physical Oceanography*, **33 (4)**, 863–884.

Jones, B., 2000: A numerical study of wave refraction in shallow tidal waters. *Estuarine, Coastal and Shelf Science*, **51 (3)**, 331–347.

Kachelein, L., S. T. Gille, M. R. Mazloff, and B. Cornuelle, 2023: Characterizing non-phase-locked tidal currents in the california current system using high-frequency radar. *Authorea Preprints*.

Kenyon, K. E., 1971: Wave refraction in ocean currents. *Deep Sea Research and Oceanographic Abstracts*, Elsevier, Vol. 18, 1023–1034.

Kim, S. Y., and P. M. Kosro, 2013: Observations of near-inertial surface currents off oregon: Decorrelation time and length scales. *Journal of Geophysical Research: Oceans*, **118 (7)**, 3723–3736.

Kim, S. Y., and Coauthors, 2011: Mapping the u.s. west coast surface circulation: A multiyear analysis of high-frequency radar observations. *Journal of Geophysical Research: Oceans*, **116 (C3)**, doi: https://doi.org/10.1029/2010JC006669.

Kuik, A. J., G. P. van Vledder, and L. H. Holthuijsen, 1988: A Method for the Routine Analysis of Pitch-and-Roll Buoy Wave Data. 1020-1034 pp., doi: 10.1175/1520-0485(1988)018⟨1020:AMFTRA⟩2.0.CO;2.

Large, W. G., J. C. McWilliams, and S. C. Doney, 1994: Oceanic vertical mixing: A review and a model with a nonlocal boundary layer parameterization. *Reviews of Geophysics*, **32 (4)**, 363–403, doi: 10.1029/94RG01872.

Lenain, L., and N. Pizzo, 2021: Modulation of surface gravity waves by internal waves. *Journal of Physical Oceanography*, **51 (9)**, 2735–2748, doi: 10.1175/JPO-D-20-0302.1.

Lewis, D., 1994: *We, the navigators: The ancient art of landfinding in the Pacific*. University of Hawaii Press.

Lewis, M. J., T. Palmer, R. Hashemi, P. Robins, A. Saulter, J. Brown, H. Lewis, and S. Neill, 2019: Wave-tide interaction modulates nearshore wave height. *Ocean Dynamics*, **69 (3)**, 367–384, doi: 10.1007/s10236-018-01245-z.

Lodise, J., S. Merrifield, C. Collins, P. Rogowski, J. Behrens, and E. Terrill, 2022: Global climatology of extratropical cyclones from a new tracking approach and associated wave

heights from satellite radar altimeter. *Journal of Geophysical Research: Oceans*, **127 (11)**, e2022JC018 925.

Longuet-Higgins, M. S., 1986: Eulerian and lagrangian aspects of surface waves. *Journal of Fluid Mechanics*, **173**, 683–707, doi: 10.1017/S0022112086001325.

Longuet-Higgins, M. S., and R. Stewart, 1961: The changes in amplitude of short gravity waves on steady non-uniform currents. *Journal of fluid mechanics*, **10 (4)**, 529–549.

Longuet-Higgins, M. S., and R. W. Stewart, 1960: Changes in the form of short gravity waves on long waves and tidal currents. *Journal of Fluid Mechanics*, **8 (4)**, 565–583, doi: 10.1017/S0022112060000803.

Longuet-Higgins, M. S., and R. W. Stewart, 1962: Radiation stress and mass transport in gravity waves, with application to 'surf beats'. *Journal of Fluid Mechanics*, **13 (4)**, 481–504, doi: 10.1017/S0022112062000877.

Marechal, G., and F. Ardhuin, 2021: Surface Currents and Significant Wave Height Gradients: Matching Numerical Models and High-Resolution Altimeter Wave Heights in the Agulhas Current Region. *Journal of Geophysical Research: Oceans*, **126 (2)**, 1–16, doi: 10.1029/2020JC016564.

Masson, D., 1996: A case study of wave–current interaction in a strong tidal current. *Journal of physical oceanography*, **26 (3)**, 359–372.

McArthur, C., and M. Parsons, 2009: Ocean current and wave measurements at the jacksonville and fernandina beach ocean dredged material disposal sites. Tech. rep., U.S. Environmental Protection Agency Region 4, Atlanta, Georgia.

McWilliams, J. C., 1996: Modeling the oceanic general circulation. *Annual Review of Fluid Mechanics*, **28 (1)**, 215–248.

Mei, C. C., 1992: *The Applied Dynamics of Ocean Surface Waves*. World Scientific, doi: 10.1142/0752.

Mei, C. C., M. Stiassnie, and D. K.-P. Yue, 2005: *Theory and Applications of Ocean Surface Waves*. World Scientific, doi: 10.1142/5566.

Melville, W. K., 1996: The Role of Surface-Wave Breaking in Air-Sea Interaction. *Annual Review of Fluid Mechanics*, **28 (1)**, 279–321, doi: 10.1146/annurev.fl.28.010196.001431, URL http://www.annualreviews.org/doi/10.1146/annurev.fl.28.010196.001431.

Merrifield, M. A., and Coauthors, 2021: An early warning system for wave-driven coastal flooding at Imperial Beach, CA. *Natural Hazards*, **108**, 2591 – 2612, doi: 10.1007/

s11069-021-04790-x.

Miles, J. W., 1957: On the generation of surface waves by shear flows. *Journal of Fluid Mechanics*, **3 (2)**, 185–204.

Miles, J. W., 1972: Kelvin waves on oceanic boundaries. *Journal of Fluid Mechanics*, **55 (1)**, 113–127, doi: 10.1017/S0022112072001685.

Monaldo, F., 1988: Expected differences between buoy and radar altimeter estimates of wind speed and significant wave height and their implications on buoy-altimeter comparisons. *Journal of Geophysical Research: Oceans*, **93 (C3)**, 2285–2302, doi: https://doi.org/10.1029/JC093iC03p02285.

Mudd, K., A. Ho, A. Amador, J. Lodise, J. Behrens, and S. Merrifield, 2024: Wind velocity estimates from wave observing platforms. *Coastal Engineering Journal*, 1–13.

Munk, W. H., and M. A. Traylor, 1947: Refraction of ocean waves: a process linking underwater topography to beach erosion. *The Journal of Geology*, **55 (1)**, 1–26.

NOAA, C., 2014: Continuously updated digital elevation model (cudem) - 1/9 arc-second resolution bathymetric-topographic tiles. NOAA National Centers for Environmental Information, doi: https://doi.org/10.25921/ds9v-ky35.

O'Reilly, W. C., T. H. Herbers, R. J. Seymour, and R. T. Guza, 1996a: A Comparison of Directional Buoy and Fixed Platform Measurements of Pacific Swell. *Journal of Atmospheric and Oceanic Technology*, **13**, 231–238, doi: 10.1175/1520-0426(1996)013⟨0231:ACODBA⟩2.0.CO;2.

O'Reilly, W. C., T. H. C. Herbers, R. J. Seymour, and R. T. Guza, 1996b: A comparison of directional buoy and fixed platform measurements of pacific swell. *Journal of Atmospheric and Oceanic Technology*, **13 (1)**, 231 – 238, doi: 10.1175/1520-0426(1996)013⟨0231:ACODBA⟩2.0.CO;2.

Paduan, J. D., and L. Washburn, 2013: High-frequency radar observations of ocean surface currents. *Annual review of marine science*, **5**, 115–136.

Peregrine, D., 1976: Interaction of water waves and currents. Advances in Applied Mechanics, Vol. 16, Elsevier, 9–117, doi: https://doi.org/10.1016/S0065-2156(08)70087-5.

Peureux, C., F. Ardhuin, and P. V. Guimarães, 2021: On the Unsteady Steepening of Short Gravity Waves Near the Crests of Longer Waves in the Absence of Generation or Dissipation. *Journal of Geophysical Research: Oceans*, **126 (1)**, 1–16, doi: 10.1029/2020JC016735.

Phillips, O. M., 1957: On the generation of waves by turbulent wind. *Journal of fluid mechanics*,

2 (5), 417–445.

Phillips, O. M., 1966: *The Dynamics of the Upper Ocean*. Cambridge University Press, London, UK.

Phillips, O. M., 1984: On the Response of Short Ocean Wave Components at a Fixed Wavenumber to Ocean Current Variations. *Journal of Physical Oceanography*, **14**, 1425–1433, doi: 10.1175/1520-0485(1984)014⟨1425:OTROSO⟩2.0.CO;2.

Phillips, O. M., 1988: Radar Returns from the Sea Surface - Bragg Scattering and Breaking Waves. *Journal of Physical Oceanography*, **18**.

Pizzo, N., L. Deike, and A. Ayet, 2021: How does the wind generate waves? *Physics Today*, **74 (11)**, 38–43.

Pizzo, N., and R. Salmon, 2021: Particle description of the interaction between wave packets and point vortices. *Journal of Fluid Mechanics*, **925**.

Pugh, D. T., 1987: *Tides, Surges and Mean Sea-Level*. John Wiley & Sons, Inc., Wiltshire, Great Britain, 1–486 pp.

Puthan, P., S. Sarkar, and G. Pawlak, 2021: Tidal synchronization of lee vortices in geophysical wakes. *Geophysical Research Letters*, **48 (4)**, e2020GL090 905, doi: https://doi.org/10.1029/2020GL090905, e2020GL090905 2020GL090905.

Quilfen, Y., and B. Chapron, 2019: Ocean surface wave-current signatures from satellite altimeter measurements. *Geophysical Research Letters*, **46 (1)**, 253–261, doi: https://doi.org/10.1029/2018GL081029.

Rascle, N., and F. Ardhuin, 2013: A global wave parameter database for geophysical applications. Part 2: Model validation with improved source term parameterization. *Ocean Modelling*, **70**, 174–188, doi: 10.1016/j.ocemod.2012.12.001.

Romero, L., 2019: Distribution of Surface Wave Breaking Fronts. *Geophysical Research Letters*, **46 (17-18)**, 10 463–10 474, doi: 10.1029/2019GL083408.

Romero, L., D. Hypolite, and J. C. McWilliams, 2020: Submesoscale current effects on surface waves. *Ocean Modelling*, **153**, doi: 10.1016/j.ocemod.2020.101662.

Romero, L., L. Lenain, and W. K. Melville, 2017: Observations of Surface Wave–Current Interaction. *Journal of Physical Oceanography*, **47 (3)**, 615–632, doi: 10.1175/JPO-D-16-0108.1.

Sadrpour, N., and D. Reineman, 2023: The impacts of climate change on surfing resources.

Salmon, R., 2002: Introduction to ocean waves. *San Diego, California, Scripps Institution of Oceanography University of California*, **66 (1–IV)**, 1–126.

Shampine, L. F., and M. W. Reichelt, 1997: The MATLAB ODE Suite. *SIAM Journal on Scientific Computing*, **18 (1)**, 1–22, doi: 10.1137/S1064827594276424.

Snodgrass, F., G. W. Groves, K. Hasselamn, G. Miller, W. Munk, and W. H. Powers, 1966: Propagation of Ocean Swell across the Pacific F. **259 (1103)**, 431–497.

Srinivasan, K., J. C. McWilliams, M. J. Molemaker, and R. Barkan, 2019: Submesoscale vortical wakes in the lee of topography. *Journal of Physical Oceanography*, **49 (7)**, 1949–1971.

Stockdon, H. F., R. A. Holman, P. A. Howd, and A. H. Sallenger Jr, 2006: Empirical parameterization of setup, swash, and runup. *Coastal engineering*, **53 (7)**, 573–588.

Sullivan, P. P., and J. C. McWilliams, 2010: Dynamics of Winds and Currents Coupled to Surface Waves. *Annual Review of Fluid Mechanics*, **42 (1)**, 19–42, doi: 10.1146/annurev-fluid-121108-145541.

Sverdrup, H., and W. Munk, 1947: Wind, Sea, and Swell. Theory of Relations For Forecasting. *Office*, **(601)**, 44.

Taylor, P. K., and M. J. Yelland, 2001: The dependence of sea surface roughness on the height and steepness of the waves. *Journal of Physical Oceanography*, **31 (2)**, 572–590, doi: 10.1175/1520-0485(2001)031⟨0572:TDOSSR⟩2.0.CO;2.

Terrill, E., and Coauthors, 2006: Data management and real-time distribution in the hf-radar national network. *OCEANS 2006*, 1–6, doi: 10.1109/OCEANS.2006.306883.

Timmermans, B., C. Gommenginger, G. Dodet, and J.-R. Bidlot, 2020: Global wave height trends and variability from new multimission satellite altimeter products, reanalyses, and wave buoys. *Geophysical Research Letters*, **47 (9)**, e2019GL086 880.

Tolman, H., 1990: The Influence of Unsteady Depths and Currents of Tides on Wind-Wave Propagation in Shelf Seas. *Journal of Physical Oceanography*, **20**, 1166–1174, doi: 10.1175/1520-0485(1990)020⟨1166:TIOUDA⟩2.0.CO;2.

Tolman, H. L., 1988: Propagation of wind waves on tides. *Coastal Engineering 1988*, **(36)**, 512–523, doi: 10.1061/9780872626874.037.

Tolman, H. L., 1991: A third-generation model for wind waves on slowly varying, unsteady, and inhomogeneous depths and currents. *Journal of Physical Oceanography*, **21 (6)**, 782 – 797, doi: 10.1175/1520-0485(1991)021⟨0782:ATGMFW⟩2.0.CO;2.

Tolman, H. L., and N. Booij, 1998: Modeling wind waves using wavenumber-direction spectra and a variable wavenumber grid. *Global Atmosphere and Ocean System*, **6 (4)**, 295–309.

Unna, P. J., 1942: Waves and tidal streams [3]. *Nature*, **149 (3773)**, 219–220, doi: 10.1038/149219a0.

Villas Bôas, A. B., and N. Pizzo, 2021: The geometry, kinematics, and dynamics of the two-way coupling between wind, waves, and currents. *US CLIVAR Variations*, **19 (1)**, 18–26.

Villas Bôas, A. B., S. T. Gille, M. R. Mazloff, and B. D. Cornuelle, 2017: Characterization of the deep water surface wave variability in the california current region. *Journal of Geophysical Research: Oceans*, **122 (11)**, 8753–8769, doi: https://doi.org/10.1002/2017JC013280.

Vincent, C. E., 1979: The interaction of wind-generated sea waves with tidal currents. *Journal of Physical Oceanography*, **9 (4)**, 748 – 755, doi: 10.1175/1520-0485(1979)009⟨0748:TIOWGS⟩2.0.CO;2.

Vrećica, T., N. Pizzo, and L. Lenain, 2022: Observations of Strongly Modulated Surface Wave and Wave Breaking Statistics at a Submesoscale Front. *Journal of Physical Oceanography*, **52 (2)**, 289–304, doi: 10.1175/JPO-D-21-0125.1.

Wallace, W. C., D., 1992: Large air–sea gas fluxes associated with breaking waves. *Nature*, **356**, 694–696, doi: https://doi.org/10.1038/356694a0.

Wang, J., H. Torres, P. Klein, A. Wineteer, H. Zhang, D. Menemenlis, C. Ubelmann, and E. Rodriguez, 2023: Increasing the observability of near inertial oscillations by a future odysea satellite mission. *Remote Sensing*, **15 (18)**, doi: 10.3390/rs15184526.

Wang, P., and J. Sheng, 2018: Tidal modulation of surface gravity waves in the gulf of maine. *Journal of Physical Oceanography*, **48 (10)**, 2305–2323, doi: 10.1175/JPO-D-17-0250.1.

Weinberg, H., and R. Burridge, 1974: Horizontal ray theory for ocean acoustics. *The Journal of the Acoustical Society of America*, **55 (1)**, 63–79.

Wolf, J., and D. Prandle, 1999: Some observations of wave-current interaction. *Coastal Engineering*, **37 (3-4)**, 471–485, doi: 10.1016/S0378-3839(99)00039-3.

Young, I., 1999: Seasonal variability of the global ocean wind and wave climate. *International Journal of Climatology: A Journal of the Royal Meteorological Society*, **19 (9)**, 931–950.